Computational Analysis of Transient Unstart/Restart Characteristics in a Variable Geometry, High-Speed Inlet

Jonathan Paul Reardon

Dissertation submitted to the faculty of the Virginia Polytechnic Institute and State University in partial fulfillment of the requirements for the degree of

Doctor of Philosophy
In
Aerospace Engineering

Joseph A. Schetz
K. Todd Lowe
Christopher J. Roy
Anthon R. Pilon

October 31, 2019
Blacksburg, VA

Keywords: Inlet, Computational Fluid Dynamics, Aerodynamics, Propulsion

Computational Analysis of Transient Unstart/Restart Characteristics in a Variable Geometry, High-Speed Inlet

Jonathan Paul Reardon

ABSTRACT

This work seeks to analyze the transient characteristics of a high-speed inlet with a variable-geometry, rotating cowl. The inlet analyzed is a mixed compression inlet with a compression ramp, sidewalls and a rotating cowl. The analysis is conducted at nominally Mach 4.0 wind tunnel conditions. Advanced Computational Fluid Dynamics techniques such as transient solutions to the Unsteady Reynolds-averaged Navier-Stokes equations and relative mesh motion are used to predict and investigate the unstart and restart processes of the inlet as well as the associated hysteresis. Good agreement in the quasi-steady limit with a traditional analysis approach was obtained. However, the new model allows for more detailed, time-accurate information regarding the fully transient features of the unstart, restart, and hysteresis to be obtained that could not be captured by the traditional, quasi-steady analysis. It is found that the development of separated flow regions at the shock impingement points as well as in the corner regions play a principal role in the unstart process of the inlet. Also, the hysteresis that exists when the inlet progresses from the unstarted to restarted condition is captured by the time-accurate computations. In this case, the hysteresis manifests itself as a requirement of a much smaller cowl angle to restart the inlet than was required to unstart it. This process is shown to be driven primarily by the viscous, separated flow that sets up ahead of the inlet when it is unstarted. In addition, the effect of cowl rotation rate is assessed and is generally found to be small; however, definite trends are observed. Finally, a rigorous assessment of the computational errors and uncertainties of the Variable-Cowl Model indicated that Computation Fluid Dynamics is a valid tool for analyzing the transient response of a high-speed inlet in the presence of unstart, restart and hysteresis phenomena. The current work thus extends the state of knowledge of inlet unstart and restart to include transient computations of contraction ratio unstart/restart in a variable-geometry inlet.

Computational Analysis of Transient Unstart/Restart Characteristics in a Variable Geometry, High-Speed Inlet

Jonathan Paul Reardon

GENERAL AUDIENCE ABSTRACT

Flight at high speeds requires efficient engine operation and performance. As the vehicle traverses through its flight profile, the engine will undergo changes in operating conditions. At high speeds, these changes can lead to significant performance loss and can be detrimental to the vehicle. It is, therefore, important to develop tools for predicting characteristics of the engine and its response to disturbances. Computational Fluid Dynamics is a common method of computing the fluid flow through the engine. However, traditionally, CFD has been applied to predict the static performance of an engine. This work seeks to advance the state of the art by applying CFD to predict the transient response of the engine to changes in operating conditions brought about by a variable geometry inlet with rotating components.

ACKNOWLEDGEMENTS

I would like to thank my committee chair and co-chair, Dr. Schetz and Dr. Lowe, for giving me the opportunity to conduct this work. Without their support and guidance this work could not have been accomplished. I also greatly appreciate the flexibility they allowed me throughout this process.

I would also like to thank my committee members, Dr. Roy and Dr. Pilon, for their willingness to serve on the committee and for their expert advice and comments.

In addition, I'd especially like to recognize Rob Vermeland, who made this work possible and Frank Marconi for all of his advice and comments during the course of this work.

Finally, I would like to thank my family and friends for their encouragement. I could not have done this without their constant support.

Thank you,

Jonathan Reardon

TABLE OF CONTENTS

1 Introduction 1
1.1 Background 1
1.2 Summary of Current Work 1
1.3 Dissertation Outline 4
2 Overview of High-Speed Engines and Physical Concepts 5
2.1.1 The Ramjet 6
2.1.2 The Scramjet 7
2.1.3 Combined-Cycle Engines 7
2.1.4 Inlets for High-Speed Engines 8
2.2 Physical Phenomena Associated with High-Speed Inlet Design and Analysis 10
2.2.1 Shock-Boundary Layer Interaction 10
2.2.2 Three-Dimensional Effects 12
2.2.3 Inlet Starting and Unstarting 13
3 Review of Relevant Previous Works 15
3.1 Development of Inlets with Variable Geometry 15
3.2 Inlet Unstart Analysis: Experimental Studies 16
3.3 Inlet Unstart Analysis: Computational Studies 18
3.4 Current Research Focus 20
4 Analysis Approach 23
4.1 Governing Equations 23
4.2 Turbulence Models 25
4.2.1 One-Equation Models 26
4.2.2 Two-Equation Models 27
4.2.3 Higher-Order Models 29
5 Computational Model 31
5.1 Spatial Discretization 31
5.1.1 Fixed-Cowl Models 31
5.1.2 Variable-Cowl Model 34
5.2 Boundary Conditions 37
5.3 Temporal Discretization 38
5.4 Flow Conditions 38
6 Computational Verification and Validation 39
6.1 Spatial Discretization Error Assessment 39
6.2 Temporal Error Assessment 43
6.3 Iterative Error Assessment 51
7 Computational Results 53
7.1 Fixed-Cowl Model Results 53
7.1.1 Three-Dimensional Results 54
7.1.2 Two-Dimensional Results 70
7.1.3 Turbulence Model Assessments 73
7.2 Unsteady Variable-Cowl Model Results 80
7.2.1 Comparison of the Variable-Cowl Model with the Fixed-Cowl Model 81
7.2.2 Cowl Rotation Cases 86
7.2.3 The Impact of Corner Flows and Separation on the Unstart Process 97
7.2.4 The Effect of Cowl Rotation Rate 109
7.2.5 Unsteady Two-Dimensional Results 112
7.2.6 Turbulence Model Assessments 117
7.3 Summary and Discussion 120
8 Conclusion 122
8.1 Future Works 125
9 References 126

TABLE OF FIGURES

Figure 1: Schematic of a Scramjet Engine [4] 3
Figure 2: Comparison of Specific Impulse for Various Propulsion Systems [7] 6
Figure 3: Schematic of a Ramjet Engine [9] 7
Figure 4: An Example of an External Compression Inlet [12] 9
Figure 5: An Example of an Internal Compression Inlet [13] 9
Figure 6: An Example of a Mixed Internal and External Compression Inlet [14] 10
Figure 7: Schematic of the Rectangular Inlet of Ref. [3] Used in the Current Computational Study 21
Figure 8: Shock System Developed for the Inlet with the Long Cowl from Ref. [3] 21
Figure 9: Computational Domain for the Fixed-Cowl Model 32
Figure 10: Structured Mesh for the Fixed-Cowl Model, 8 deg Cowl Angle Shown 33
Figure 11: Fixed-Cowl Model Grids at a) $\theta c = 8$ deg, b) 1.2 deg, and c) 0 deg ($\beta = 3$ deg, 9.8 deg, 11 deg) 33
Figure 12: Fixed-Cowl Model Grids at a) $\theta c = 8$ deg, b) 1.2 deg, and c) 0 deg ($\beta = 3$ deg, 9.8 deg, 11 deg) Enlarged to Show Inlet Ramp and Cowl Details 34
Figure 13: Computational Domain for the Variable-Cowl Model 36
Figure 14: Distinct a) Body-Side and b) Cowl Grids used for the Variable Geometry Model 36
Figure 15: Overset, Structured Mesh for the Variable-Cowl Model, 8 deg Cowl Angle Shown 37
Figure 16: Cowl Grid Overset on Body Grid Before and After Sequential Cutting and Blanking is Applied 37
Figure 17: Centerline Normalized Pressures from the Coarse, Medium, and Fine Grids Compared with the Exact Value from Richardson Extrapolation 42
Figure 18: Relative Discretization Error for the Centerline Normalized Pressures for the Coarse, Medium, and Fine Grids 43
Figure 19: Time Histories of Mass Flow Rate Through the Inlet for Different Cowl Rotation Rates Obtained Using Different Time Steps 46
Figure 20: Centerline Mach Number Contours of the Oscillatory Unstarted Flow Field Computed with a) the Baseline and b) Fine Timesteps 47
Figure 21: Mass Flow Rate Through the Inlet During the Rotation of the Cowl Plotted as a Function of Cowl Angle for Different Cowl Rotation Rates Obtained Using Different Time Steps 49
Figure 22: Time Histories of Mass Flow Rate Through the Inlet for Different Cowl Rotation Rates Obtained Using the Different Time Steps and the Menter SST Turbulence Model 50
Figure 23: Mass Flow Rate Through the Inlet During the Rotation of the Cowl Plotted as a Function of Cowl Angle for Different Cowl Rotation Rates Obtained Using Different Time Steps and the Menter SST Turbulence Model 51
Figure 24: Comparison of the Time Histories of Mass Flow Rate for Computations with 10, 20, and 30 Sub-Iterations to Assess the Impact of Iterative Errors 52
Figure 25: Centerline Mach Number Contours for the Fixed-Cowl Model at $\theta c = 8$ deg 54
Figure 26: Mach Number Contours for the Fixed-Cowl Model at $\theta c = 8$ deg along a Plane 0.1 inches above the Inlet Ramp 55
Figure 27: Simulated Oil Flow Lines and Log of the Pressure Ratio Contours along the Inlet Ramp and Sidewall for Cowl at $\theta c = 8$ deg 56
Figure 28: Simulated Oil Flow Lines and Log of the Pressure Ratio Contours along the Inlet Ramp and Sidewall for Cowl at $\theta c = 8$ deg with Isosurface of U=0 showing Separated Flow Regions 57
Figure 29: a) Pressure Contours and b) Spanwise Pressures in the Region of the Cowl Shock Impingement 58
Figure 30: Spanwise and Centerline Mach Number Contours through the Inlet at $\theta c = 8$ deg 58
Figure 31: Comparison of the Normalized Centerline Wall Pressures from the Fixed-Cowl Model at $\theta c = 8$ deg and the Experimental Results of Ref. [3] 60
Figure 32: Centerline Mach Number Contours for the Fixed-Cowl Model at $\theta c = 1.2$ deg 62
Figure 33: Mach Number Contours for the Fixed-Cowl Model at $\theta c = 1.2$ deg along Plane 0.1 inches above the Inlet Ramp 62
Figure 34: Simulated Oil Flow Lines and Log of the Pressure Ratio Contours along the Inlet Ramp and Sidewall for Cowl at $\theta c = 1.2$ deg 63

Figure 35: Simulated Oil Flow Lines and Log of the Pressure Ratio Contours along the Inlet Ramp and Sidewall for Cowl at $\theta c = 1.2$ deg with Isosurface of U=0 showing Separated Flow Regions 63
Figure 36: Spanwise and Centerline Mach Number Contours through the Inlet at $\theta c = 1.2$ deg 64
Figure 37: Streamlines Illustrating Corner Vortices that Develop in the Inlet at $\theta c = 1.2$ deg 64
Figure 38: Comparison of the Normalized Centerline Wall Pressures from the Fixed-Cowl Model at $\theta c = 1.2$ deg and the Experimental Results of Ref. [3] 65
Figure 39: Centerline Mach Number Contours for the Fixed-Cowl Model at $\theta c = 0$ deg 66
Figure 40: Time History of Centerline Mach Number Contours for the Fixed-Cowl Model at $\theta c = 0$ deg for a Time-Accurate Simulation 66
Figure 41: Comparison of the Normalize Centerline Wall Pressures from the Fixed-Cowl Model at $\theta c = 0$ deg and the Experimental Results of Ref. [3] 67
Figure 42: Comparison of Mass Flow Rates from the Fixed-Cowl Models with the Theoretical Values from Ref. [3] as a Function of the Cowl Convergence Angle 69
Figure 43: Time-History of the Mass Flow Rate through the Inlet when Unstarted at the Cowl Angle of $\theta c = 0$ deg 69
Figure 44: Comparison of the Normalized Centerline Wall Pressures from the 2D Fixed-Cowl Model at $\theta c = 8$ deg with the Fully 3D Fixed-Cowl Model and with the Experimental Results of Ref. [3] 71
Figure 45: Comparison of the Normalized Centerline Wall Pressures from the 2D Fixed-Cowl Model at $\theta c = 1.2$ deg with the Fully 3D Fixed-Cowl Model and with the Experimental Results of Ref. [3] 72
Figure 46: Comparison of the Normalized Centerline Wall Pressures from the 2D Fixed-Cowl Model at $\theta c = 0$ deg with the Fully 3D Fixed-Cowl Model and with the Experimental Results of Ref. [3] 72
Figure 47: Comparison of Mass Flow Rates from the 2D and 3D Fixed-Cowl Models with the Theoretical Values from Ref. [3] as a Function of the Cowl Convergence Angle 73
Figure 48: Inlet Body-Side Only Grid Used to Calculate Boundary Layer Profiles on the Ramp 74
Figure 49: Inlet Body-Side Only Grid Used to Calculate Boundary Layer Profiles on the Ramp Enlarged to Show Inlet Ramp Details 74
Figure 50: a) Mach Number and b) Velocity Boundary Layer Profiles at x=6.81 inches Computed with a Range of Turbulence Models and Compared with Experimental Data from Ref. [3] 75
Figure 51: Law of the Wall Plot of Computed Boundary Layer Profiles Using Different Turbulence Models 76
Figure 52: Comparison of Normalized Centerline Wall Pressures between Various Turbulence Models and Experimental Data from Ref. [3] at Cowl Angle $\theta c = 8$ deg 79
Figure 53: Comparison of Normalized Centerline Wall Pressures between Various Turbulence Models and Experimental Data from Ref. [3] at Cowl Angle $\theta c = 8$ deg 80
Figure 54: Comparison of Shock Structure in Simulated Schlieren Images from the Variable-Cowl Model and the Fixed-Cowl Model at the Static Cowl Angle of $\theta c = 8$ deg 83
Figure 55: Comparison Normalized Centerline Wall Pressures from the Variable-Cowl Model and the Fixed-Cowl Model at the Static Cowl Angle of $\theta c = 8$ deg 83
Figure 56: Comparison of Shock Structure in Simulated Schlieren Images from the Variable-Cowl Model and the Fixed-Cowl Model at the Static Cowl Angle of $\theta c = 1.2$ deg 84
Figure 57: Comparison Normalized Centerline Wall Pressures from the Variable-Cowl Model and the Fixed-Cowl Model at the Static Cowl Angle of $\theta c = 1.2$ deg 84
Figure 58: Comparison of Shock Structure in Simulated Schlieren Images from the Variable-Cowl Model and the Fixed-Cowl Model at the Static Cowl Angle of $\theta c = 0$ deg 85
Figure 59: Comparison Normalized Centerline Wall Pressures from the Variable-Cowl Model and the Fixed-Cowl Model at the Static Cowl Angle of $\theta c = 0$ deg 85
Figure 60: Comparison of Mass Flow Rates from Fixed-Cowl Model and Variable-Cowl Model with the Theoretical Values from Ref. [3] as a Function of the Cowl Convergence Angle 86
Figure 61: Cowl Angle, θc, and Rotation Rate, ωc, as a Function of Time for the Baseline Transient Computation for the 10 rad/s Cases 87
Figure 62: Centerline Mach Number Contours During Inlet Opening, Holding at the Horizontal Position, and Closing Obtained from a Three-Dimensional, Transient Computation Using the Variable-Cowl Model 89
Figure 63: Time History of Mass Flow Rate Through the Inlet During the Rotation of the Cowl for the Baseline Computation 90

Figure 64: Pressure Time Histories during the Cowl Rotation in the Baseline Computation 91
Figure 65: Pressure Tap Locations Shown in Figure 64 Corresponding to Experimental Tap Locations from Ref. [3] 91
Figure 66: Centerline Mach Number Contours During Inlet Unstart 93
Figure 67: Normalized Wall Pressure Time Histories During Inlet Unstart.....94
Figure 68: Centerline Mach Number Contours During Inlet Restart.....95
Figure 69: Mass Flow Rate Through the Inlet During the Rotation of the Cowl Plotted as a Function of Cowl Angle for the Baseline Computation.....97
Figure 70: x-t Wall Pressure Diagram Along the Centerline of the Inlet 98
Figure 71: x-t Wall Pressure Diagram Along a Line at Z = 0.9 inches (0.1 inch off the Side Wall).....99
Figure 72: Time Histories of Mach Number Contours along a Plane 0.1 inches Above Body Side Ramps 101
Figure 73: Time Histories of Mach Number Contours along Axial and Centerline Cuts.....102
Figure 74: Time Histories of Vorticity Contours along Axial and Centerline Cuts 103
Figure 75: Oil Flow Lines on the Inlet Ramp and Sidewalls During the Cowl Rotation Highlighting the Development of the Separation Bubbles 105
Figure 76: Simulated Oil Flow Lines on the Inlet Ramp and Sidewalls During the Unstart Process Highlighting the Motion of the Separation Bubbles.....107
Figure 77: Time Histories of Mass Flow Rate Through the Inlet for Different Cowl Rotation Rates.....110
Figure 78: Mass Flow Rate Through the Inlet During the Rotation of the Cowl Plotted as a Function of Cowl Angle for Different Cowl Rotation Rates 111
Figure 79: Centerline Mach Number Contours at θc = 6.9 deg Computed with a) the Baseline Rotation Rate of 10 rad/s and b) the Slow Rotation Rate of 1 rad/s.....112
Figure 80: Time Histories of Mass Flow Rate Through the Inlet for Different Cowl Rotation Rates Obtained Using the Two-Dimensional Model.....113
Figure 81: Centerline Mach Number Contours During Cowl Opening for the a) 3D and b) 2D Models....114
Figure 82: Centerline Mach Number Contours for the a) 3D and b) 2D Models at 14 msec 116
Figure 83: Mass Flow Rate Through the Inlet During the Rotation of the Cowl Plotted as a Function of Cowl Angle for Different Cowl Rotation Rates Obtained Using the Two-Dimensional Model 117
Figure 84: Comparison of Time Histories of Mass Flow Rate Through the Inlet Using the Cubic k-ε and Menter SST Turbulence Models.....118
Figure 85: Centerline Mach Number Contours at 13.45 msec for the a) Cubic k-ε and b) SST Models.....119
Figure 86: Centerline Mach Number Contours at 14.05 msec for the a) Cubic k-ε and b) SST Models.....119

TABLE OF TABLES

Table 1: Nominal Test Conditions used for Computations from Ref. [3] 38
Table 2: Grid Characteristics used to Assess Spatial Discretization Error 39
Table 3: Mass Flow Rate Through the Inlet for Each Grid 40
Table 4: Summary of the Grid Convergence Indices for the Spatial Discretization Error Estimate.....41
Table 5: Time-Averaged Mass Flow Rate Through the Inlet for Each Time Step 44
Table 6: Summary of the Grid Convergence Indices for the Temporal Error Estimate 44
Table 7: Cowl Angle at Peak Mass Flow Rate and Peak Mass Flow Rate Obtained Using Different Time Steps 49
Table 8: Cowl Angle at Peak Mass Flow Rate and Peak Mass Flow Rate Obtained Using Different Sub-Iterations.....52
Table 9: Mass Flow Rates from the Fixed-Cowl Model and the Theoretical Values from Ref. [3].....70
Table 10: Mass Flow Rates Computed using the 2D Fixed-Cowl Model 73
Table 11: Boundary Layer Parameters for Flow Over the Inlet Ramp (No Cowl Present and no Foreplate)78
Table 12: Summary of the Variable-Cowl Model Cases.....81
Table 13: Mass Flow Rates Through the Inlet for the Fixed-Cowl Model and the Variable-Cowl Model ...86
Table 14: Peak Mass Flow Rates Prior to Inlet Unstart for Different Cowl Rotation Rates 110
Table 15: Cowl Angle Corresponding to Peak Mass Flow Rate Prior to Inlet Unstart for Different Cowl Rotation Rates 111
Table 16: Cowl Angle at Peak Mass Flow Rate and Peak Mass Flow Rate Obtained Using Different Turbulence Models.....118

NOMENCLATURE

A	Area
a	Speed of Sound
c_f	Skin Friction Coefficient
c_p	Specific Heat at Constant Pressure
c_v	Specific Heat at Constant Volume
CAP	Mass Capture Ratio
e	Internal Energy
k	Turbulent Kinetic Energy
k	Thermal Conductivity
E_t	Total Energy
F_{thrust}	Thrust Force
g_o	Gravitational Constant
GCI	Grid Convergence Index
H_{cap}	Capture Height
$H_{cap,act}$	Capture Height Adjusted for Viscous Boundary Layer
H_{cowl}	Cowl Height
H_{th}	Throat Height
H_m	Model Height
I_{sp}	Specific Impulse
L	Isolator Length
L_c	Cowl Length
L_r	Ramp Length
M	Mach Number
$\dot{m}$	Mass Flow Rate
$\dot{m}_f$	Fuel Mass Flow Rate
p	Observed Order of Accuracy
P	Static Pressure
P_t	Total Pressure
q_i	Heat Flux Vector
R	Gas Constant
r_{ij}	Refinement Factor from Grid i to Grid j
RDE	Relative Discretization Error
Re	Reynolds Number
S_{ij}	Mean Strain Rate
T	Static Temperature
t	Time
T_t	Total Temperature
u	Axial Velocity Component
u_*	Friction Velocity
u^+	Non-Dimensional Law-of-the-Wall Velocity
u_{eff}	Van-Driest Effective Velocity
v	Vertical Velocity Component
V	Velocity Magnitude
w	Spanwise Velocity Component
x	Axial Direction
y	Vertical Direction
z	Spanwise Direction
y^+	Non-Dimensional Wall Height

Greek

α	Ramp Angle
β	Cowl Convergence Angle
γ	Ratio of Specific Heats
δ	Boundary Layer Thickness
δ^*	Displacement Thickness
ϵ	Turbulent Dissipation Rate
ε_{ij}	Relative Error Between Grid i to Grid j
θ	Momentum Thickness
θ_c	Cowl Angle Below Horizontal
θ_r	Ramp Shock Wave Angle
θ_s	Shock Wave Angle
θ_w	Inviscid Shock Wave Angle
λ	Bulk Viscosity Coefficient
μ	Dynamic Viscosity Coefficient
μ_T	Turbulent Eddy Viscosity
ν_T	Kinematic Eddy Viscosity
ρ	Density
τ_{ij}	Viscous Stress Tensor
ω	Specific Dissipation Rate
ω_c	Cowl Rotation Rate
$\mathbf{\Omega}$	Vorticity Vector

Subscripts

c	Cowl
e	Value at Edge of Boundary Layer
inf	Freestream Value
w	Value at Wall
1	Freestream Station

1 Introduction

1.1 Background

At high Mach numbers, conventional turbine engines begin to lose performance because of high losses due to strong shocks that are developed inside the engine as the airstream is slowed for combustion. Therefore, to reach hypersonic velocities the development of ramjet and scramjet engines began and has been pursued for many years. See Refs. [1] and [2] for extensive reviews. However, a single, fixed ramjet/scramjet geometry is still not suitable for the large range of Mach numbers that are traversed by proposed hypersonic vehicles [1]. One solution to this problem is the introduction of variable geometry into these engines that allows for tailoring of the engine flow path to the local flight conditions, thus improving efficiency. Associated with these concepts are a vast array of technical challenges. These include practical concerns such as mechanical complexity and system weight [1], as well as aerodynamic concerns related to transient physics, including inlet unstart, restart, and hysteresis. Although these phenomena occur even in engines with fixed geometry, the introduction of the variable geometry makes them more prevalent.

1.2 Summary of Current Work

The current work focuses on the computational modeling of a high-speed inlet geometry that includes a variable geometry, rotating cowl. See Figure 1 for a schematic of a scramjet engine showing an inlet with a cowl. A significant amount of work has been conducted on the computational analysis of high-speed inlets as noted in later sections. However, transient computational analysis of inlets has not received as much focus, and the transient analysis of rotating geometries using CFD has received even less attention. This is primarily due to the large computational costs associated with time-accurate solutions to the unsteady Navier-Stokes equations. Therefore, traditionally, to analyze variable geometry inlets computationally, a series of steady state solutions is obtained at various geometric configurations that the inlet may take. This approach is based on the fact that the local flow time scale is often much smaller than the time scale of the motion of the variable geometry component, so that a quasi-steady assumption is valid. However, this approach does not provide a means for capturing the actual transients due to unstart, restart, or hysteresis

and cannot yield detailed time histories of physical quantities of interest as the inlet is changed from one state to the next.

Therefore, this work seeks to apply high-fidelity Computational Fluid Dynamics (CFD) methods specifically to the analysis of the transient phenomena associated with variable geometry inlets. To do this, an experimental rectangular inlet design from Reference [3] that includes a rotating cowl was chosen as a model problem and analyzed computationally. The inlet was analyzed at nominally Mach 4.0 conditions. The current work is divided into two parts: the development and analysis of the inlet using 1) a "Fixed-Cowl Model" and 2) a "Variable-Cowl Model". The Fixed-Cowl Model uses a series of steady-state computations at discrete, fixed, cowl angles, as would normally be done in a traditional quasi-steady analysis approach. These computations provide static performance of the inlet at different cowl angles. The results are compared to experimental data for validation of the computational grids, used to assess the sensitivity due to turbulence models, and used as a baseline for comparing the transient computations against. It is found that the turbulence model can have a dramatic effect on the performance calculation. It is noted that even small changes in computed boundary layer thicknesses can lead to very different results, especially near the inlet unstart boundary. It is also found that to accurately model the unstart physics requires a fully three-dimensional solution due to the presence of sidewall effects not present in purely two-dimensional solutions.

After using the Fixed-Cowl Model, the Variable-Cowl Model, which is the primary focus of this work is developed with the intent to advance of the state of the art of inlet analysis. This variable-geometry model incorporates advanced computational methods, including a time-accurate solution approach to the unsteady, Reynolds-averaged, Navier – Stokes (URANS) equations coupled with relative motion through use of an overset mesh approach. These methods are applied to analyze the transient features of the inlet with respect to cowl rotational motion including inlet unstart and restart and the associated hysteresis. Prior to conducting the full, time-accurate, relative motion solutions, the model is validated through comparisons of steady-state, static solutions at discrete cowl angles with the Fixed-Cowl Model and with the experimental data. After validation, the Variable-Cowl Model is used to analyze the transient performance of the inlet.

The results allow for time-accurate interrogations of the flow field as it adjusts to the change in position of the rotating cowl. The cowl angles at which the inlet unstarts and then restarts are in good agreement with the experimental results. It is shown that this analysis approach is capable of predicting the transient nature of inlet unstart and the hysteresis experienced as the inlet restarts. The transient aerodynamics due to unstart are captured including time-dependent pressure profiles in the inlet and on the cowl, as well as the transient mass flow rate through the inlet. It is also shown that hysteresis exists as the cowl is rotated and as the inlet is unstarted and then restarted with overshoots and undershoots in the mass flow rates prior to reaching steady state values. The source of the hysteresis in the inlet is theorized to be from large-scale vortical structures that are developed as the inlet is unstarted and from separated flow regions in the corners of the ducts. These structures are inherently unsteady and three-dimensional, again highlighting the three-dimensionality of even simple, rectangular inlets. The influence of corner flows on the unstart process is particularly emphasized and the development of these features with time as the cowl is rotated is shown. Also, a range of cowl rotation rates is assessed for comparison, and they generally show the same general trends. Finally, the uncertainties associated with such an analysis are rigorously quantified using well-documented verification and validation techniques developed for spatial discretization, iterative, and temporal error estimation in computational studies.

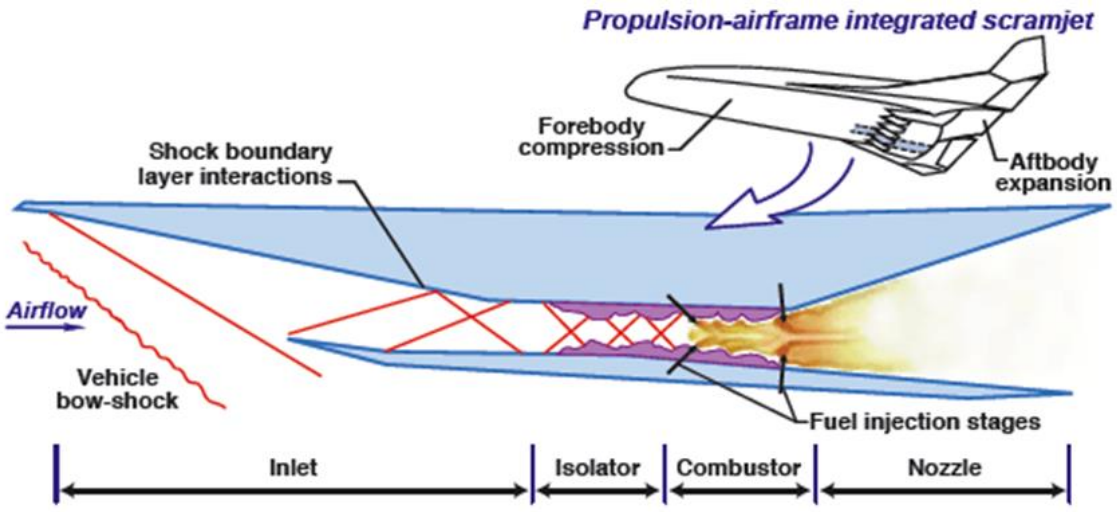

Figure 1: Schematic of a Scramjet Engine [4]

1.3 Dissertation Outline

The major research goals of the current work are:

1. To develop a variable-geometry model to analyze the transient features of an inlet with a rotating cowl computationally and to compare its results to a traditional quasi-steady analysis approach
2. To use the variable-geometry model to obtain insight into the physics of the transients that the inlet experiences including unstart/restart and hysteresis induced by cowl motion
3. To validate and verify the new model and to quantify uncertainties in the approach

By achieving these goals, the knowledge base of inlet unstart which, to date, has primarily been built on backpressure induced unstart, will be expanded to include an understanding of the physics related to contraction ratio induced unstart in variable-geometry inlets.

To accomplish this, the current work is organized as follows. Section 2 provides an overview of concepts related to high-speed engine design, analysis, and performance including physical flow features that will be discussed throughout the present work. Section 3 reviews previous works that are relevant to the subject of the current area of study including a survey of experimental and computational studies on inlet unstart and transient physics. Section 4 describes the analysis approach taken in the current work, including the governing equations and turbulence closure. Section 5 shows the computational model developed to analyze the inlet of Reference [3] including the spatial discretization of the grid, associated boundary conditions, and temporal discretization for the transient cases. Section 6 provides verification and validation of the computational results. Next, after validating the approach, Section 7 presents the major findings of this work with discussions. In this section, the steady state calculations will be presented and discussed first, followed by the transient results. Finally, conclusions and future works are then discussed in Section 8.

2 Overview of High-Speed Engines and Physical Concepts

Efficiency is a major design driver in engine development. Indeed, "support for an engine development is usually furnished only if there is reasonable promise that it will allow either an existing mission to be carried out more effectively (e.g., the evolution of very high bypass turbofan engines for low fuel consumption of transport aircraft) or an entirely new mission to be accomplished (e.g., the development of afterburning turbojet engines for supersonic flight) " [5]. In the case of hypersonic flight, this led to the development of ramjet and scramjet engines, and variations thereon. This is because the use of turbojets led to drastic losses due to shock waves and increased drag that significantly reduced engine performance and thus vehicle range. A simple performance parameter used to evaluate and compare different engine concepts is the specific impulse of the engine or propulsion system, I_{sp}. The specific impulse is defined as the thrust produced normalized by the weight of fuel flow as shown in Equation 2.1 [5, 6]. When comparing different propulsion systems, a higher I_{sp} is desired because this indicates more thrust is created per amount of fuel burned.

$$I_{sp} = \frac{F_{thrust}}{g_o * \dot{m}_f} \qquad \text{Equation 2.1}$$

Figure 2 depicts the specific impulse of various engine types plotted as a function of flight Mach number. The Mach number is defined as the flight velocity normalized by the local speed of sound, $a = \sqrt{\gamma RT}$ where γ is the ratio of specific heats of air, R is the gas constant for air, and T is the temperature of the air.

Figure 2 clearly indicates that as the Mach number increases, the most efficient air-breathing propulsion options are ramjets between about Mach 3-6 and scramjets from Mach 6 and higher [5]. Airbreathing engines have much higher I_{sp} than rockets because they do not have to carry an oxidizer since they use the oxygen in the air. This allows for an increased payload and better range. A more in-depth description of ramjet and scramjet engine concepts is given in the following sections.

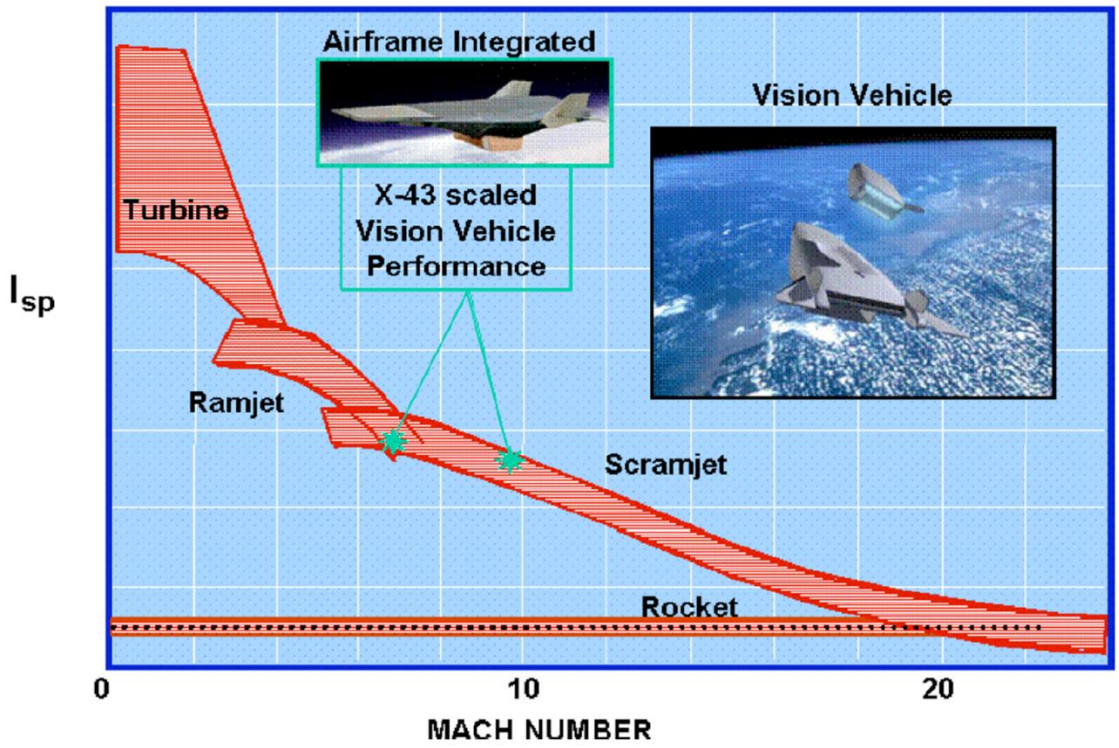

Figure 2: Comparison of Specific Impulse for Various Propulsion Systems [7]

2.1.1 The Ramjet

Ramjet and scramjet engines have been in development for many years [1, 2]. The concept of the ramjet is very simple. In fact, this engine concept contains no moving components. The conventional ramjet takes in air from a supersonic freestream and creates compression via a converging duct and a series of shock waves terminating in a normal shock wave that brings the flow to subsonic velocities [5]. After this compression process, combustion takes place by injecting fuel into the now subsonic airstream. The combustion products are then expanded through a converging-diverging nozzle back to supersonic velocities [5]. A schematic of a conventional ramjet is shown in Figure 3. The ramjet is suited specifically for flight Mach numbers in the 3-6 range [5, 8].

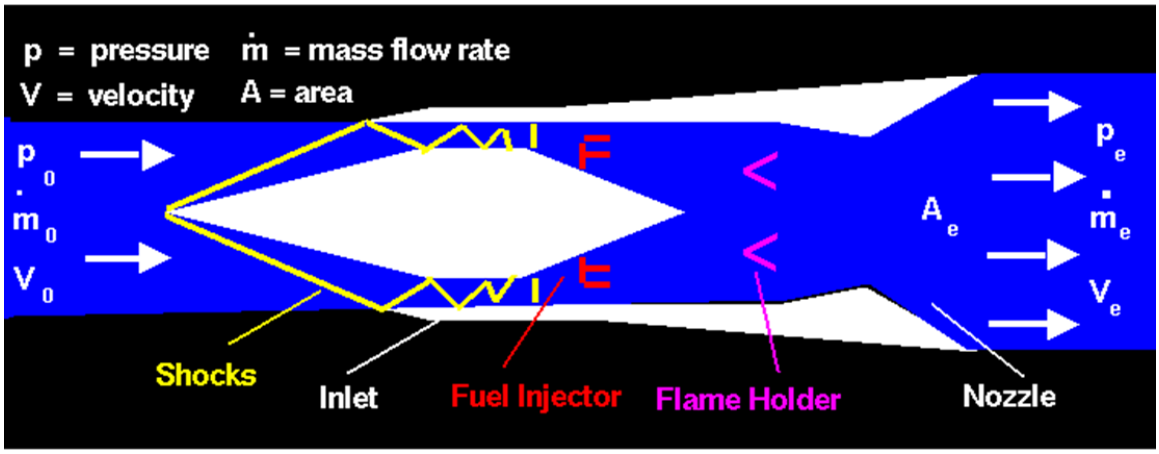

Figure 3: Schematic of a Ramjet Engine [9]

2.1.2 The Scramjet

The scramjet engine is similar to the ramjet engine in that it requires no moving components. The scramjet, which is short for supersonic combustion ramjet, was developed because as the flight Mach number increases, the losses due to decelerating to a subsonic flow become prohibitive. These losses can manifest themselves as total pressure losses, excessively high pressures and temperatures that make thermal-structural designs unfeasible, as well as loss of energy due to chemical processes [5]. The scramjet bypasses these issues by allowing combustion to take place in a supersonic airstream. The flow is compressed by a diffuser and a system of obliques shock waves but the normal shock creating subsonic flow does not exist [5]. After combustion takes place, the exhaust products are again expanded through a nozzle to produce thrust. A schematic of a scramjet engine was given in Figure 1. Scramjet engines are the best system for flight Mach numbers greater than about 6 [5].

2.1.3 Combined-Cycle Engines

The ramjet and scramjet engines, although suited for high Mach number flight, have a major drawback. This drawback is that because they rely on compression due to ram pressure from slowing a high-speed airstream, they cannot produce static thrust [1]. Therefore, a high-speed vehicle must incorporate a separate source of propulsion to get it to the takeover Mach numbers where the ramjet or scramjet can operate. This has given rise to Combined Cycle engine (CCE) concepts [1, 5]. These include Rocket-Based Combined

Cycle (RBCC) engines as well as Turbine-Based Combined Cycle (TBCC) engines [1]. These concepts apply a second propulsion system to allow the vehicle to reach the point at which the ramjet/scramjet can operate [1, 5].

2.1.4 Inlets for High-Speed Engines

The first component in all the high-speed engines discussed above is the inlet. Analyzing the inlet will be the focus of the current work. The inlet is responsible for providing a stream of compressed air to the combustor. Compression is critical for engine operation because the engine cycle operates with higher efficiency and produces more useful work at higher temperatures and pressures [10]. As important as inlets are, they also present large technical challenges, especially for high speed applications. Challenges include but are not limited to:

- High pressures and temperatures leading to material and structural design challenges [5, 11]
- Adverse pressure gradients that can lead to shock-boundary layer interaction (SBLI) causing performance losses [5]
- Shock train instabilities that can lead to inlet unstart [11]
- Operating at off-design conditions that can lead to reduced performance [5]

High-speed inlets can take on many forms. These include internal compression inlets, external compression inlets, or a combination of the two [5]. An external compression inlet is one in which compression is obtained through oblique shock waves that are set up by the inlet structure prior to entering the internal flow path [5]. A schematic of an external compression inlet using a system of oblique shock waves is shown below in Figure 4. The operation of the inlet is shown at the “shock on lip” condition. This indicates that the freestream flow conditions are such that the oblique shock waves are focused on the leading edge of the cowl [5]. The cowl is the point at which the flow transitions from external to internal. When the “shock on lip” condition is met, the inlet is operating at its design condition, because it maximizes the amount of air flow that enters the engine [5]. At off-design conditions, the shock waves are not focused on the lip which allows air to not enter the inlet leading to “spillage”. Spillage is thus the amount of air which is actually passing through the system compared to that which ideally could pass through the system [5].

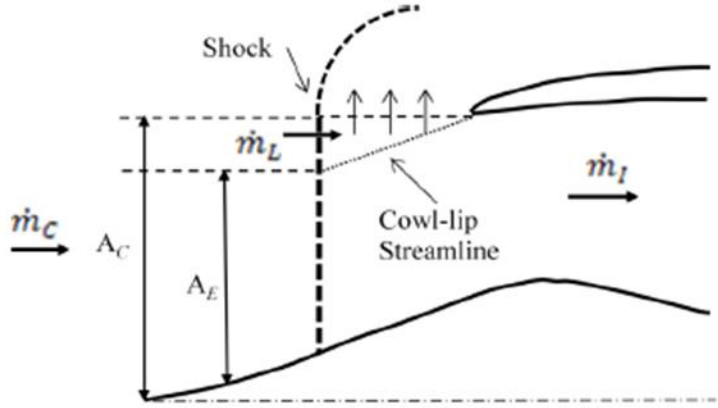

Figure 4: An Example of an External Compression Inlet [12]

Contrary to an external compression inlet, an internal compression inlet is one in which the compression takes place inside the internal flow path [5]. An example is shown below in Figure 5.

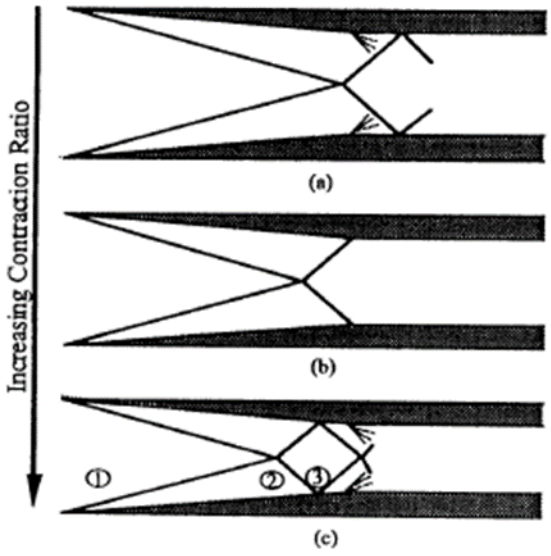

Figure 5: An Example of an Internal Compression Inlet [13]

Finally, an example of a mixed internal and external compression inlet is shown in Figure 6. As its name suggests, this type of inlet uses both shock waves created by the external portion of the inlet and a system of shock waves in the internal flow path to create the required final pressure rise [5].

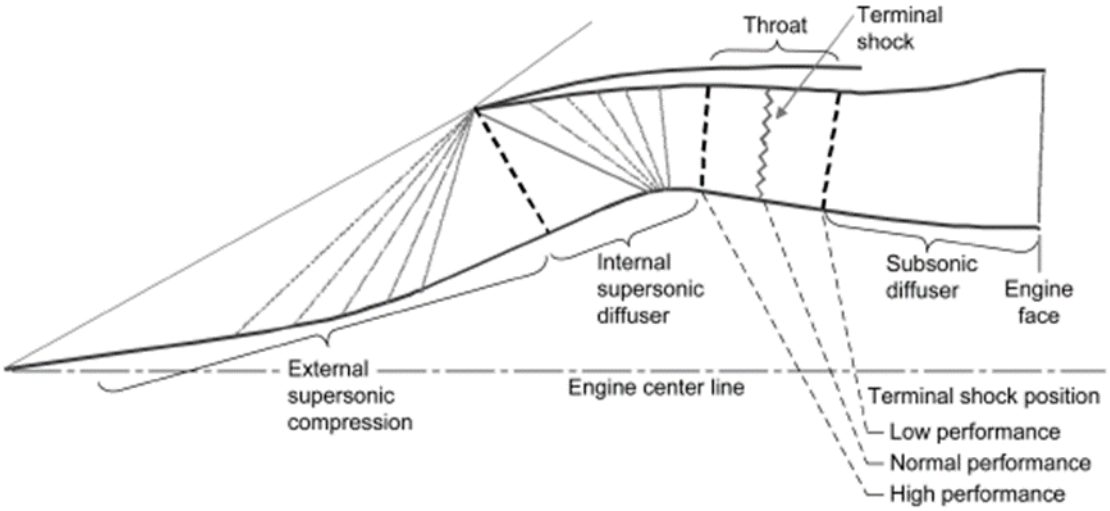

Figure 6: An Example of a Mixed Internal and External Compression Inlet [14]

2.2 Physical Phenomena Associated with High-Speed Inlet Design and Analysis

High-speed inlets include a range of physical challenges that are not present in low-speed inlets. For example, as the flow speeds exceed the speed of sound, shock waves develop that interact with the inlet walls giving rise to shock-boundary layer interactions. Also, the presence of the shock waves gives rise to the inlet starting problem. Once the inlet is started, meaning the shock train is internal to the inlet, the shock train is positioned based on engine operating conditions [5]. Violent changes in engine operation can occur as the shock train is ejected from the inlet leading to inlet unstart. Once the inlet is unstarted, there may exist a hysteresis or path dependency to restart it [15]. These physical features will be discussed in more detail in the following sections.

2.2.1 Shock-Boundary Layer Interaction

The operation of high-speed inlets necessarily includes the presence of shock waves. The presence of shock waves can lead to additional physical phenomena, specifically an inviscid-viscous interaction known as shock-boundary layer interaction. SBLI occurs when a shock wave interacts with the viscous boundary layer that develops along the solid surfaces of the inlet [5]. The most common interaction encountered in a high-speed inlet is the impinging shock interaction. As the boundary layer develops along the wall and a

shock wave from some external source (the cowl for example) impinges on the boundary layer, creating a complex interaction. In many cases a separation region is created because of the adverse pressure gradient created by the shock. Whether flow separation occurs, and the extent of the separation region depends on the properties of the boundary layer and whether it is laminar or turbulent [5, 16]. As the flow moves along the surface, momentum is lost due to viscous forces acting on the boundary layer leading to its inability to overcome the adverse pressure gradient [5]. This can lead to an inflection in the velocity profile and flow separation. Laminar boundary layers have less momentum near the wall than turbulent boundary layers, because the turbulent mixing helps sustain momentum by bringing in fluid with higher momentum from the edge of the boundary layer [5, 17].

It is important to note that this separation region extends ahead of the point where the shock would impinge on the wall in an inviscid flow calculation [18]. This is because the disturbances and pressure rise propagate upstream in the subsonic portion of the boundary layer [16, 18]. This separation bubble leads to the creation of additional shock waves. At the forward portion of the interaction, a separation shock is created because the separation bubble forces the flow to turn into itself. As the flow expands around the separation bubble an expansion wave is created until the flow reaches the wall and is again turned by a reattachment shock [18].

There are many reasons why shock-boundary layer interactions are so important for high-speed inlet operation. For example, SBLI can lead to significant increases in pressure and heat flux at the impingement and reattachment points thus causing thermal-structural concerns [5]. In addition, as mentioned above, shock-boundary layer interaction has the possibility of producing flow separation [5]. The flow separation can lead to local unsteady flow conditions [5, 11, 19, 20]. Further, separated flow reduces the flow-through area of the main supersonic core in the inlet and can lead to inlet unstart which is described in Section 2.2.3 [5].

2.2.2 Three-Dimensional Effects

The brief description of shock-boundary layer interaction given in the previous section suggests that the interaction is planar or two-dimensional. However, this is known to not be the case and three-dimensional effects play a significant role in the interaction, especially in rectangular ducts [20]. These effects are primarily due to the formation of separated flow regions in the corners of the duct. The viscous forces acting on the fluid from both a side wall and the duct floor lead to a significant reduction in momentum which makes the flow in the corners more susceptible to separation [21]. These separated regions are thought to induce additional shock and expansion waves that then enter the primary shock-boundary layer interaction and lead to changes in the structure of the interaction [21]. The corner separation causes the flow to be turned inward toward the duct centerline leading to the creation of a series of compression waves or a shock wave much the same way as described in Section 2.2.1. Then, as the flow rounds the separation bubble, a series of expansion waves are produced. As these waves propagate toward the centerline of the duct, they begin to alter the structure of the primary interaction region [21].

The location and size of the corner separations have been found to alter the structure of the shock-boundary layer interaction significantly. As the corner separation is moved forward, along with its induced waves, the separation length, defined as the distance between the separation point and the reattachment point along the centerline, is increased [21]. When the corner waves pass through the reattachment point of the ideal, planar, shock-boundary layer interaction, the maximum separation length is obtained [21]. Then the separation length is reduced as the waves move ahead of the reattachment line [21]. This trend is due to the pressure rise or drop induced by the corner compression or shock waves at the upstream side of the corner separation and the expansion waves on the downstream side of the corner separation. Depending on the location of these waves, they either add to the pressure rise due to the original planar interaction or they reduce the pressure rise [21].

Recently, computational work using large eddy simulation (LES), has uncovered additional three-dimensional phenomena in the impinging shock-boundary layer interaction case. For example, Ref. [22] identifies a secondary shock behind the main shock, caused by the presence of the sidewalls, that

eventually merges with the main shock causing it to take a curved shape. It is noted that this second shock has not been observed experimentally, possibly because of being masked from schlieren images [22]. Also, the separation bubble is predicted to increase and move forward for lower aspect ratio ducts as compared to large aspect ratio ducts because of the increased effect of the sidewalls [22].

In addition, not only are shock-boundary layer interactions three-dimensional in nature, but they also have an unsteady nature with low-frequency content, the cause of which is still yet to be determined [23]. The unsteadiness leads to motion and distortion of the separation shock [24].

2.2.3 Inlet Starting and Unstarting

Often, a high-speed inlet operation will be described as either started or unstarted. The inlet is considered started when the shock system is contained within the inlet [5]. This is the designed operating condition because mass flow through the inlet is maximized and drag is minimized since there is no spillage. To illustrate how the inlet reaches this design point, the inlet starting process will be described next. The description follows from [5] and [11] to which the reader is referred for additional details.

At subsonic speeds, the flow through the inlet is entirely subsonic. As the freestream Mach number increases, the flow remains subsonic except at the throat, the point of minimum area, where the Mach number reaches unity. Once the throat reaches Mach 1, the inlet is choked, and the maximum mass flow rate is obtained [25]. As the freestream Mach number continues to increase and becomes supersonic, a normal shock in front of the inlet forms and there is spillage around the inlet. This condition is termed subcritical. The normal shock is pushed back towards the inlet as the freestream Mach number is increased further. This mode is termed the critical operating point. Any increase past the critical Mach number pushes the shock wave inside of the inlet yielding the supercritical condition. Once the shock wave is inside of the inlet, the inlet is said to be started.

The inlet becomes “unstarted” if the shock train is ejected upstream from inside of the inlet [5]. This can occur for many reasons, for example, inviscid effects such as changes in freestream conditions like Mach

number or angle of attack or an increase in backpressure that forces the shock upstream towards the throat and eventually out of the inlet, and viscous effects such as boundary layer separation that causes excessive blockage [5]. The unstart process is a very violent and rapid transient process that significantly reduces the engine performance and can be detrimental to the vehicle by causing combustion to be interrupted leading to the loss of the vehicle [26].

In scramjet engines at lower hypersonic Mach numbers, heat release in the combustor causes strong pressure waves that propagate upstream [5]. To minimize interaction with the inlet, a long duct is introduced. This “isolator” contains a series of oblique waves, called a shock train, as was visible seen in Figure 1. The isolator is used to allow the shock train to adjust to backpressure changes without unstarting the inlet [5]. The focus of this work will be the inlet. For additional information about isolators, the reader is referred to Ref [5].

The starting and unstarting processes discussed above can be further complicated by the presence of hysteresis [5]. Hysteresis in an inlet generally manifests itself as a path-dependency of the inlet start and unstart characteristics. That is, after an inlet is unstarted by a process, whether this is due to contraction ratio or backpressure, simply reversing the process will not necessarily lead to the inlet restarting at the same point that it unstarted [15].

3 Review of Relevant Previous Works

3.1 Development of Inlets with Variable Geometry

The concept of variable geometry inlets has existed for some time. The first uses of variable geometry inlet designs targeted inlets for supersonic cruise aircraft to tailor the inlet for better off-design performance [27]. These designs included variable ramp positions for two-dimensional, planar inlets, and collapsing and translating center bodies for axisymmetric inlets [27]. These concepts were both tested as part of supersonic transport aircraft development in the mid-1960s [28, 29], as noted in [27].

As the development of the ramjet, and later the scramjet, matured, the use of variable geometry was applied to make these engines operable over a wider range of flight conditions than a fixed geometry inlet could provide. In fact, variable geometry, for both inlet and nozzle operations, has been cited as part of the top ten enabling technologies for ramjet propulsion [1]. Extensive experimental work was conducted to develop an understanding of mixed-compression, variable geometry inlets. An example is the work of Reference [3] which focused on performance characterization of a rectangular inlet with a variable geometry cowl. This work will be presented in more detail in Section 3.4 as it is the focus of the current computational study.

As mentioned previously, a major goal of including variable geometry in an inlet design is to increase the range of operability of the inlet [1]. However, even variable geometry inlets cannot provide design point operation over the entire flight range of a vehicle, so they will also see off-design conditions. Reference [30] investigated the off-design performance of a scramjet engine with a fixed-geometry and a variable-geometry inlet designed for use at Mach 8. The goal of the incorporation of variable geometry in this work was to maintain the shock-on-lip condition. The variable geometry was introduced by a translating cowl to cancel the final inlet shock so that there were no shocks entering the isolator. They noted that a fixed-geometry inlet would lead to subpar performance over a significant portion of the flight envelope because of the need to design the combustor for lower Mach number operation to ensure thermal choking does not occur. The variable geometry inlet concept presented was cited as not being optimal for performance. It is interesting to note that they suggested a rotating cowl, as will be presented in the current study, to provide better performance at extremes of the flight envelope.

Even more recently, the development of Combined-Cycle-Engines (CCE) has received much attention. These inlet concepts, designed for high-speed cruise vehicles that must operate from subsonic take-off conditions to supersonic or hypersonic cruise conditions [1], inherently include variable geometry. For example, Reference [31] presents the design of a "over-under" dual flow path combined cycle engine consisting of a turbine and a scramjet. The flow paths are separated by a variable geometry low speed cowl that closes off the low-speed flow path during scramjet operation. The high-speed flow path also includes a rotating cowl. Additional variable geometry ramps are used to allow the engine to be tailored to a range of flight conditions and to ensure properly conditioned airflow is provided to the turbine. Similar designs are presented and analyzed in References [32] and [33].

3.2 Inlet Unstart Analysis: Experimental Studies

Numerous experimental investigations have been conducted on varying inlet geometries to assess the effect of unstart caused by both backpressure and contraction ratio. The majority of unstart studies have focused on the effect of backpressure on the shock train stability and inlet unstart. Examples of this are found in References [3, 26, 34, 35, 36, 37]. In particular, the work of Wagner, et.al. [37] conducted an experimental investigation of the unstart of a rectangular inlet due to backpressure caused by the closing of a flap at the exit of the inlet. The test was conducted in the Mach 5 blow-down facility at the University of Texas at Austin. They used high-speed schlieren to obtain video images of the unstart process as well as pressure measurements from Kulite sensors. With these techniques, they were able to identify the mechanisms of unstart as flow separation that led to increased blockage that eventually chokes the inlet into unstart. Once the inlet unstarted, they noted that there were several different modes of unstart: a large-amplitude oscillation mode, a small-amplitude oscillation mode, and a non-oscillation mode. The need for additional work was cited to fully understand the mechanisms driving these different modes.

In a similar study, Zhang, et.al. [26], also studied the unstart due to backpressure of a rectangular inlet and identified multiple modes of unstart. The rectangular inlet studied was designed for a shock-on-lip Mach number of 6.0. They investigated unstart processes at Mach 5.0, below the design point, at Mach 6.0, at the design point, and at Mach 7.0, above the design point. This led to substantial differences in the unstart

process and the resulting unstarted flow. At and below the design Mach number of the inlet, the unstart process was created by the shock train moving upstream toward the inlet entrance, eventually to the point where the first shock in the shock train began to interact with the cowl shock, leading to an increase in the size of the boundary layer separation on the ramp side of the inlet. As the separation increased, it led to significant flow blockage and unstarted the inlet as the shock moved out of the inlet to allow for flow spillage. This unstart process led to a large amplitude oscillation in the flow driven by the growth and decline of the separated flow region. On the other hand, above the design Mach number, the shock train was situated such that the cowl shock sat on the shoulder of the inlet ramp and did not cause significant boundary layer separation. The result of this was a shear layer with subsonic flow on the cowl-side of the inlet and supersonic flow on the ramp-side. As the inlet became unstarted, the flow was not driven by the separated flow dynamics but instead by the fluctuations of the shock train on the ramp side. Thus, the oscillations in the unsteady flow were decreased. These works again highlight the highly complex, three-dimensional flow during and after inlet unstart.

The previous studies are focused on unstart that is driven by an inviscid mechanism, namely backpressure. However, additional studies have been conducted to investigate unstart caused by other means that are viscous in nature. For example, Ref. [38] investigated the effect of mass injection on unstart to assess the impact of boundary layer thickness and separation on inlet operability. In addition, there have been studies that have investigated the impact of contraction ratio on inlet unstart. This can be considered a combination of both inviscid and viscous phenomena [37]. This is because the shock-boundary layer interactions induced by the inlet cowls can play a large role in the unstart in the form of boundary layer separation as discussed in Sections 2.2.1 and 2.2.2. Less work has been conducted in this area but References [3, 36, 39] provide good examples. In particular, Rodi et.al. [36], conducted an experimental test of a planar inlet with a rotating cowl very similar to that which will be considered in the current work. The goal of that study was to characterize the pressures in the inlet just prior to, during, and after the inlet unstart occurs. The unstart was driven by contraction ratio by rotating the cowl and then in a separate run by backpressure due to a downstream flap, similar to that discussed previously for comparison. The results showed that both unstart

mechanisms lead to similar pressure fluctuations and oscillatory unstarted flowfields; however, the magnitudes of the fluctuations and oscillations were slightly different between the two cases.

3.3 Inlet Unstart Analysis: Computational Studies

With the increase in availability of computing resources, Computational Fluid Dynamics (CFD) has played an increasingly important role in the design and analysis process [40, 41]. Accordingly, there has been significant work on using CFD to analyze ramjet and scramjet engines. CFD is vital for the analysis of high-speed inlets because of the detailed flowfield calculations that are possible even in complex geometries. It also allows for study at conditions that may not be achievable in ground test facilities [42] and for data acquisition that may be difficult, costly, or impossible to obtain with experimental measurements. Most commonly, steady state or quasi-steady CFD is used. The steady state and/or quasi-steady assumption is that the flow timescales are small compared to any transient timescale that may exist. Steady-state CFD is often used to obtain static pressure distributions (Ref. [5]), heat transfer predictions (Ref. [5]), performance calculations with varying levels of backpressure (Ref [43]), and assessments of how combustion affects the inlet performance (Ref [44]).

In some of the cases just mentioned, the steady-state assumption is valid. However, there are many cases where a transient analysis is necessary. As has been mentioned before, this includes inlet unstart and any associated hysteresis effects. Transient CFD analysis of inlets has been conducted, but to a much lesser extent compared to steady-state CFD. This is primarily due to the sharply increased computational cost. However recently, there has been a more intense focus on transient analysis of inlet unstart, especially with respect to backpressure induced unstart. Early work in the area focused on inviscid Euler computations for unstart analysis like in Ref. [45]. However today, full Navier-Stokes computations are utilized. For example, Neaves, et.al. [46] conducted a three-dimensional computational analysis of the inlet of Ref. [3], the same inlet considered in the current work, using an implicit solver with an adaptive mesh routine to analyze the backpressure unstart due to the closing of the throttling device. They noted that three-dimensional computations were necessary due to effects like those discussed in Section 2.2.2. From these

computations, they were able to compute the change in shock train position that eventually led to larger separation regions and inlet unstart. The computed unstart time was cited as only about 5.74 milliseconds. In addition, Hoeger [47] applied steady-state and transient CFD methods in two- and three-dimensions to characterize the effect of backpressure on the shock train development and unstart in a rectangular inlet-isolator configuration. Also, Riley and Gaitonde [48, 49] and Yentsch and Gaitonde [50, 51] have recently applied transient CFD methods incorporating unsteady Reynolds-averaged Navier-Stokes (URANS) solutions to the problem of inlet unstart and mode transition of dual-mode ramjets with fixed geometry.

Similar to the experimental analysis of inlet unstart, backpressure induced unstart has generally accounted for the majority of the computational work in unstart analysis. Investigations into the contraction ratio or cowl-induced unstart have been treated to a lesser degree. However recently, with the interest in Combined-Cycle Engines (CCE), which generally include multiple flow paths with variable geometry cowls and splitters, this area of focus is beginning to receive more attention. Some recent relevant works in this area can be found in Refs. [52, 53, 54]. In particular, the work of Grainger et.al. [52], used two-dimensional, transient CFD methods with overset meshes to analyze the starting characteristics of an inlet with a sliding door geometry that was tested experimentally. They looked at different speeds at which the door was opened and found that the geometry and path that the doors took had an impact on what door speeds allow the inlet to become started. Once the inlet was started, they also computed the transient response of the inlet due to unstart caused by backpressure.

Also, Xianhong, et.al. [53] used a 2D, transient CFD model with an overset, dynamic grid approach to investigate the mode transition of a Turbine-Based Combined Cycle Engine (CCE). They did not investigate unstart in particular but found that a transient simulation with cowl and splitter motion led to different flowfields as compared to a steady state analysis at the same geometric configuration. In addition, even computations with different rotation rates led to different flowfields. This can be considered a type of hysteresis. The works discussed highlight the complex interactions between shock waves and the turbulent boundary layer, as well as backpressure due to combustion, that lead to inlet unstart.

3.4 Current Research Focus

The review just given highlights the fact that inlet unstart analysis has primarily been approached through experimental studies. The use of CFD is only now beginning to be used to investigate the problem. In both experiment and computation, the majority of the work has focused on backpressure induced unstart, whereas contraction ratio unstart due to variable geometry has received less attention.

This work will attempt to bolster the knowledge of contraction ratio unstart in variable-geometry inlets. Hence, the focus of the current work is to extend the use of transient CFD to gain understanding in the unstart process of inlets with variable geometry, thus contributing additional insights and data to the knowledge base of inlet unstart in the area of variable geometry, rotating cowl geometries. To do this, the inlet configuration of Ref. [3] is analyzed using Computational Fluid Dynamics to assess its performance in capturing the transients due to the rotation of the variable geometry cowl. Ref. [3] was an extensive parametric experimental study of a combination of inlet cowl and isolator configurations that consisted of 250 geometry configurations [3]. The goal of the study was to obtain experimental data that could be used for a database to predict inlet performance.

The geometries tested were at 2% scale of what an inlet on a generic hypersonic vehicle would be. The inlet was planar and consisted of an inlet compression ramp, a rotating cowl, sidewalls, an isolator section, and a diffuser section. The inlet is shown schematically in Figure 7. The inlet width was 2.0 inches and the throat height was 0.4 inches which led to an aspect ratio of 5.0. The inlet ramp was 9.77 inches long with an 11° angle from the horizontal to provide compression. There were three different cowls tested, each with different lengths: long, medium, and short. The long cowl was 4.4 inches in length (L_c/H_{th} = 11.00), the medium cowl was 3.9 inches in length (L_c/H_{th} = 9.75), and the short cowl was 2.5 inches in length (L_c/H_{th} = 6.25). All configurations consisted of mixed external and internal compression. External compression was due to the oblique shock wave emanating from the leading edge of the inlet ramp. Internal compression was achieved by an oblique shock train initiated by the cowl leading edge. For the long cowl, a three-shock system was developed, and for the medium and short cowls a two-shock system was developed as depicted in Figure 8. The cowls were actuated so that they could be rotated about a hinge. The

cowl angle from the horizontal was defined as θ_c. Another angle defining the cowl rotational position was the cowl convergence angle β, defined as the angle between the cowl and the inlet ramp. Since the inlet ramp angle was fixed at 11°, the geometric relationship between the cowl angle (from the horizontal) and the cowl convergence angle was $\beta = 11° - \theta_c$. The cowls could be rotated between angles of $\theta_c = 0$ deg (horizontal) to 11 deg (parallel to ramp). Following the throat and isolator section was a 20° diffuser ramp that led into a constant area rectangular duct. At the end of the duct was a throttling device that could be used to backpressure the inlet.

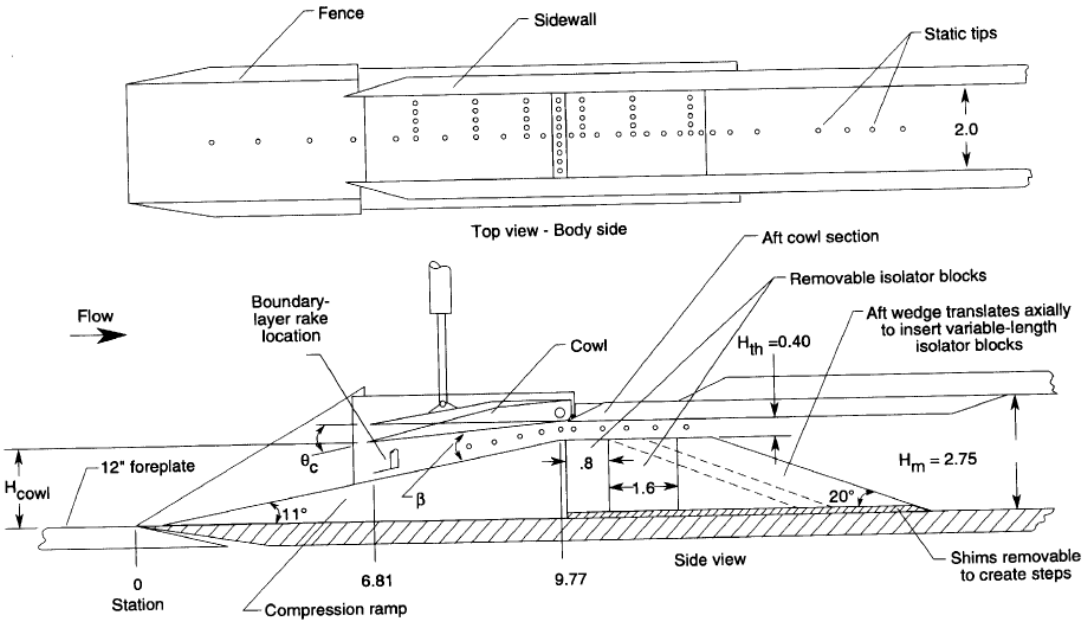

Figure 7: Schematic of the Rectangular Inlet of Ref. [3] Used in the Current Computational Study

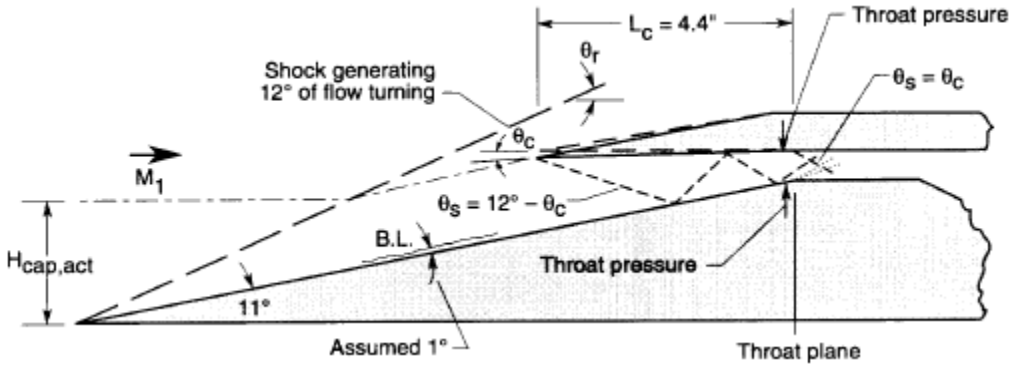

Figure 8: Shock System Developed for the Inlet with the Long Cowl from Ref. [3]

In addition to different cowl configurations, the study also tested various isolator designs and lengths. First, a simple constant area isolator was used. Next, an isolator with a constant area and a 6° expansion was used. The isolator lengths were 1.08 inches (L/H_{th} = 2.7), 1.88 inches (L/H_{th} = 4.7), 3.48 inches (L/H_{th} = 8.7) and 6.68 inches (L/H_{th} = 16.7). After each isolator, a 20° diffuser section was used. Each cowl and isolator was also tested with and without rearward facing steps to be representative of fuel injector features. The steps were not included in the current computations, so they will not be addressed further here.

The inlet was instrumented with 110 wall static pressure taps on the inlet ramp, sidewalls, cowl, and isolator. No dynamic pressure sensors were included. The effect of the boundary layer was obtained by testing with and without at a 12-inch foreplate positioned ahead of the inlet ramp. The foreplate allowed for the growth of a thicker boundary layer entering the inlet as compared to not including the plate.

The experimental work was conducted in the NASA Langley Research center Mach 4 Blowdown Facility (M4BDF). The tunnel had a test section that was 9 inches by 9 inches in cross section and about 15 inches long [3]. The evaluation of the inlet geometries was conducted at nominal test conditions of P_t = 200 ± 2 psia and M = 4.03 ± 0.02. The static pressure in the test section was P = 1.266 ± 0.034 psia while the static temperature ranged between T = 500 R ± 3 R to 540 R ± 3 R.

4 Analysis Approach

To conduct the analysis of transient flow features in the variable geometry inlet test case, a computational study is performed using the commercial CFD code CFD++ provided by Metacomp Technologies. The code is capable of solving incompressible and compressible flows, inviscid and viscous flows, and also has additional capabilities to include chemical reactions. It can compute solutions on both structured and unstructured meshes and can accommodate overset meshes which will be used in this work.

4.1 Governing Equations

To analyze the flow in a high-speed inlet, the Navier-Stokes equations which govern compressible, viscous flow are solved numerically. The Navier-Stokes equations are a set of nonlinear, partial differential equations that are of mixed hyperbolic and parabolic nature in transient form and mixed hyperbolic and elliptic nature in steady-state form [16]. The derivation of these equations can be found in numerous references focusing on fluid dynamics, compressible flow, and CFD [16, 18, 25, 40, 55, 56]. The differential form of the Navier-Stokes equations is given below in vector form using a cartesian coordinate system in Equations 4.1 – 4.5 [40]. The first row of each vector corresponds to the continuity equation. The following three rows are the three components of the momentum equation. The last row then corresponds to the energy equation. In this case, the energy equation is given in terms of the total energy, that is the sum of internal energy and kinetic energy, defined as $E_t \equiv e + \frac{1}{2}V^2$ [16].

$$\frac{\partial \boldsymbol{U}}{\partial t} + \frac{\partial \boldsymbol{E}}{\partial x} + \frac{\partial \boldsymbol{F}}{\partial y} + \frac{\partial \boldsymbol{G}}{\partial z} = 0 \qquad \text{Equation 4.1}$$

$$\boldsymbol{U} = \begin{bmatrix} \rho \\ \rho u \\ \rho v \\ \rho w \\ E_t \end{bmatrix} \qquad \text{Equation 4.2}$$

$$\boldsymbol{E} = \begin{bmatrix} \rho u \\ \rho u^2 + p - \tau_{xx} \\ \rho uv - \tau_{xy} \\ \rho uw - \tau_{xz} \\ (E_t + p)u - u\tau_{xx} - v\tau_{xy} - w\tau_{xz} + q_x \end{bmatrix} \qquad \text{Equation 4.3}$$

$$\boldsymbol{F} = \begin{bmatrix} \rho v \\ \rho uv - \tau_{xy} \\ \rho v^2 + p - \tau_{yy} \\ \rho vw - \tau_{yz} \\ (E_t + p)v - u\tau_{xy} - v\tau_{yy} - w\tau_{yz} + q_y \end{bmatrix} \quad \text{Equation 4.4}$$

$$\boldsymbol{G} = \begin{bmatrix} \rho w \\ \rho uw - \tau_{xz} \\ \rho vw - \tau_{yz} \\ \rho w^2 + p - \tau_{zz} \\ (E_t + p)w - u\tau_{xz} - v\tau_{yz} - w\tau_{zz} + q_z \end{bmatrix} \quad \text{Equation 4.5}$$

The terms τ_{ij} are the components of the viscous stress tensor and are given in Equations 4.6 – 4.11. In these equations, μ is the molecular viscosity and λ is the second viscosity coefficient or bulk viscosity coefficient. Stoke's Hypothesis, which calls for $\lambda = -\frac{2}{3}\mu$, is generally used [16, 18]. The terms q_i are the components of the heat flux vector, given in Equations 4.12 – 4.14 using Fourier's Law.

$$\tau_{xx} = 2\mu\frac{\partial u}{\partial x} + \lambda\left(\frac{\partial u}{\partial x} + \frac{\partial v}{\partial y} + \frac{\partial w}{\partial z}\right) \quad \text{Equation 4.6}$$

$$\tau_{yy} = 2\mu\frac{\partial v}{\partial y} + \lambda\left(\frac{\partial u}{\partial x} + \frac{\partial v}{\partial y} + \frac{\partial w}{\partial z}\right) \quad \text{Equation 4.7}$$

$$\tau_{zz} = 2\mu\frac{\partial w}{\partial z} + \lambda\left(\frac{\partial u}{\partial x} + \frac{\partial v}{\partial y} + \frac{\partial w}{\partial z}\right) \quad \text{Equation 4.8}$$

$$\tau_{xy} = \tau_{yx} = \mu\left(\frac{\partial u}{\partial y} + \frac{\partial v}{\partial x}\right) \quad \text{Equation 4.9}$$

$$\tau_{xz} = \tau_{zx} = \mu\left(\frac{\partial w}{\partial x} + \frac{\partial u}{\partial z}\right) \quad \text{Equation 4.10}$$

$$\tau_{yz} = \tau_{yz} = \mu\left(\frac{\partial v}{\partial z} + \frac{\partial w}{\partial y}\right) \quad \text{Equation 4.11}$$

$$q_x = k\frac{\partial T}{\partial x} \quad \text{Equation 4.12}$$

$$q_y = k\frac{\partial T}{\partial y} \quad \text{Equation 4.13}$$

$$q_z = k\frac{\partial T}{\partial z} \quad \text{Equation 4.14}$$

The Navier-Stokes equations are closed with equations of state that relate the thermodynamic variables to themselves [40]. For the work considered here, the ideal gas law of Equation 4.15 suffices as there are no high temperature effects leading to dissociation or ionization and the effect of intermolecular forces

between molecules are negligible at the conditions of the experiments [40]. By using the ideal gas law, the gas is considered to be thermally perfect; however, it is not calorically perfect as the specific heats are computed using the curve fits of Ref. [57] that are a function of temperature as shown in Equation 4.16.

$$p = \rho RT \qquad \text{Equation 4.15}$$

$$c_v = f(T) \text{ and } c_p = f(T) \qquad \text{Equation 4.16}$$

The above equations govern the flow of a gaseous fluid that is either laminar or turbulent subject to the applied boundary conditions. However, turbulence is necessarily three-dimensional and unsteady and exists over an extremely large range of length and time scales [16, 20, 58]. To solve the full Navier-Stokes equations for a turbulent flow (this is generally known as Direct Numerical Simulation or DNS) is not a tractable problem for the Reynolds numbers of interest in the current study [20, 40]. To make the problem manageable, the fluid variables, including the fluid density and velocity components, etc., are decomposed into an average or mean flow component and a fluctuating component [16, 58]. For incompressible flows, this is the well-known Reynolds-averaging process. For compressible flows, the analogous process is known as mass-averaging or Favre-averaging. For compressible flows, the Favre-averaging includes mass averaged variables which leads to further simplifications of the Navier-Stokes equations than could be obtained from simply applying a Reynolds-averaging technique [20]. In doing either of these averaging processes, additional unknowns are introduced into the governing equations [20]. These unknowns are related to "stresses" created by turbulent fluctuations. To finally close the system of equations these Reynolds stresses, as they are known, must be modeled by additional turbulence modeling equations [20]. This will be discussed in the next section.

4.2 Turbulence Models

The result of applying the averaging processes to the Navier-Stokes equations is the Reynolds-averaged Navier-Stokes (RANS) equations or the Favre-averaged Navier-Stokes (FANS) equations. It should be noted that despite the fact that the Favre-averaging process is used for compressible flows, the equations are generally still referred to as the RANS equations.

To close the system of equations, a turbulence model that solves for the appropriate turbulent parameters is needed [58]. In general, no single turbulence model will be appropriate for every flow [58]. In this work, a series of turbulence models was assessed and compared to the experimental results of Ref [3]. These are the Spalart-Allmaras model, the Menter SST model, the Realizable k-ε model, the Cubic k-ε model, and a Reynolds Stress model. The formulations of these models are given below. It should be noted that the models described are by no means an exhaustive list, but they were chosen instead because of their wide-spread use in the CFD community and their applicability for the current problem of study.

Two types of turbulence models will be discussed, models that rely on the Boussinesq Approximation and those that do not [40]. The Boussinesq Approximation assumes that the Reynolds stresses are proportional to the strain rate of the mean flow by means of an eddy viscosity coefficient as shown below in tensor notation in Equation 4.17 [40, 59]. In this equation, the indices i and j denote the Cartesian coordinate directions, x, y, and z, $\overline{-\rho u_i' u_j'}$ is the tensor of Reynolds stresses, S_{ij} is the mean strain rate, k is the turbulent kinetic energy, and μ_T is the turbulent eddy viscosity. The Boussinesq Approximation results from an analogy of the transport due to random molecular motion [59].

$$\overline{-\rho u_i' u_j'} = 2\mu_T S_{ij} - \frac{2}{3}\left(\mu_T \frac{\partial u_k}{\partial x_k} + \rho k\right) \qquad \text{Equation 4.17}$$

The Boussinesq type turbulence models solve additional equations to ultimately determine the turbulent viscosity. Higher-order models that do not rely on the Boussinesq Approximation solve transport equations for the Reynolds stresses directly. These models are known as second-moment closure models or Reynolds Stress models [40]. Only a brief description of the major aspects of each model will be given here. For detailed information about each model and how it is implemented in CFD++, the reader is referred to Ref. [60].

4.2.1 One-Equation Models

A one-equation turbulence model adds a partial differential equation to the Navier-Stokes system governing the evolution of a turbulent quantity [40]. One-equation models are also considered to be “incomplete”, because they rely on associating the turbulent length scale to a length scale of the mean flow [59]. The most

common one-equation model, and the only one-equation model considered in this work, is the Spalart-Allmaras model [61]. The implementation of the model in CFD++ is given below.

The Spalart-Allmaras one-equation model solves a single partial differential equation to determine the kinematic eddy viscosity through a turbulent working variable, $\tilde{\nu}$ [60, 61]. It is a local model, meaning that the evolution of the turbulence is not considered [59, 61]. The relationship between the working variable and the kinematic eddy viscosity is given below in Equation 4.18, and the transport equation for the working variable is given in Equation 4.19 [60]. The particular model constants and additional relationships for the different f functions are given in Ref. [60].

$$\nu_T = \tilde{\nu} f_{\nu 1} \qquad \text{Equation 4.18}$$

$$\frac{\partial}{\partial x_j}\left(u_j \tilde{\nu}\right) = c_{b1} f_{r1} (1 - f_{t2}) \tilde{S} \tilde{\nu} + \frac{1}{\sigma}\{\nabla \cdot [(\nu + \tilde{\nu}) \nabla \tilde{\nu}] + c_{b2} (\nabla \tilde{\nu})^2\} - \left(c_{w1} f_w - \frac{c_{b1}}{\kappa^2} f_{t2}\right)\left(\frac{\tilde{\nu}}{d}\right)^2 + f_{t1} \Delta U^2 \qquad \text{Equation 4.19}$$

4.2.2 Two-Equation Models

As mentioned previously, one-equation turbulence models are considered to be "incomplete" because they require a relation between the turbulent length scale and the mean flow. Two-equation models include two partial differential equations, one for the turbulent kinetic energy and one for the turbulent length scale or a similar quantity. Therefore, two-equation models are considered to be more "complete" [59]. Two-equation models still rely on the assumption that the turbulence variables are related to the mean strain rate through the eddy viscosity (Boussinesq Approximation), but they attempt to add in the influences related to the history of the flow development [59]. Again, there are many different two-equation turbulence models. This work focused on three common models, the Realizable *k*-*ε* model, the Cubic *k*-*ε* model, and the Menter SST model.

The Realizable *k*-*ε* model is a two-equation model that solves transport equations for the turbulent kinetic energy and the turbulent dissipation rate shown in Equations 4.20 and 4.21 [60]. The turbulent kinetic energy is the energy associated with the turbulent fluctuations, defined for compressible flow as $\rho k \equiv$

$\frac{1}{2}\overline{u_\iota' u_\iota'}$ and the dissipation rate is the rate at which turbulent kinetic energy is dissipated into heat, defined for compressible flow as $\rho\epsilon \equiv \overline{t_{j\iota}\,\partial u_\iota'/\partial x_j}$ [59]. In this definition, t_{ji} are the viscous stresses [59].

$$\frac{\partial \rho k}{\partial t} + \frac{\partial}{\partial x_j}\left(u_j \rho k\right) = \frac{\partial}{\partial x_j}\left[\left(\mu + \frac{\mu_t}{\sigma_k}\right)\frac{\partial k}{\partial x_j}\right] + P_k - \rho\epsilon \qquad \text{Equation 4.20}$$

$$\frac{\partial \rho \epsilon}{\partial t} + \frac{\partial}{\partial x_j}\left(u_j \rho \epsilon\right) = \frac{\partial}{\partial x_j}\left[\left(\mu + \frac{\mu_t}{\sigma_\epsilon}\right)\frac{\partial \epsilon}{\partial x_j}\right] + (C_{\epsilon 1}P_k - C_{\epsilon 2}\rho\epsilon + E)T_t^{-1} \qquad \text{Equation 4.21}$$

In the above equations, P_k is the production of turbulent kinetic energy and T_t is a turbulence time scale [60]. The model seeks to improve performance in cases with adverse pressure gradients by including the variable E in the ε equation [60]. See Ref. [60] for additional details and for the model constants that are used in CFD++. The eddy viscosity used in the Boussinesq Approximation of Equation 4.17 is calculated as $\mu_T = \min\left(C_\mu f_\mu \rho k^2/\epsilon\ , \phi\frac{\rho k}{S}\right)$ where ϕ, S,C_μ, and f_μ are given in Ref. [60].

The Cubic *k*-ε model uses the same transport equations for *k* and ε as given in Equations 4.20 and 4.21 for the Realizable *k*-ε model. The non-linearity is incorporated by adding additional, higher-order expansion terms to the original linear Boussinesq eddy viscosity [60]. The eddy viscosity is then determined as $\mu_t = C_\mu f_\mu \bar{\rho}\tilde{k}^2/\tilde{\epsilon}$ where C_μ, f_μ are defined in Ref. [60]. The Reynolds stresses are determined from a nonlinear relation with the mean strain rate.

The other two-equation model considered here is the Menter SST model which combines aspects of both a *k*-ε model and a *k*-ω model. The *k*-ω model solves a transport equation for ω, the specific dissipation rate, defined as $\omega \equiv \epsilon/k$ [58]. The *k*-ε model is used for free shear layers and the *k*-ω model is used in the near wall region [60]. A blending function is used to transition between the models. The transport equations for the turbulence kinetic energy and turbulent dissipation time scale, ω, are given below [60].

$$\frac{\partial(\rho k)}{\partial t} + \frac{\partial}{\partial x_j}\left(u_j \rho k\right) = \widetilde{P_k} - \beta^* \rho k\omega + \nabla\cdot[(\mu + \sigma_k\mu_t)\nabla k] \qquad \text{Equation 4.22}$$

$$\frac{\partial(\rho\omega)}{\partial t} + \frac{\partial}{\partial x_j}\left(u_j \rho \omega\right) = \frac{\gamma}{\widetilde{\nu_t}}P_k - \beta\rho\omega^2 + \nabla\cdot[(\mu + \sigma_\omega\mu_t)] + 2(1-F_1)\rho\sigma_{\omega 2}\frac{1}{\omega}\nabla k\cdot\nabla\omega \qquad \text{Equation 4.23}$$

In the above, the production of kinetic energy is limited to $\widetilde{P_k} = \min(P_k, 10\beta^*\rho k\omega)$, where P_k is the production term as given in Ref. [60]. The model constants for the *k*-ε model and a *k*-ω model are blended as $\phi = F_1\phi_1 + (1 - F_1)\phi_2$, where ϕ_1 and ϕ_2 represent the respective model constants. The blending function is given as,

$$F_1 = \tanh\left\{\left(min\left[max\left(\frac{\sqrt{k}}{\beta^*\omega d}, \frac{500\nu}{d^2\omega}\right), \frac{4\rho\sigma_{\omega 2}k}{CD_{k\omega}d^2}\right]\right)^4\right\} \quad \text{Equation 4.24}$$

From these transport equations, the turbulent eddy viscosity is found as $\nu_t = a_1 k / \max(a_1\omega, SF_2)$ where the second blending function is given in Equation 4.25.

$$F_2 = \tanh\left\{\left[\max\left(\frac{2\sqrt{k}}{\beta^*\omega d}, \frac{500\nu}{d^2\omega}\right)\right]^2\right\} \quad \text{Equation 4.25}$$

CFD++ also implements a limit on the eddy viscosity such that $\widehat{\nu_t} = \max(\nu_t, 10^{-8})$ in the dissipation equation [60].

4.2.3 Higher-Order Models

The models above all relied on the Boussinesq Approximation. However, second-moment closure models were developed to bypass this assumption and solve transport equations for the Reynolds stresses directly. This approach requires the addition of seven partial differential equations, one for each of the six components of the Reynolds stress tensor and an additional turbulent quantity. There is obviously additional computational cost associated with this; however, this formulation inherently accounts for curvature of streamlines, changes in strain rate, and secondary flows [59]. The second-moment closure model in CFD++ is a seven-equation model that solves a transport equation for each of Reynolds stresses and an equation for the dissipation rate. The transport equation for the Reynolds stresses is given in Equation 4.26, where P_{ij} is the production term, d_{ij} is the diffusion term, ϕ_{ij}^* is the pressures-strain term, and ϵ_{ij} is the dissipation term [60]. These terms are all tensors. The transport equation for the homogeneous dissipation rate is given in Equation 4.27 [60].

$$\frac{\partial \overline{\rho u_i' u_j'}}{\partial t} + \frac{\partial \overline{\rho u_i' u_j' u_k}}{\partial x_j} = P_{ij} + d_{ij} + \phi_{ij}^* - \epsilon_{ij}$$ Equation 4.26

$$\frac{\partial \bar{\rho}\widetilde{\epsilon^*}}{\partial t} + \frac{\partial \bar{\rho}\widetilde{\epsilon^*}\tilde{u}_k}{\partial x_k} = \frac{\partial}{\partial x_l}\left[\left(\tilde{\mu}\delta_{lk} + C_\epsilon \bar{\rho}\widetilde{u_l' u_k'}\frac{\tilde{k}}{\tilde{\epsilon}}\right)\frac{\partial \widetilde{\epsilon^*}}{\partial x_k}\right] + \frac{C_{\epsilon 1}\bar{\rho}P_k}{\tau} - \frac{C_{\epsilon 2}\bar{\rho}\widetilde{\epsilon^*}}{\tau} - \frac{C_{\epsilon 3}(\tilde{\epsilon} - \widetilde{\epsilon^*})\bar{\rho}\widetilde{\epsilon^*}}{\tilde{k}} + C_{\epsilon 4}\tilde{\mu}\tau\widetilde{u_i' u_j'}\frac{\partial^2 \widetilde{u_k}}{\partial x_i \partial x_l}\frac{\partial^2 \widetilde{u_k}}{\partial x_j \partial x_l} + \frac{C_{\epsilon 5}\bar{\rho}\widetilde{\epsilon^*}}{\tau}Y_P$$

Equation 4.27

For this work, the baseline turbulence model was chosen to be the Cubic k-ε model. This model was chosen because it has been demonstrated to agree well with experimental measurements in previous works [44, 48, 49, 50, 51, 62] and because it correlated well to the current experimentally measured data as will be discussed in Section 7.1.3. It was noted in Ref. [49] that aspects of the Cubic k-ε model such as inclusion of anisotropy in the Normal Reynolds Stresses and streamline curvature effects make it suited for three-dimensional flow fields encountered in high-speed internal flow applications.

5 Computational Model

The computational model used for both the Fixed-Cowl Model and Variable-Cowl model is described in this section. First, the spatial discretization of the inlet is presented followed by the applied boundary conditions. Finally, the temporal discretization used for the transient computations is described. It should be noted that all computations were conducted based on the inlet with the long (L_c/H_{th} = 11.0) cowl and with no inlet foreplate (thin boundary layer) and with the short isolator length (L/H_{th} = 2.7). The long cowl was chosen because of the longer shock train it developed prior to the throat and the short isolator length was chosen to minimize the size of the computational mesh needed.

5.1 Spatial Discretization

To conduct the computational analysis, the inlet of Ref. [3] shown in Figure 7 was spatially discretized using a structured meshing approach. First, a series of models with the cowl fixed at select angles was created. These models will be referred to as the "Fixed-Cowl Models" and were created using a single grid at each of the selected cowl angles as would be done for a traditional, quasi-steady analysis of the inlet. After creating the Fixed-Cowl Models, an overset meshing technique was used to create a "Variable-Cowl Model". This model constitutes the primary focus of the current work and allows for the inclusion of relative motion of the cowl during the transient computations. Structured meshes with hexahedral cells were used because of their ability to capture the gradients due to shock waves well, as noted by Candler et. al [63]. Details of each type of grid will be discussed in the following sections.

5.1.1 Fixed-Cowl Models

Fixed-cowl models were created at three distinct cowl angles, θ_c = 8 deg, 1.2 deg, and 0 deg (β = 3 deg, 9.8 deg, 11 deg). A typical computational domain is shown in Figure 9. The inflow is placed 0.5 inches ahead of the compression ramp. Ahead of the compression ramp and along the sides of the ramp are boundaries used to guide the flow into the inlet such that no spillage occurred. The inlet sidewalls begin at x/H_{th} = 11.8. The leading edges of the sidewalls are accurately modeled to the 0.005-inch radius that was incorporated on the test geometry. The cowl lower surface is fully modeled; however, the upper surface is truncated. This was because the current area of focus was the flow through the inlet. The cowl extends the

full width of the inlet and joins with the sidewalls. This is in contrast to the experimental geometry which had a 0.001-inch gap between the cowl and sidewall. This will be discussed in more detail later.

The grids used were created in the commercial meshing tool Gridgen™. Grid convergence will be discussed in Section 6. The mesh was fully structured with clustering at the leading edges and no-slip walls to resolve the large gradients due to the shocks and the growth of the boundary layer. Details of the grid are shown in Figure 10. The first cell height above the no-slip walls was set to $3\text{x}10^{-5}$ inches to achieve a $y^+ < 1$ along ramp. The y^+ is a non-dimensional height defined as $y^+ \equiv \rho_w y u_* / \mu_w$, where $u_* \equiv \sqrt{\tau_w/\rho}$ is the friction velocity [16]. The cell spacing grew from this first cell height using a hyperbolic tangent function. The 8 deg cowl grid was created using 13 structured blocks with a total of 8,878,023 cells. The 1.2 deg and 0 deg cowl grids were created using 12 structured blocks with a total of 8,560,223 cells. The three Fixed-Cowl Model grids are shown together in Figure 11 and again in Figure 12 where the details of the inlet and cowl are enlarged.

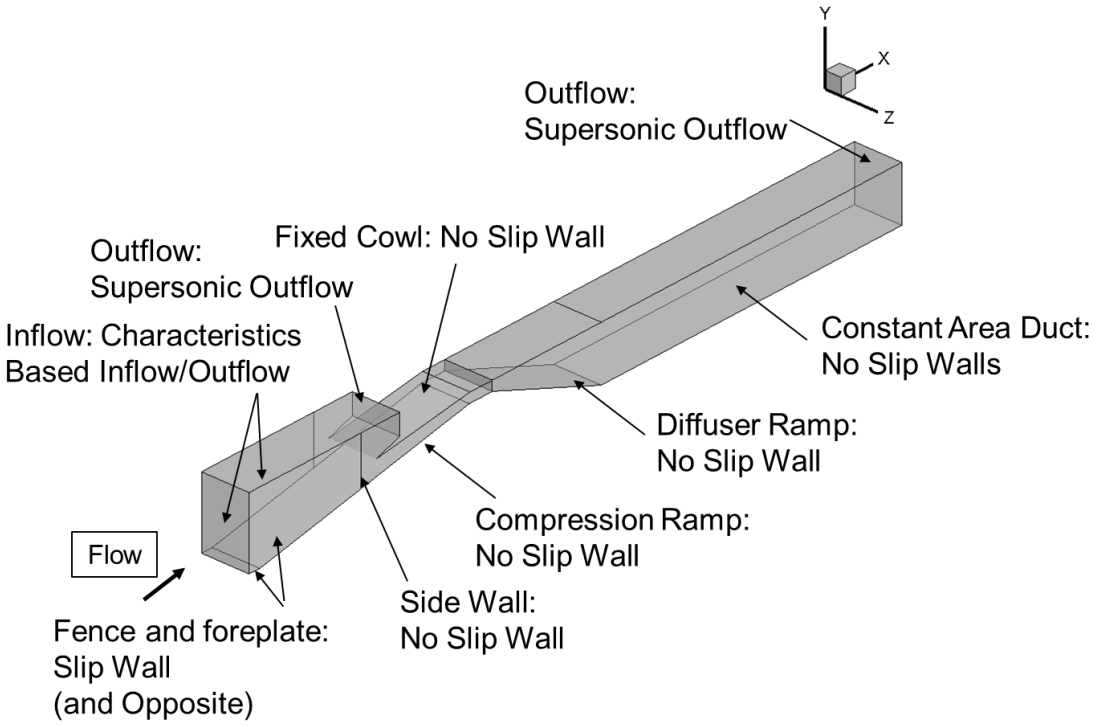

Figure 9: Computational Domain for the Fixed-Cowl Model

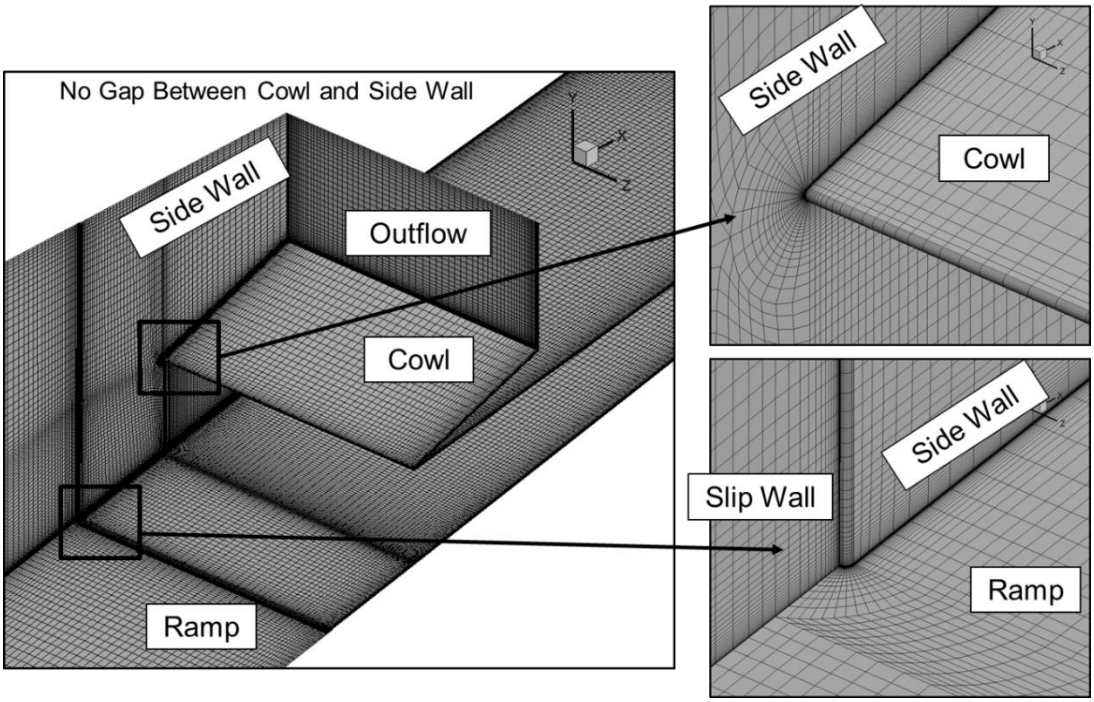

Figure 10: Structured Mesh for the Fixed-Cowl Model, 8 deg Cowl Angle Shown

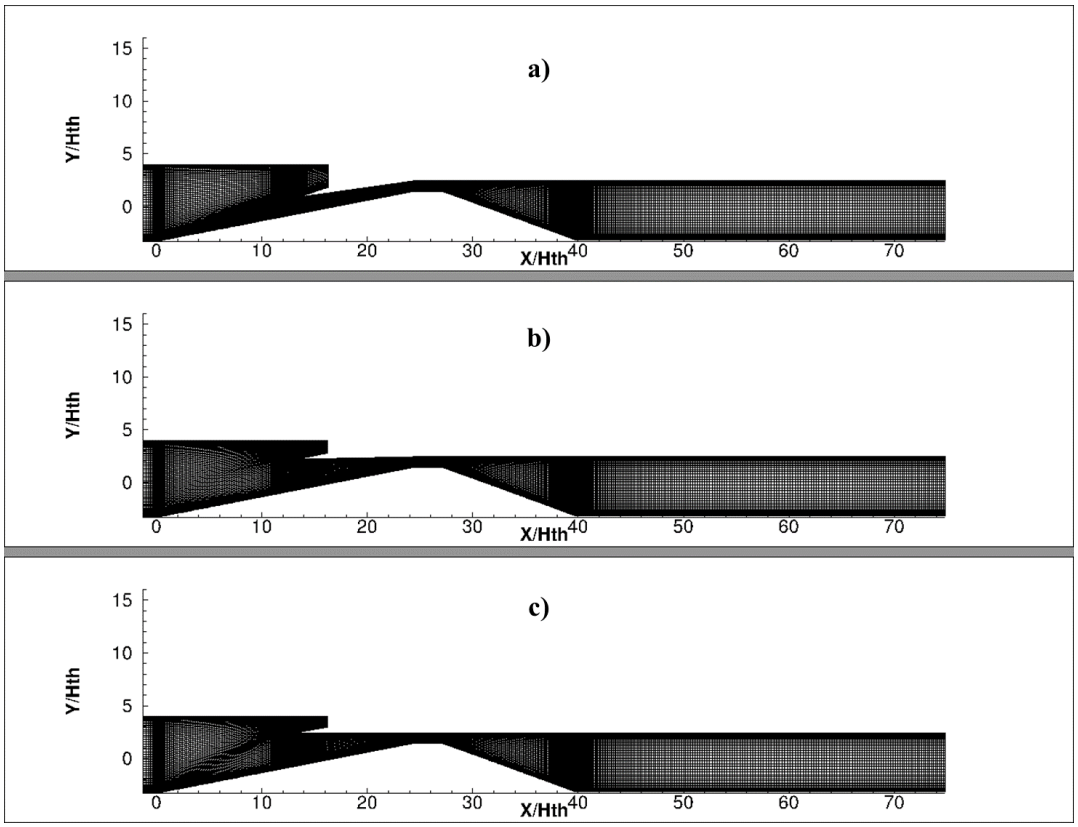

Figure 11: Fixed-Cowl Model Grids at a) $\theta_c = 8$ deg, b) 1.2 deg, and c) 0 deg ($\beta = 3$ deg, 9.8 deg, 11 deg)

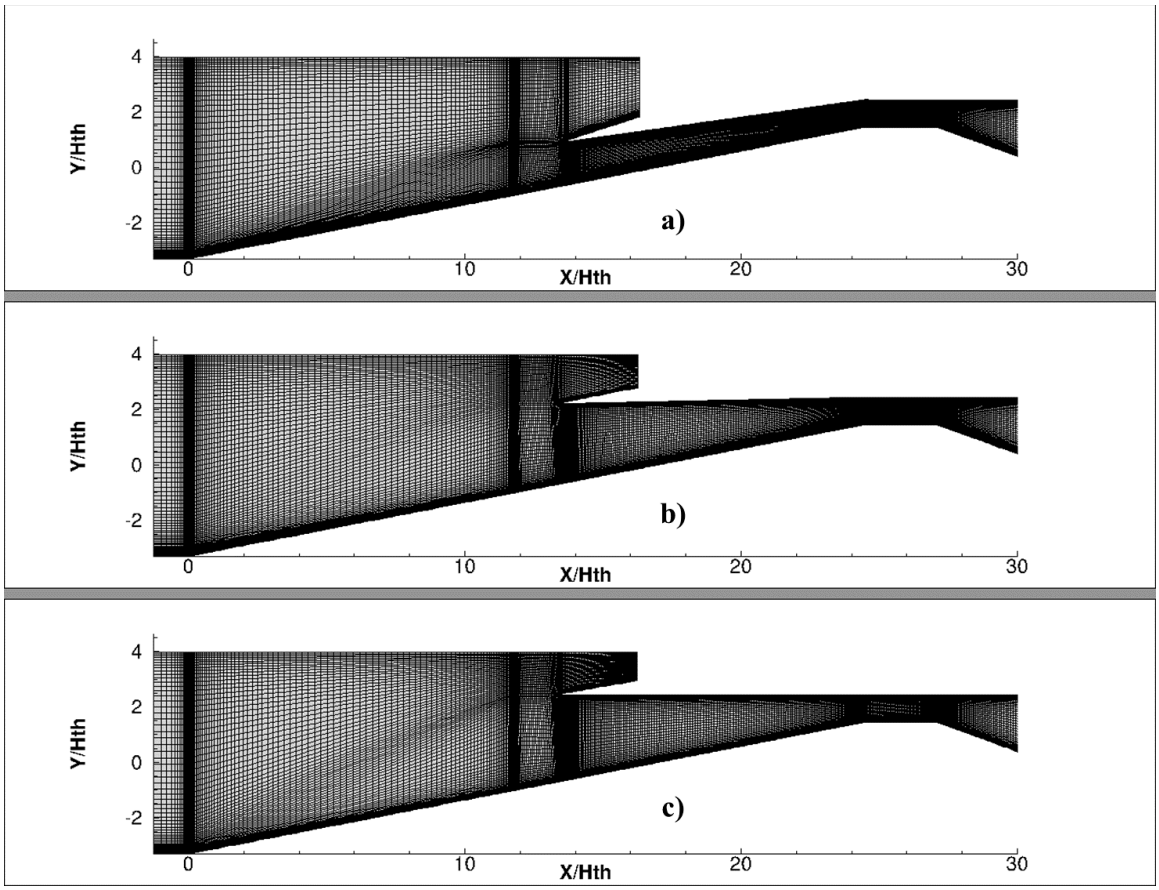

Figure 12: Fixed-Cowl Model Grids at a) $\theta_c = 8$ deg, b) 1.2 deg, and c) 0 deg ($\beta = 3$ deg, 9.8 deg, 11 deg) Enlarged to Show Inlet Ramp and Cowl Details

5.1.2 Variable-Cowl Model

After creating the Fixed-Cowl Models, a Variable-Cowl Model was created. The computational domain for this model is shown in Figure 13. The model is very similar to the Fixed-Cowl Model. However, in this case, the full cowl is incorporated, both the upper and lower surfaces. In addition, surrounding the cowl is a flow-through boundary to allow for communication between the two grids as will be discussed in the following description. Details of the leading edges are captured as was in the Fixed-Cowl Models. Unlike the Fixed-Cowl Models, the 0.001-inch gap between the cowl and sidewalls is accurately modeled.

The goal of the variable cowl grid was to allow for rotational motion of the cowl relative to the body-side portion of the inlet. To do this, the cowl and body-side portions of the inlet were meshed separately to create two distinct grids. Similar to the Fixed-Cowl Models, a structured meshing approach was applied to

both the cowl and the body-side grids. The distinct grids created for the body-side portion of inlet and the cowl are shown in Figure 14. The body-side grid was created with 12 structured blocks and a total of 10,534,944 cells. The cowl grid was created using 37 structured blocks and a total of 1,883,373 cells. This yields a total of 12,418,317 cells prior to the cutting and blanking process to be described next.

Once the two separate grids were created, they are combined using the overset meshing capability in CFD++. To do this, the two meshes are first concatenated so that the body-side grid and cowl grid overlap each other. At this point, cells from the body-side grid lay inside of the interior of the cowl, and cells from the cowl grid lay inside the interior of the body-side portion of the inlet. Therefore, sequential cutting and blanking was used to remove the cells from the interiors of the two bodies. In the sequential cutting and blanking process, the boundaries of the two grids are marked as either live of cut boundaries. The marking of live cells propagates from the live boundaries until a cut boundary is encountered which terminates the marching process. Any cell not tagged as live will be blanked and not included in the computation. In doing this process, the cells in the interiors of the two bodies are removed. An overlap region exists which allows for interpolation of flow variables between the two grids. This is created by a flow-through boundary that surrounds the cowl. An example of the overset grids prior to and after the sequential cutting and blanking process is shown in Figure 16. Additional details on the cutting and blanking process in CFD++ can be found in Ref. [60].

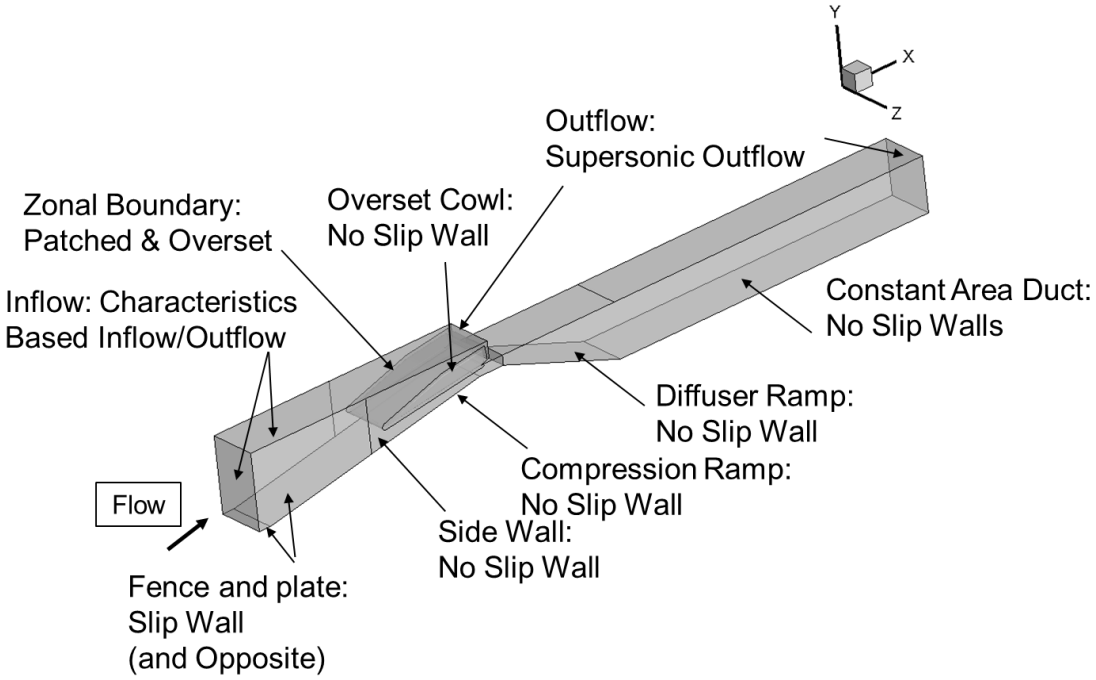

Figure 13: Computational Domain for the Variable-Cowl Model

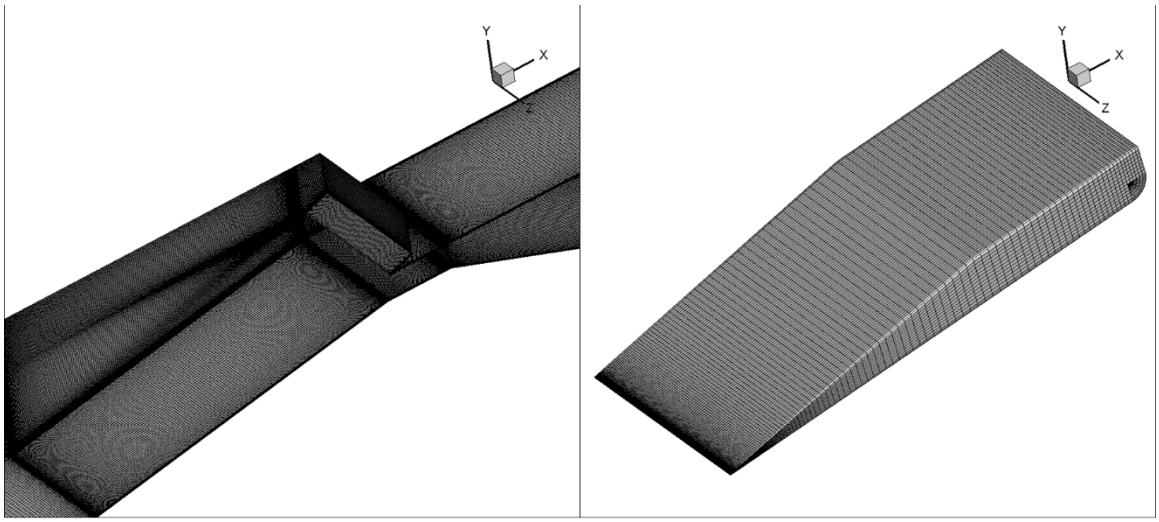

a) b)

Figure 14: Distinct a) Body-Side and b) Cowl Grids used for the Variable Geometry Model

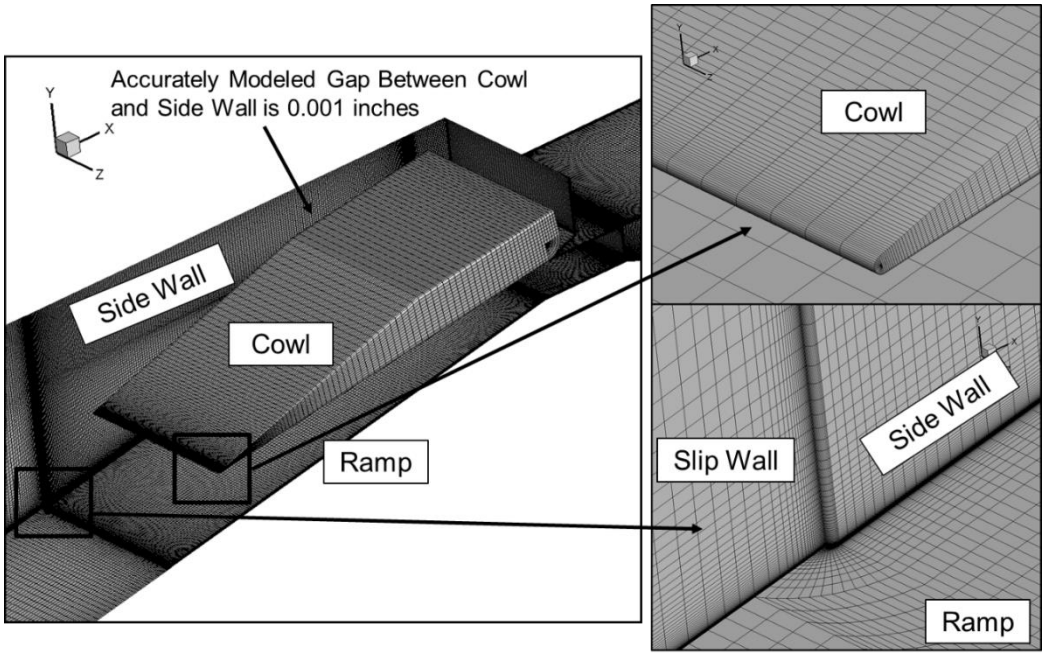

Figure 15: Overset, Structured Mesh for the Variable-Cowl Model, 8 deg Cowl Angle Shown

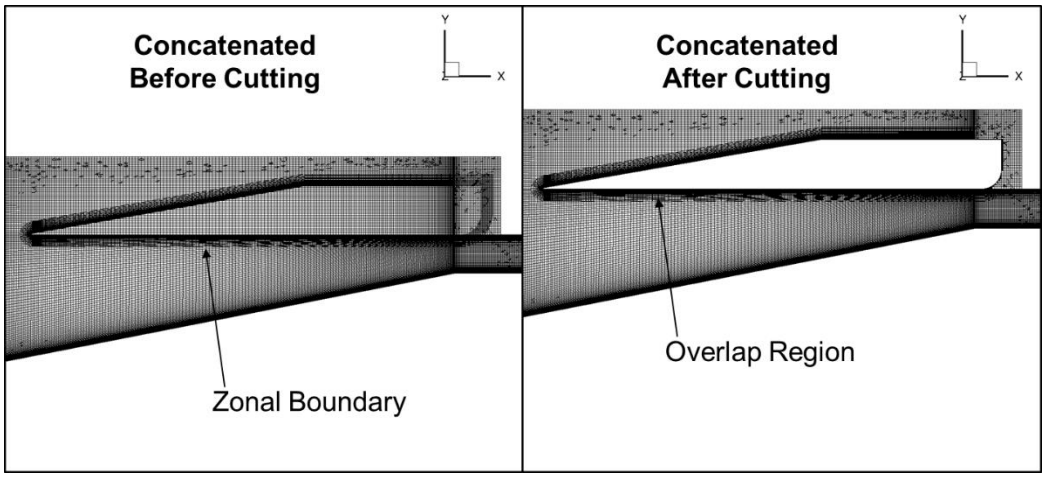

Figure 16: Cowl Grid Overset on Body Grid Before and After Sequential Cutting and Blanking is Applied

5.2 Boundary Conditions

The discretized Navier-Stokes equations are solved on the computational grids discussed in the previous section subject to the applied boundary conditions. The inflow boundaries were set to Characteristics-Based Inflow/Outflow boundary conditions where the freestream temperature, pressure and velocity are specified. The sides of the computational domain ahead of the inlet sidewalls were modeled as Inviscid Wall boundary conditions to ensure no spillage occurred and to guide the flow into the inlet. All walls of the

inlet and the cowl were set to Viscous, Adiabatic Wall boundary conditions. The outflow plane at the end of the constant area duct and at the end of the domain at the upper surface of the inlet (for the fixed-cowl model) were set to Supersonic Outflow boundary conditions. It should be noted that by applying a supersonic outflow at the end of the constant area duct, the effect of backpressure was neglected. This was done to isolate the effects of the inlet. The variable geometry model also required the use of a Patched, Zonal boundary condition to create the overlap region to allow for flow variables to be communicated between the two grids, as was previously described.

5.3 Temporal Discretization

For the transient, variable-cowl model, the governing equations were solved in a time-accurate manner with a specified time-step. An implicit, dual-time stepping approach was used wherein at each timestep, a specified number of iterations is conducted to converge the flow solution prior to moving to the next time step. The baseline time-step was 10 μs. This time-step was chosen in an attempt to balance needs based on the physics that were to be captured as well as needs based on computational limits. A time-step convergence study was conducted to assess the impact of time-step size on the solution. This study, which will be discussed in Section 6.2, considered time-steps of 100 μs and 1 μs.

5.4 Flow Conditions

All computations were conducted using the nominal wind tunnel conditions described in Table 1. It should be noted that no backpressure was applied in the computation model so as to isolate the effects of the inlet cowl on the unstart. This is consistent with the experimental data used for comparison, as it was obtained with the throttling device fully open for minimum backpressure, again to characterize the effects of the cowl on the unstart.

Table 1: Nominal Test Conditions used for Computations from Ref. [3]

Variable	Nominal Value
Static Pressure	182.2562 psf
Static Temperature	124.76 R
Mach Number	4.03
Velocity	2206.6131 ft/s

6 Computational Verification and Validation

Prior to reporting the main results of this work, it is necessary to validate the computational model and verify it is performing as intended. Therefore, this section presents an assessment of uncertainty and error quantification using established verification and validation techniques developed for computational studies to assess discretization error, temporal error, and iterative error. It should be noted that because the focus of the current work is to develop the Variable-Cowl Model, the verification and validation conducted was only done for the Variable-Cowl Model and not for the Fixed-Cowl Model. This section will address one of the main goals of the work cited in Section 1.3, that is, to validate and verify the variable-geometry model and to quantify uncertainties in the approach.

6.1 Spatial Discretization Error Assessment

To assess the spatial discretization error, a grid convergence study was conducted. A coarse grid and a fine grid were created to be compared with the baseline grid used to obtain the main results. The grids were developed such that each grid had essentially twice as many grid points in each direction. The number of cells in each grid is shown below in Table 2. Also shown is the effective refinement ratio, defined as the cube-root of the ratio of the number of cells of the current grid to previous grid as shown in Equation 6.1.

$$r_{ij} = \left(\frac{N_i}{N_j}\right)^{\frac{1}{3}} \qquad \text{Equation 6.1}$$

Table 2: Grid Characteristics used to Assess Spatial Discretization Error

Grid	Number of Cells	Refinement Ratio
Coarse (Grid 3)	1,450,113	---
Medium (Grid 2)	12,418,317	r_{23}= 2.05
Fine (Grid 1)	142,978,764	r_{12}= 2.25

The mass flow rates computed using each grid are shown if Table 3. Using the solutions on each grid, the observed order of accuracy of the computations can be determined [41]. Because of the complex nature of the grid, the refinement factors from one grid to the next were not exactly the same. Therefore, the

observed order of accuracy, p, is computed using Equation 6.2 [41, 64], where f_1, f_2, and f_3 correspond to the mass flow rate on the fine, medium, and coarse grids, respectively.

$$\frac{f_3-f_2}{r_{23}^p-1} = r_{12}^p\left(\frac{f_2-f_1}{r_{12}^p-1}\right) \quad \text{Equation 6.2}$$

Using the equation above, the observed order of accuracy is found to be $p = 0.996$. The order of accuracy is nearly first order despite the fact that the formal order of accuracy of the computations is second order. This is because of singularities that exist in the grid and due to the discontinuities in the problem, including shock waves. Using the observed order of accuracy just computed, the exact solution can be calculated using the Richardson Extrapolation [41]. The exact solution is calculated according to Equation 6.3. Doing this yields an exact mass flow rate of 0.952077 lbm/s.

$$f_{exact} = f_1 + \frac{f_1-f_2}{r^p-1} \quad \text{Equation 6.3}$$

The same results are recast as a percent difference from the exact solution by creating the Relative Discretization Error (RDE) as defined in Equation 6.4. As the grid is refined, the error is decreased as the solution approaches the exact solution.

$$RDE_i = \frac{f_i-f_{exact}}{f_{exact}} * 100 \quad \text{Equation 6.4}$$

Table 3: Mass Flow Rate Through the Inlet for Each Grid

Grid	Mass Flow Rate (lbm/s)	RDE (%)
Coarse (Grid 3)	0.939609	-1.31
Medium (Grid 2)	0.945980	-0.64
Fine (Grid 1)	0.949358	-0.29
Exact (Richardson)	0.952077	---

In addition to the Relative Discretization Error, the Grid Convergence Index (GCI) of Roache (Ref. [64]) was computed. First, the relative errors, ε_{12} and ε_{23}, are calculated as shown in Equations 6.5 and 6.6. Then, the Grid Convergence Indices are computed using Equations 6.7 and 6.8. In these equations, the factor of safety, FS, was chosen to be 3 as recommended by Roache since the observed order of accuracy

did not match the formal order of accuracy [64]. For the exact solution calculated from the Richardson Extrapolation to be valid, the grids need to be in the asymptotic range; that is, that the Taylor Series Expansion used to obtain the Richardson Extrapolation is valid in the asymptotic limit [64]. To judge whether the grids have reached the asymptotic range, the condition shown in Equation 6.9 is used [64]. The summary of the Grid Convergence Indices just discussed are presented in Table 4. As noted in Ref. [64] and Ref. [41], the Relative Discretization Error presented in Table 3 is generally not conservative compared to the Grid Convergence Index. This is visible in comparing the results of the two methods. In particular, for the coarse grid, the RDE is 1.31 % compared to the GCI of 1.9 %. Similarly, for the fine grid, the RDE is 0.29 % compared to the GCI of 0.86 %. Finally, the last row of Table 4 indicates that the grids are within the asymptotic range.

$$\varepsilon_{12} = \frac{f_2 - f_1}{f_1} \quad \text{Equation 6.5}$$

$$\varepsilon_{23} = \frac{f_3 - f_2}{f_2} \quad \text{Equation 6.6}$$

$$GCI_{12} = F_s \frac{|\varepsilon_{12}|}{r^p - 1} \quad \text{Equation 6.7}$$

$$GCI_{23} = F_s \frac{|\varepsilon_{23}|}{r^p - 1} \quad \text{Equation 6.8}$$

$$GCI_{23} = r_{12}^p GCI_{12} \quad \text{Equation 6.9}$$

Table 4: Summary of the Grid Convergence Indices for the Spatial Discretization Error Estimate

Grid	**GCI (%)**
Coarse, GCI_{23}	1.93
Fine, GCI_{12}	0.86
$r_{12}^p GCI_{12}$	1.94

The same technique was applied to the centerline pressures along the inlet. Figure 17 shows a comparison of the normalized pressures along the centerline of the duct computed using the coarse, medium, and fine grids with the exact solution computed from the Richardson Extrapolation. The Relative Discretization

Error is also shown in Figure 18. As can be seen, as the grid is refined, the relative discretization error is reduced. The largest errors for all grid levels occur at the point of the shock-boundary layer interaction as expected due to the complex interactions in this region. It should be noted that the fine grid yields results within about 15% of the exact solution at all points and the baseline grid is mostly within 20% of the exact solution.

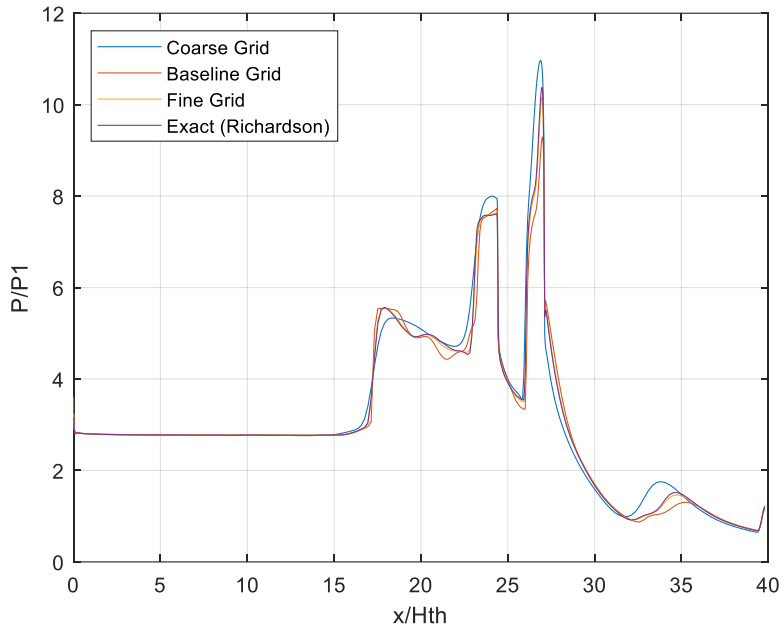

Figure 17: Centerline Normalized Pressures from the Coarse, Medium, and Fine Grids Compared with the Exact Value from Richardson Extrapolation

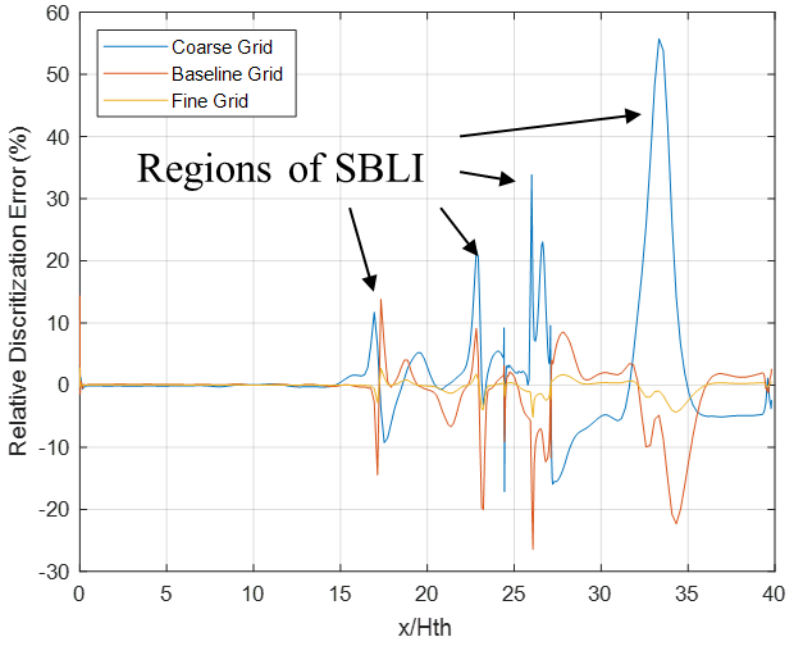

Figure 18: Relative Discretization Error for the Centerline Normalized Pressures for the Coarse, Medium, and Fine Grids

6.2 Temporal Error Assessment

To assess the convergence of the computations in time, a time step convergence study was conducted, similar to the grid convergence study conducted to assess spatial convergence. A coarse and fine time step were used in addition to the baseline time step. The coarse time step was chosen to be 100 µs and the fine time step was chosen to be 1 µs. The baseline time step as previously mentioned was 10 µs. This yielded a uniform refinement factor of 10.0. Similar to what was done in the spatial discretization error assessment, the observed order of accuracy was computed but now in time. To do this, the time-averaged mass flow rate through the inlet from 0 to 65 ms was used. The 65 ms mark was chosen merely because the finest time step only ran about 67 ms because of the significant run time required to compute the solution. The results are tabulated in Table 5. As the time step is refined, the time-averaged mass flow rate is reduced. Using these values, the observed order of accuracy for a uniform refinement factor is computed as shown below in Equation 6.10 [41, 64]. This led to an observed order of accuracy of 1.35. The dual-time stepping is a second-order accurate scheme, but due to singularities in the computations, the observed order of accuracy is less than that.

$$p = \frac{\ln\frac{f_3 - f_2}{f_2 - f_1}}{\ln(r)}$$ Equation 6.10

Again, similar to what was done in the discretization error estimation, the Richardson Extrapolation was used to estimate the exact value. The relative discretization error of the values obtained with the three different time steps was computed and is also shown in the table.

Table 5: Time-Averaged Mass Flow Rate Through the Inlet for Each Time Step

Time Step	Time-Averaged Mass Flow Rate (lbm/s)	RDE (%)
Coarse (Δt = 1.0e-4 sec)	0.881567	11.668
Medium (Δt = 1.0e-5 sec)	0.793594	0.525
Fine (Δt = 1.0e-6 sec)	0.789638	0.024
Exact (Richardson)	0.789451	---

In addition, the Grid Convergence Index was calculated for the temporal error estimate using Equations 6.5 – 6.8, the results of which can be seen in Table 6. Again, the solutions are found to be within the asymptotic range validating the exact solution calculated using the Richardson Extrapolation.

Table 6: Summary of the Grid Convergence Indices for the Temporal Error Estimate

Grid	GCI (%)
Coarse, GCI_{23}	1.55
Fine, GCI_{12}	0.07
$r_{12}^{p} GCI_{12}$	1.57

The time-history of the mass flow rate through the inlet for the different time steps is also plotted in Figure 19. Some large differences can be noted between the different time steps. First, the coarsest time step, 100 μs, does not capture the proper unstart point but predicts the inlet to remain started for a longer time than the finer time steps. In addition, the time it takes for the inlet to unstart is extended over a much longer time than shown by the finer time steps. Next, comparing the baseline (10 μs) and fine (1 μs) time steps, it can be seen that the point of unstart agrees well between the two. During the unstarted portion, however, the finest time step shows much larger oscillations compared to the baseline time step. The large amplitude oscillations occur because of significant oscillation and motion of the separation shock ahead of the

separation bubble. This motion occurs on a time scale related to the convective velocity of pressure waves in the flow, namely $u \pm a$, where u is the flow velocity and a is the speed of sound. Using this velocity and an average cell size outside of the boundary layer of about 0.4 inches yields a time scale of $\Delta t = \frac{u+a}{\Delta x} \approx$ 1.22 μs. Therefore, the motion of the shock wave occurs at a time scale smaller than the baseline time step. The baseline time step then produces essentially a "time-averaged" solution during this period. This is shown visually in Figure 20, which compares the centerline Mach number contours computed using the bassline and fine timesteps during the time interval from 20.0 ms to 22.0 ms. The details of the flow will be discussed in depth in Section 7, but it can be seen that much larger oscillations in the separation bubble and supersonic jet along the underside of the cowl are predicted by the fine time step compared to the baseline timestep. For reference, the position of the separation shock at the 20.0 ms frame is outlined in each frame to show how the oscillations in the separation bubble lead to motion of the separation shock. It is important to note, however, that if the exact dynamics of unstart are not necessary, the baseline time step does a good job of capturing the unstart and restart points. This is significant to note because the computational cost for the finest time step is significantly greater than that for the baseline computation and makes using the finest time step unfeasible for engineering analyses. For this reason, the baseline time step was chosen to be 10 μs in this work.

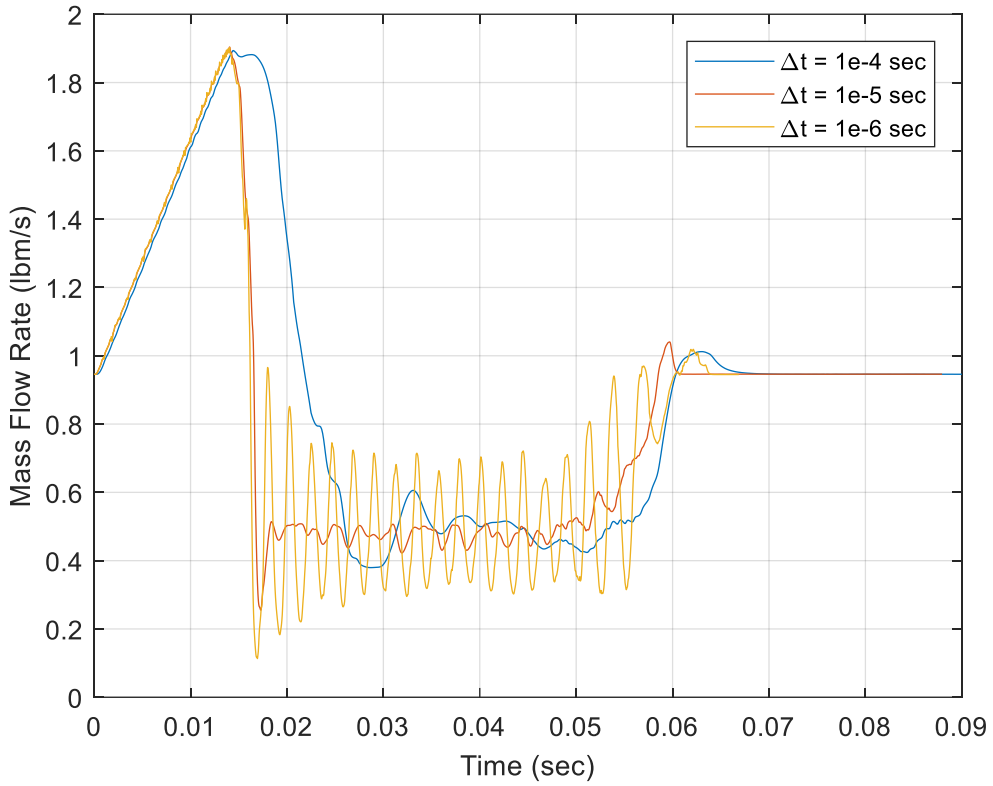

Figure 19: Time Histories of Mass Flow Rate Through the Inlet for Different Cowl Rotation Rates Obtained Using Different Time Steps

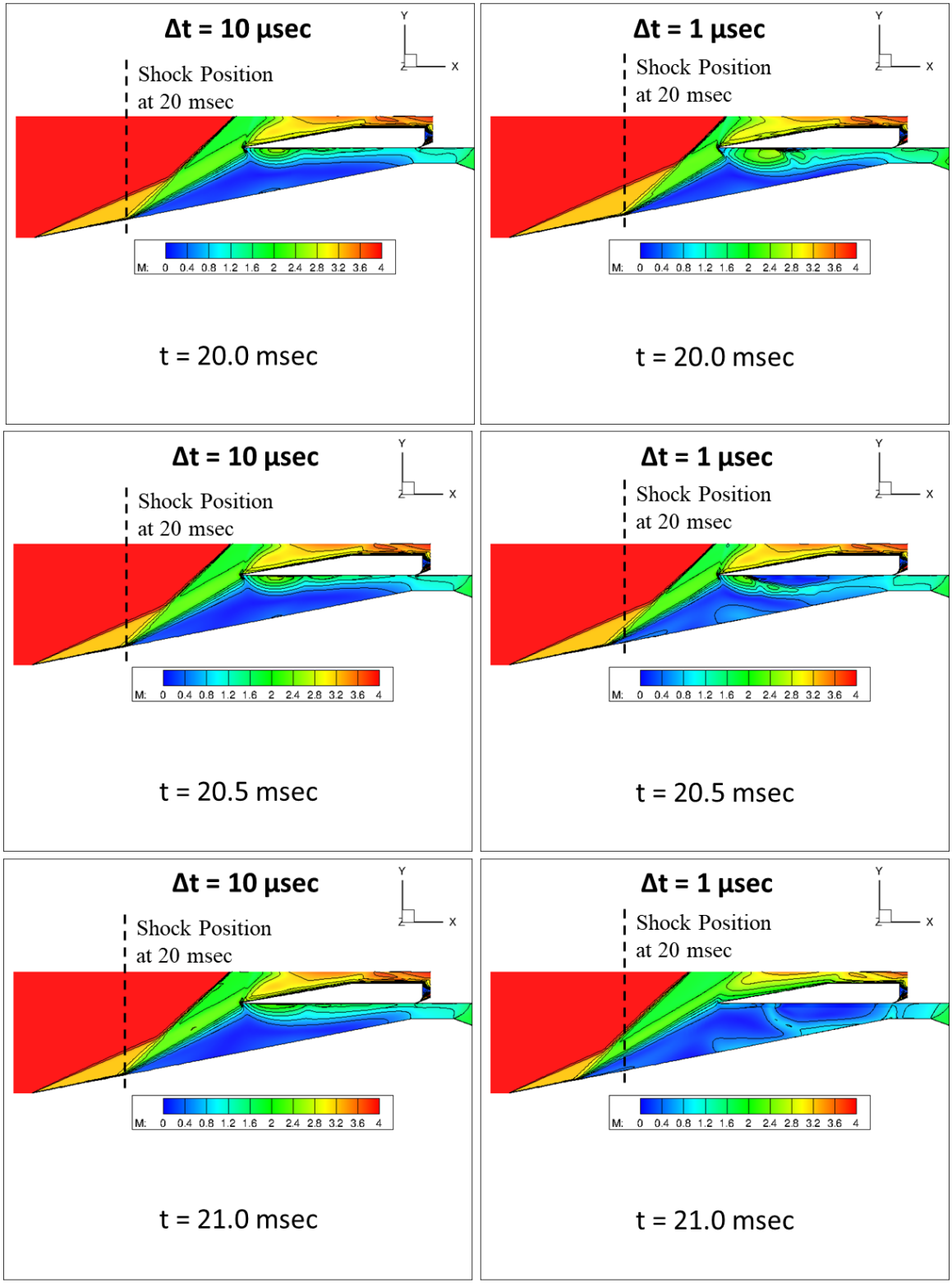

Figure 20: Centerline Mach Number Contours of the Oscillatory Unstarted Flow Field Computed with a) the Baseline and b) Fine Timesteps

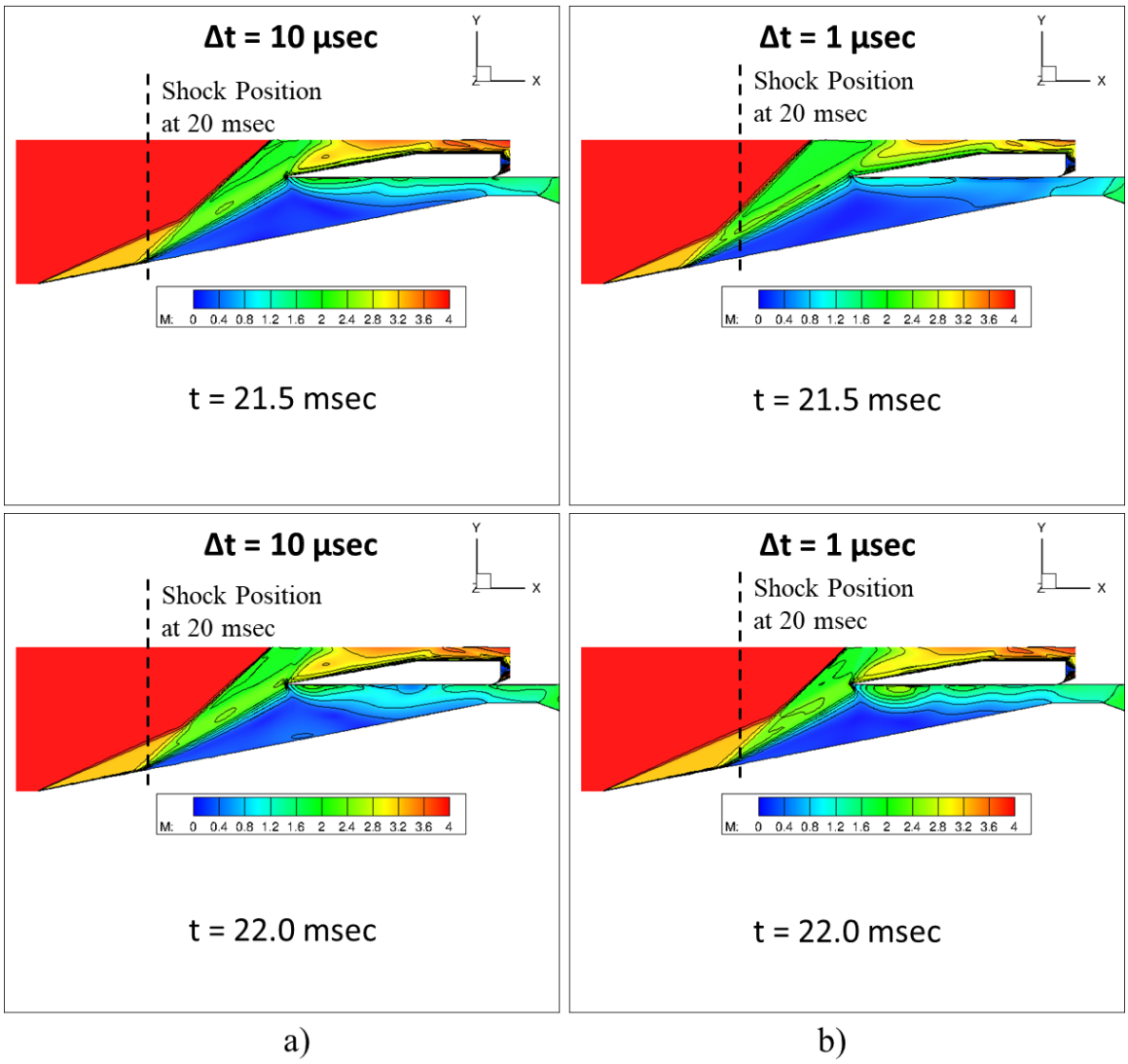

Figure 20 (Continued): Centerline Mach Number Contours of the Oscillatory Unstarted Flow Field Computed with a) the Baseline and b) Fine Timesteps

The previous results are also reformatted as a function of the cowl angle, θ_c in Figure 21. It can be seen that at the same cowl angle, the coarse time step is actually slightly underpredicting the mass flow rate through the inlet as the cowl is rotated open. Although the actual time of the unstart is later for the coarse time step, Figure 21 shows that the angle of unstart and restart agree with all of the time steps. As the cowl closes there is again a discrepancy in the mass flow rates with the smallest time step showing larger fluctuations. The peak mass flow rate and the cowl angle and time at which this peak occurs is shown in Table 7. Again, the peak mass flow rate is underpredicted by the coarse time step but good agreement between the baseline

and fine timesteps is shown. The angle of peak mass flow rate for all models occur essentially when the cowl is at the horizontal position, but the actual time at which this occurs is delayed when using the coarse timestep.

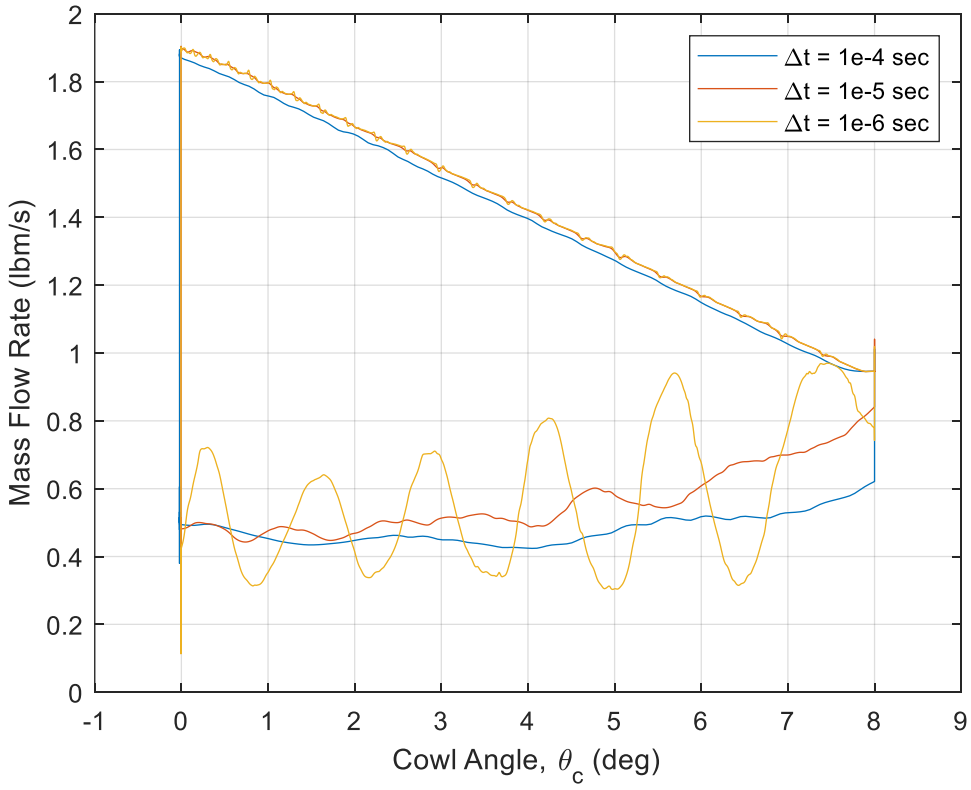

Figure 21: Mass Flow Rate Through the Inlet During the Rotation of the Cowl Plotted as a Function of Cowl Angle for Different Cowl Rotation Rates Obtained Using Different Time Steps

Table 7: Cowl Angle at Peak Mass Flow Rate and Peak Mass Flow Rate Obtained Using Different Time Steps

Time Step	Cowl Angle, θ_c, at Peak Mass Flow Rate (deg)	Time at Peak Mass Flow Rate (sec)	Peak Mass Flow Rate (lbm/s)
Coarse ($\Delta t = 100$ μs)	-0.0214	0.0144	1.8937
Medium ($\Delta t = 10$ μs)	-0.0042	0.01405	1.9040
Fine ($\Delta t = 1$ μs)	-0.0048	0.014043	1.9030

A similar study was conducted with the same time steps using the Menter SST turbulence model. This was done to understand whether the turbulence model changed the behavior of the model as the time step was refined or coarsened. As seen in Figure 22, the same trends noted above occur with the Menter SST model and no major differences were caused by the difference in turbulence model.

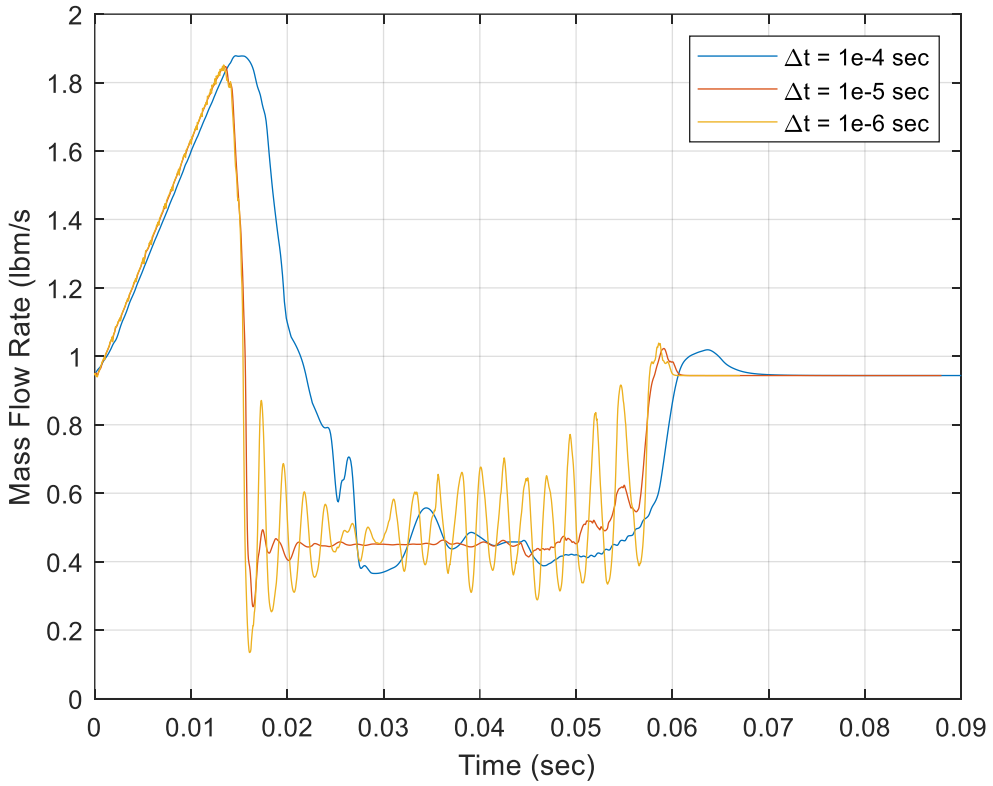

Figure 22: Time Histories of Mass Flow Rate Through the Inlet for Different Cowl Rotation Rates Obtained Using the Different Time Steps and the Menter SST Turbulence Model

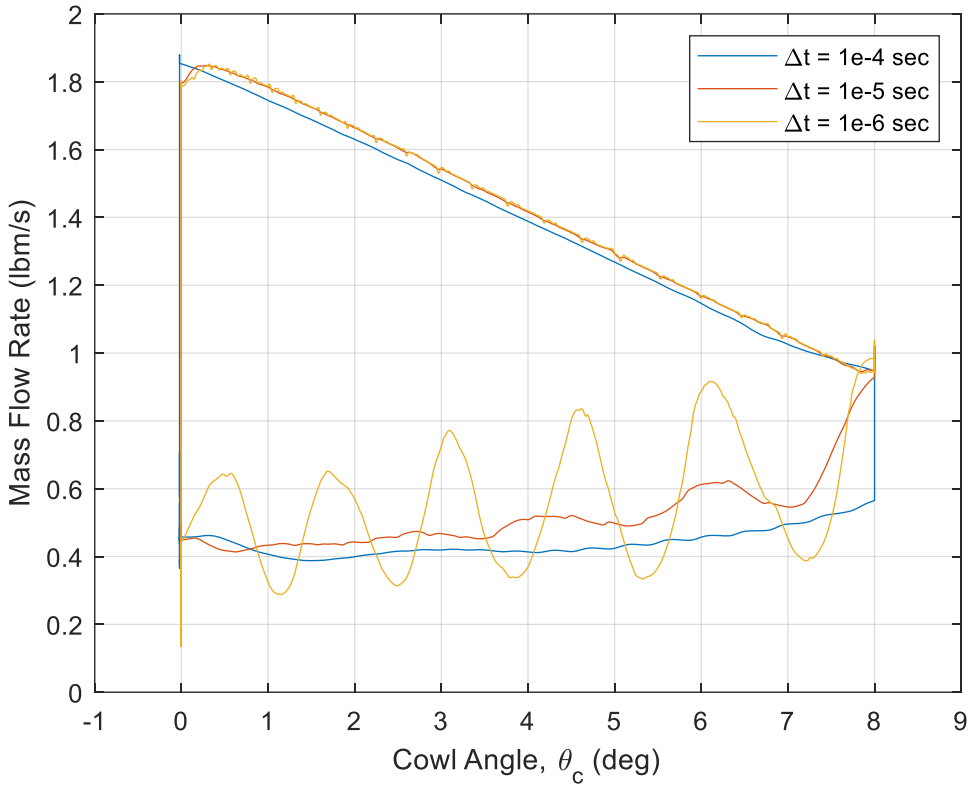

Figure 23: Mass Flow Rate Through the Inlet During the Rotation of the Cowl Plotted as a Function of Cowl Angle for Different Cowl Rotation Rates Obtained Using Different Time Steps and the Menter SST Turbulence Model

6.3 Iterative Error Assessment

The transient variable-cowl solutions were conducted using an implicit dual-time stepping approach as mentioned previously. In this approach, a series of inner iterations are conducted at each time step to converge the flow field prior to moving to the next time step. This approach generally allows for larger time steps to be used compared to a purely explicit approach [60]. In doing this, another potential source of error can be from the number of sub-iterations chosen. In this work, the number of sub-iterations was chosen to be 20. To quantify the effect of the sub-iterations on the computations, a single transient case was conducted at the nominal time step of 10 μs with 10, 20, and 30 sub-iterations. The results of this study are shown in Figure 24. In general, the agreement between all cases is good. The point of unstart is captured well with all sub-iterations. The main differences appear in the oscillatory nature of the unstarted flow

field. The restart point is also consistent between all sub-iterations. The peak mass flow rates and the angle and time at which this peak occurs also agree well with all the sub-iterations as seen in Table 8.

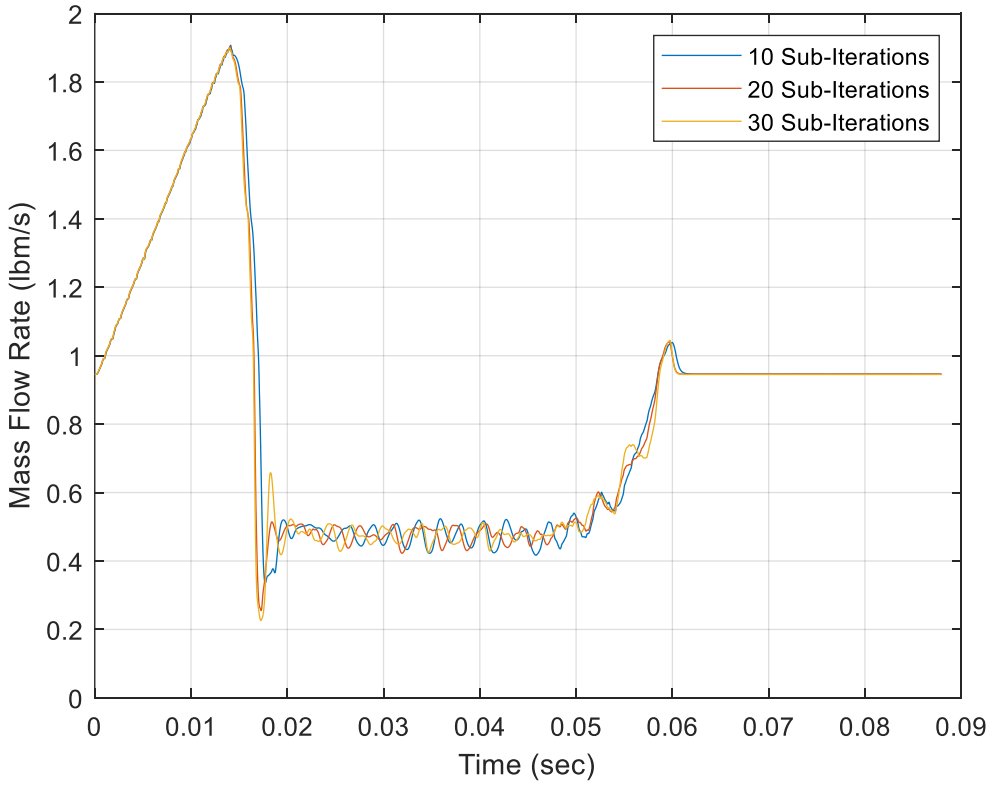

Figure 24: Comparison of the Time Histories of Mass Flow Rate for Computations with 10, 20, and 30 Sub-Iterations to Assess the Impact of Iterative Errors

Table 8: Cowl Angle at Peak Mass Flow Rate and Peak Mass Flow Rate Obtained Using Different Sub-Iterations

Number of Sub-Iterations	**Cowl Angle, θ_c, at Peak Mass Flow Rate (deg)**	**Time at Peak Mass Flow Rate (sec)**	**Peak Mass Flow Rate (lbm/s)**
10	-0.0042	0.01411	1.9072
20	-0.0042	0.01405	1.9038
30	-0.0042	0.01404	1.8993

7 Computational Results

Now that the computational approach has been validated and verified to be soundly based, the main results of the work are presented. As stated previously, the major research goals of the current work are:

1. To develop a variable-geometry model to analyze the transient features of an inlet with a rotating cowl computationally and to compare its results to traditional quasi-steady analysis approaches
2. To use the variable-geometry model to obtain insight into the physics of the transients that the inlet experiences including unstart/restart and hysteresis induced by cowl motion
3. To validate and verify the new model and to quantify uncertainties in the approach

The third goal has been addressed already in Section 6. The current section presents the results obtained first using the Fixed-Cowl Model followed by the results obtained using the Variable-Cowl Model. Both three-dimensional and two-dimensional solutions were conducted using steady-state and transient approaches. Results of the Fixed-Cowl Model will be shown first and will be used as the baseline for comparing the steady-state Variable-Cowl Model results against. By doing this, the first goal, comparing the new, transient, variable-geometry model with a traditional quasi-steady analysis will be addressed. Following this, the transient computational results will be used to accomplish the second goal of investigating the dominant physical features of the unstart, restart, and hysteresis in the variable-geometry inlet. Finally, to particularly highlight the effects of the three-dimensional phenomena, complementary two-dimensional solutions will be presented. This will accomplish the second goal stated above.

7.1 Fixed-Cowl Model Results

The first results obtained were quasi-steady results at discrete cowl angles using the Fixed-Cowl Model that was described in Section 5.1.1. These results were obtained to be used first to compare with the experimental results and to validate the computational approach; second, to assess the performance and effect of an array of turbulence models on the computed performance; and third to be used as baselines for comparisons made with the Variable-Cowl Model. Both two-dimensional and three-dimensional results were obtained at three selected cowl angles: θ_C = 8, 1.2, and 0 deg (β = 3, 9.8, 11 deg).

7.1.1 Three-Dimensional Results

Results for the first cowl angle, $\theta_c = 8$ deg, can be seen in Figure 25. The figure shows the Mach number contours along the center plane of the inlet. The ramp shock which aligns the incoming flow with the ramp and creates the external compression is clearly visible. The Mach number behind this shock is reduced from the freestream value of 4.03 to 3.23. When the cowl is set to $\theta_c = 8$ deg, the first cowl shock initiates the internal compression shock train that develops as the shock waves reflect off the ramp and the cowl surfaces. The shock train consists of four oblique shock waves ahead of the throat and isolator. As the flow passes through the shock train, the Mach number is repeatedly reduced, and the pressure and temperature are increased. In addition, compression is also achieved due to the oblique shocks emanating from the leading edges of the sidewalls as shown in Figure 26. Inside the isolator, a region of subsonic flow can be seen which is caused by separation due to shock boundary layer interaction; however, along the inlet ramp, the pressure rises due to the shocks are not strong enough to cause such separation.

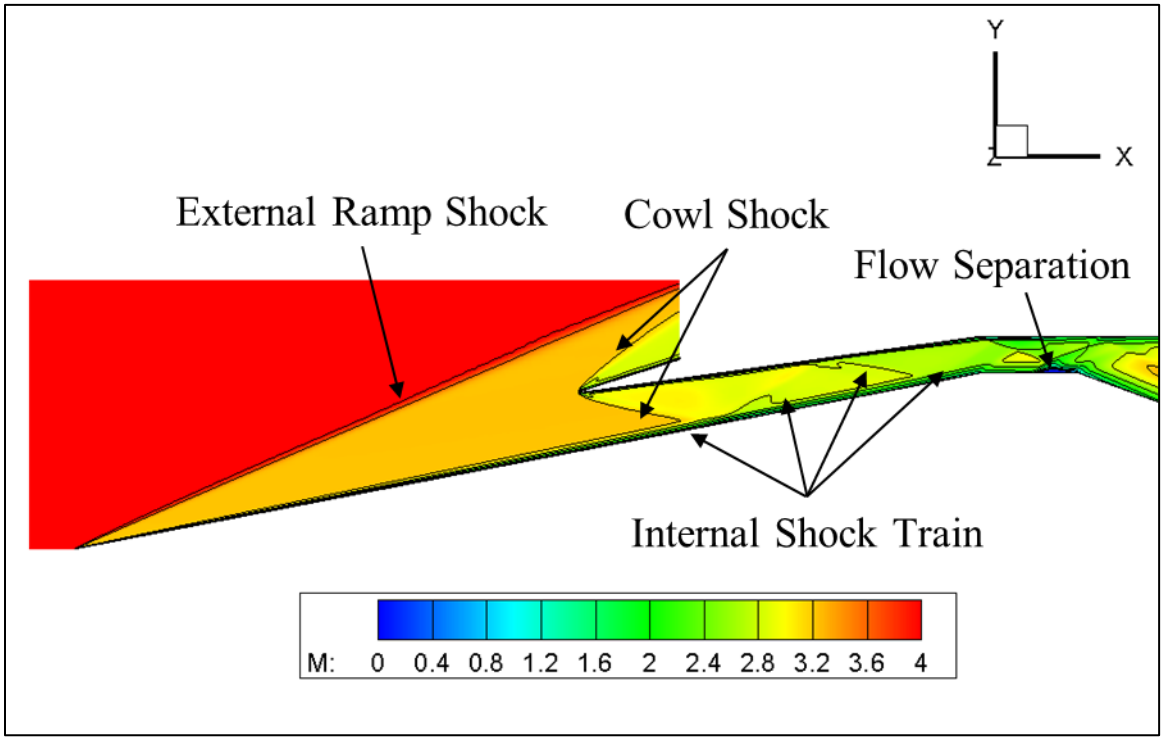

Figure 25: Centerline Mach Number Contours for the Fixed-Cowl Model at $\theta_c = 8$ deg

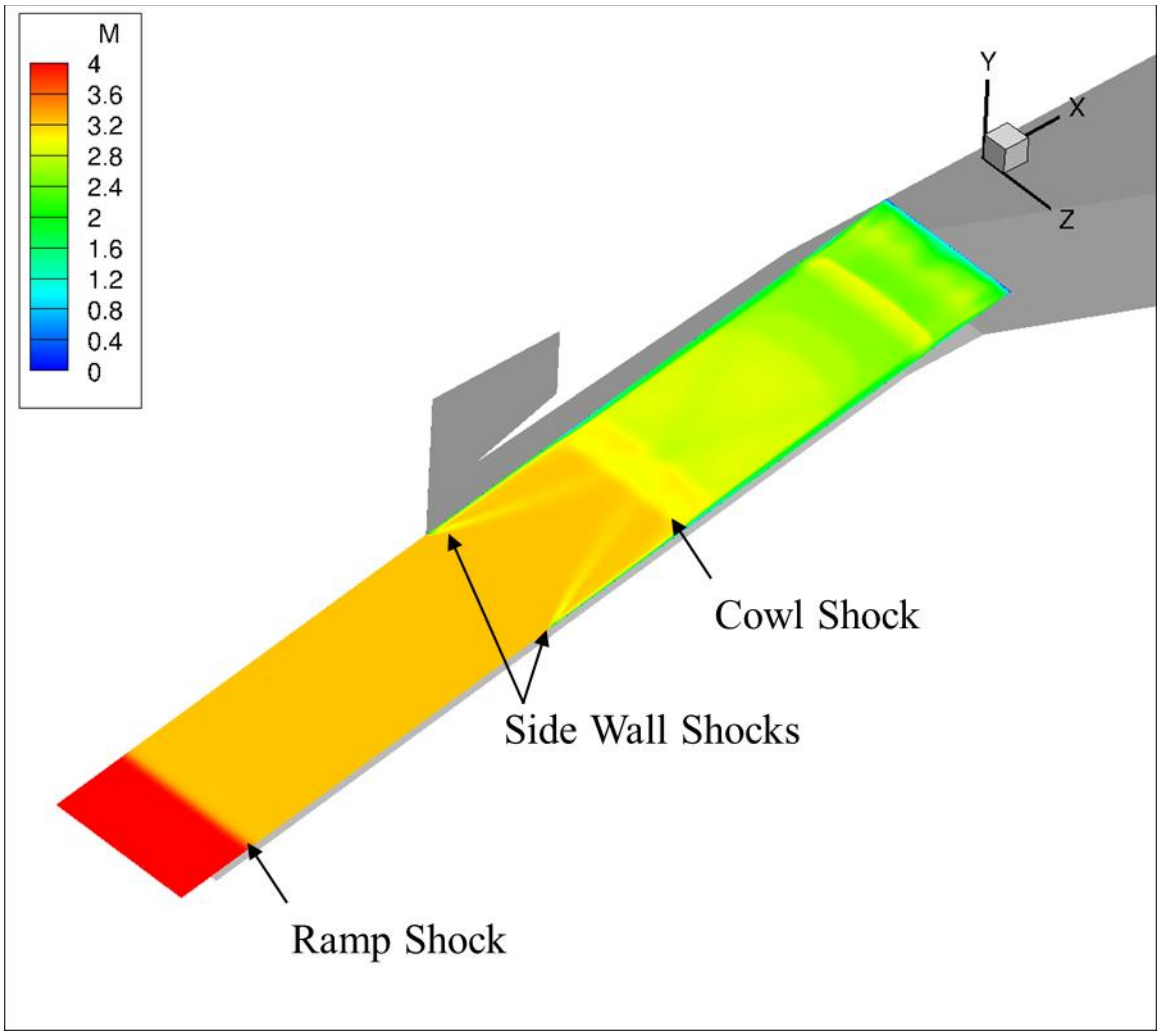

Figure 26: Mach Number Contours for the Fixed-Cowl Model at $\theta_c = 8$ deg along a Plane 0.1 inches above the Inlet Ramp

Figure 27 shows the surfaces of the inlet with contours of the logarithm of the pressure ratio and with simulated oil flow traces mapped along the surfaces. These oil flow traces indicate the separated flow regions in the isolator where the traces converge to create two foci like that described in Ref. [(1)]. The extent of the separation bubble is depicted in Figure 28 by an isosurface defined by the points where the axial velocity, U, is 0. Also visible by the oil flow traces are the complex flow patterns along the inlet sidewalls due to the cowl shock which sweeps across the surface.

It is interesting to note that along the inlet there are multiple regions of spanwise flow. The first spanwise flow is induced by the sidewall leading edge shocks and a second, smaller spanwise flow is created at the

point where the cowl shock impinges on the ramp. This leads to a three-dimensional pressure field on the ramp surface that can be seen in Figure 27. There is a "X-like" pattern in Figure 26 due to the crossing waves that lead to local regions of higher and lower pressure. At the axial station where the cowl shock impinges on the ramp, the pressure is not uniform in the spanwise direction but instead has local regions of increased pressure where the waves interact. This is shown in Figure 29 which displays the surface pressures in the spanwise direction across the inlet in the region of the cowl shock impingement on the inlet ramp. Contours of the three-dimensional spanwise flow are also shown in Figure 30. In particular, note the change in flow contours in the corners where the sidewall and ramp meet. It will be shown later that at these points the boundary layer will separate with large cowl angles ultimately leading to the inlet unstart.

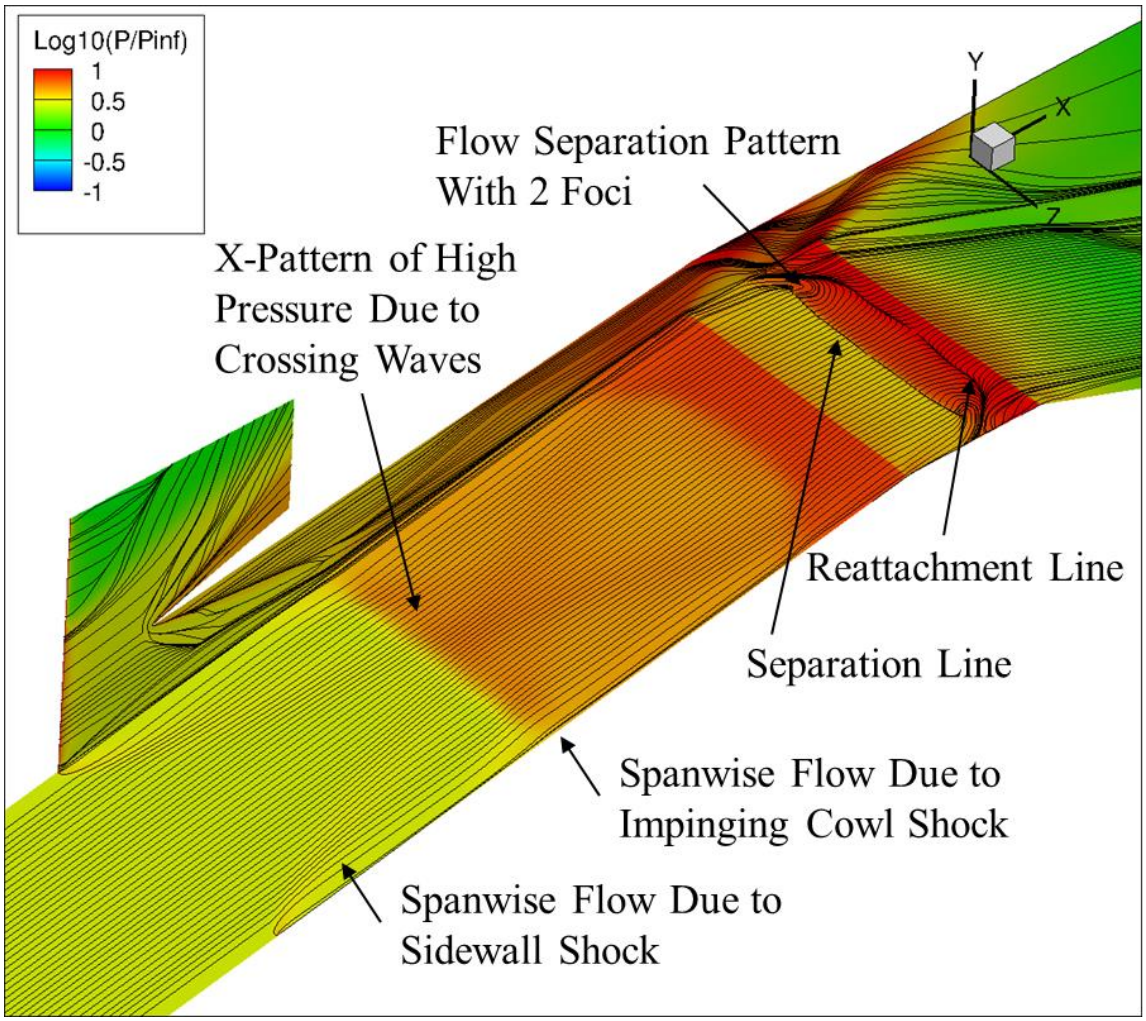

Figure 27: Simulated Oil Flow Lines and Log of the Pressure Ratio Contours along the Inlet Ramp and Sidewall for Cowl at $\theta_c = 8$ deg

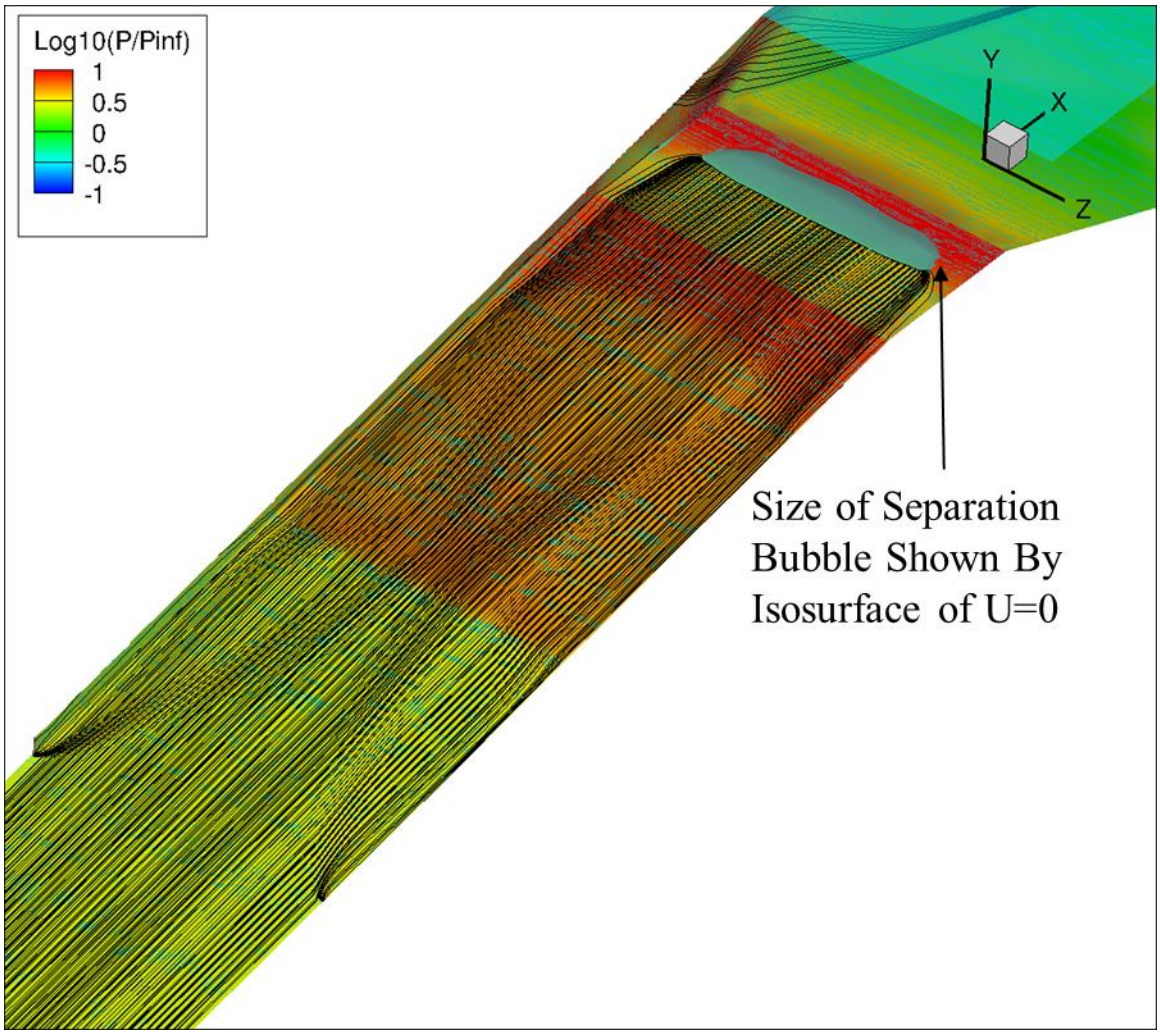

Figure 28: Simulated Oil Flow Lines and Log of the Pressure Ratio Contours along the Inlet Ramp and Sidewall for Cowl at $\theta_c = 8$ deg with Isosurface of U=0 showing Separated Flow Regions

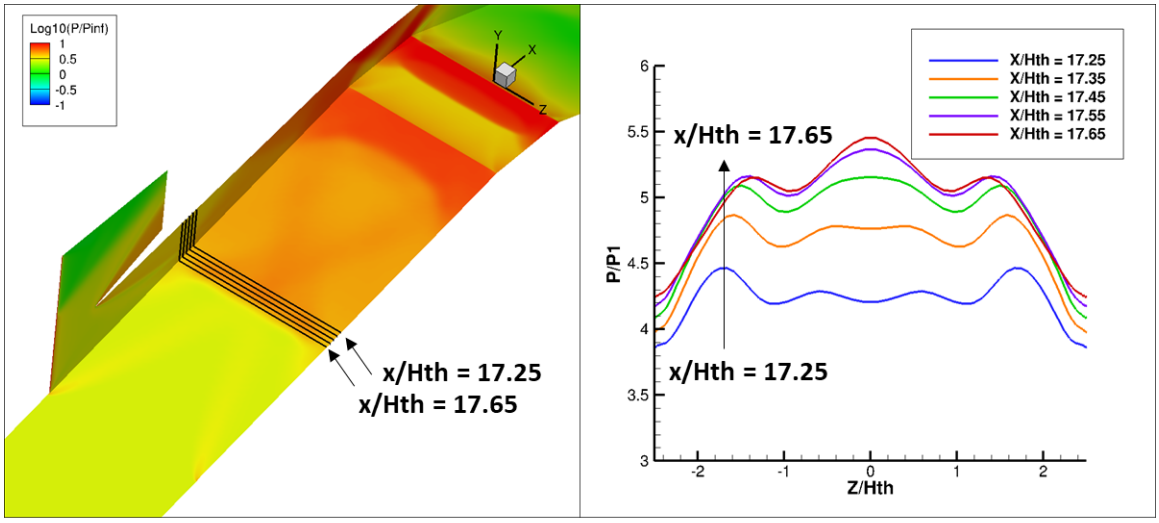

a) b)

Figure 29: a) Pressure Contours and b) Spanwise Pressures in the Region of the Cowl Shock Impingement

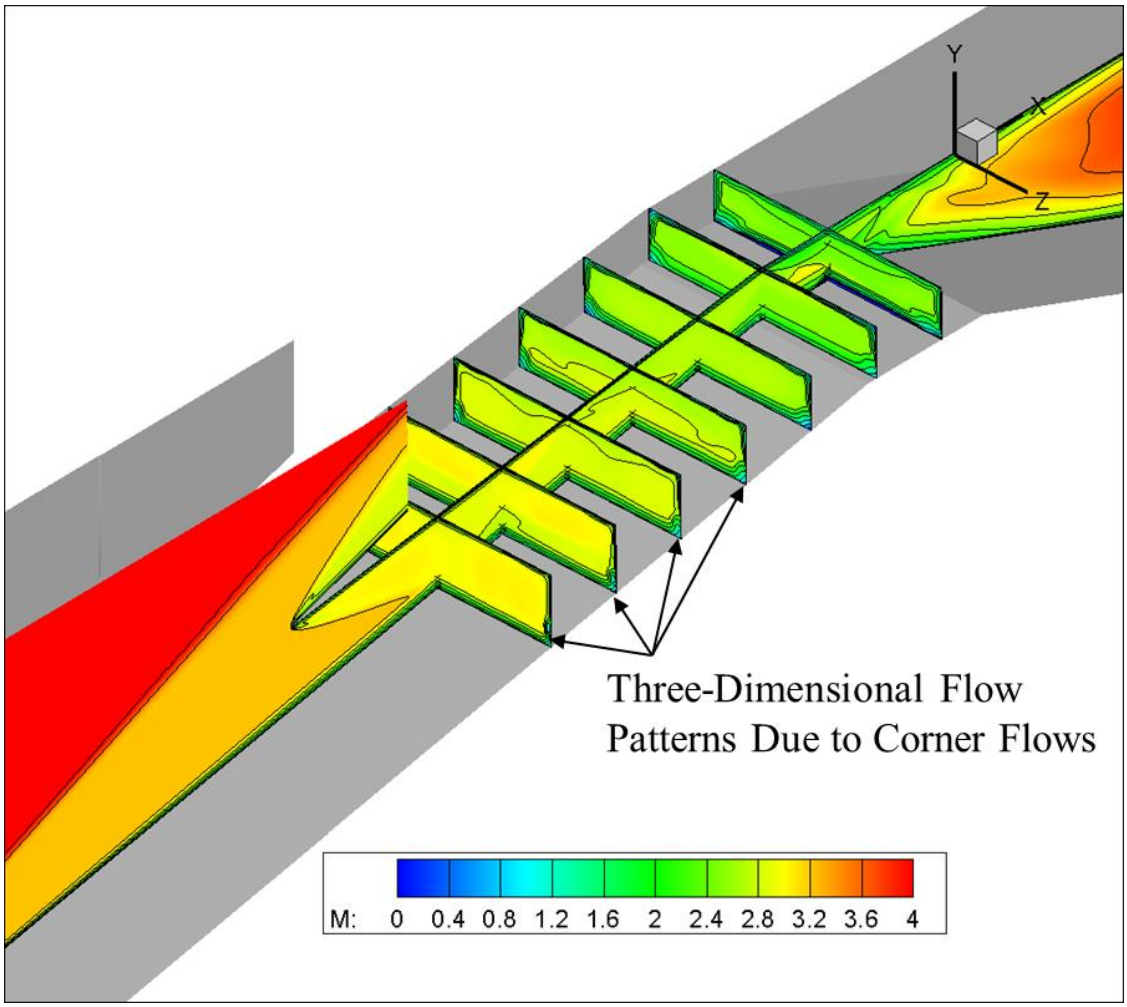

Figure 30: Spanwise and Centerline Mach Number Contours through the Inlet at $\theta_c = 8$ deg

Finally, a comparison of the centerline wall pressures computed using the Fixed-Cowl Model and the experimental data from Ref. [3] is shown in Figure 31. The main features are captured by the current computation. Along the inlet ramp prior to the shock train ($x/H_{th} = 0$ to 15), the computation predicts a slightly lower pressure than the experimental data reports. This is possibly due to slight flow angularity in the wind tunnel. The first pressure rise at $x/H_{th} = 17$ is due to the cowl shock impinging on the inlet ramp. The pressure rise due to this interaction is nearly captured. However, the model predicts a steeper expansion after the interaction compared to the experimental data. The current model then underpredicts the pressure rise at the second interaction but agrees better at the third interaction. The pressure in the computations falls off much more rapidly than the experimental data because the isolator length in the computation was shorter than that used in the experiment. The discrepancies at shock impingement points mentioned are most likely due to the inability of RANS turbulence models to model all of the physics associated with shock-boundary layer interactions. In addition, in this work, no attempt to adapt the grid to the shock waves was made. This was because in the Variable-Cowl Model, this would have had to be done at each time step which would lead to challenges in computational time. However, it is known that aligning the grid with the shock waves can have an impact on the predicted flow quantities after the shock wave. In general, the model compares well with the experimental data and captures the relevant flow features.

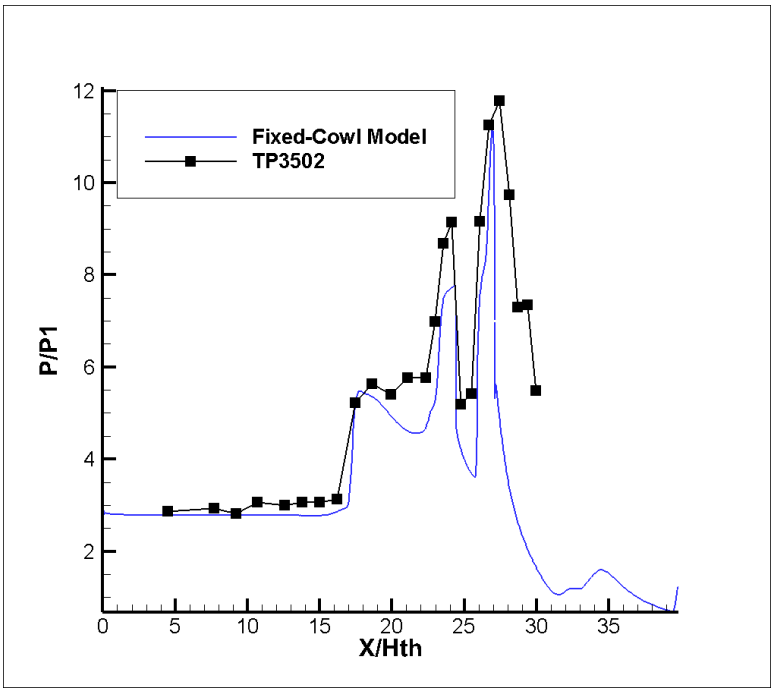

Figure 31: Comparison of the Normalized Centerline Wall Pressures from the Fixed-Cowl Model at $\theta_c = 8$ deg and the Experimental Results of Ref. [3]

At the cowl angle of $\theta_c = 1.2$ deg, the predicted flow field structure shown in Figure 32 - Figure 36 is similar to that at 8 deg. The ramp shock initiates the compression process, and the cowl forms a shock train internal to the inlet. However, now with the inlet cowl further open, the ramp shock is just above the shock-on-lip condition with the cowl. This leads to a shock-shock interaction between the ramp shock and the upper portion of the cowl shock. This shock interaction can be classified as the Type VI shock interaction based on Edney's [65, 66, 67] classification.

Also, because the cowl is closer to the horizontal position, it creates a larger turning angle for the flow after the ramp shock. Therefore, the cowl shock is much stronger and leads to a larger drop in Mach number and a larger increase in pressure compared to the 8 deg cowl position. Because of this, at the point where the cowl shock impinges on the inlet ramp, a larger adverse pressure gradient is imposed on the boundary layer which induces a small separation region that can be seen in Figure 32. At this point, because of the geometry of the reflected waves, the shock train only includes two oblique waves prior to entering the isolator. The second wave in the shock train is reflected off the underside of the cowl and impinges on the

point where the ramp transitions to the isolator and is essentially cancelled by an expansion wave. Additional regions of separated flow can be seen inside the isolator. Unlike when the cowl was set to 8 deg, there are also regions of separation along the sidewalls of the inlet as seen in Figure 33. These corner separation regions can be seen to affect the flow by creating additional blockage that pushes the flow inward leading to additional oblique waves that move in the spanwise direction toward the centerline. This leads to the highly three-dimensional flow field shown in the figure and which is further highlighted in Figure 34 which shows contours of the logarithm of the pressure ratio and simulated oil flow traces along the inlet solid surfaces. The oil flows show the central separation region as well as the sidewall separation regions and how the sidewall flow impacts the central separation region similar to what was found in Ref [21]. Again, visible by the oil flow traces are the complex flow patterns along the inlet sidewalls due to the cowl shock which sweeps across the surface. The separation in the sidewall region extends farther in front of the impinging shock due to disturbances that are propagated in the subsonic portion of the boundary layer. The separation regions are elucidated in Figure 35 where they are depicted with isosurfaces of where the axial velocity is zero ($U = 0$). This shows that the separation in the corner flows and cowl shock impingement are two distinct separation bubbles and that at the inlet shoulder, there exists three distinct separation bubbles. Figure 36 is analogous to Figure 30 showing how the corner flow regions have developed. At this cowl angle, the corner flows have grown significantly into regions of separated flow. There are also regions of corner vortices that entrain fluid from the core flow as highlighted in Figure 37.

Again, the centerline wall pressures along the inlet ramp are compared with the experimental data of Ref. [3]. As shown in Figure 38, the pressure rise at all of the shock interactions is captured quite well by the computations. The agreement seems to be slightly better than that obtained at the 8 deg cowl angle. Again, the computed pressures drop off sooner because the isolator length is shorter in the model than in the experiment.

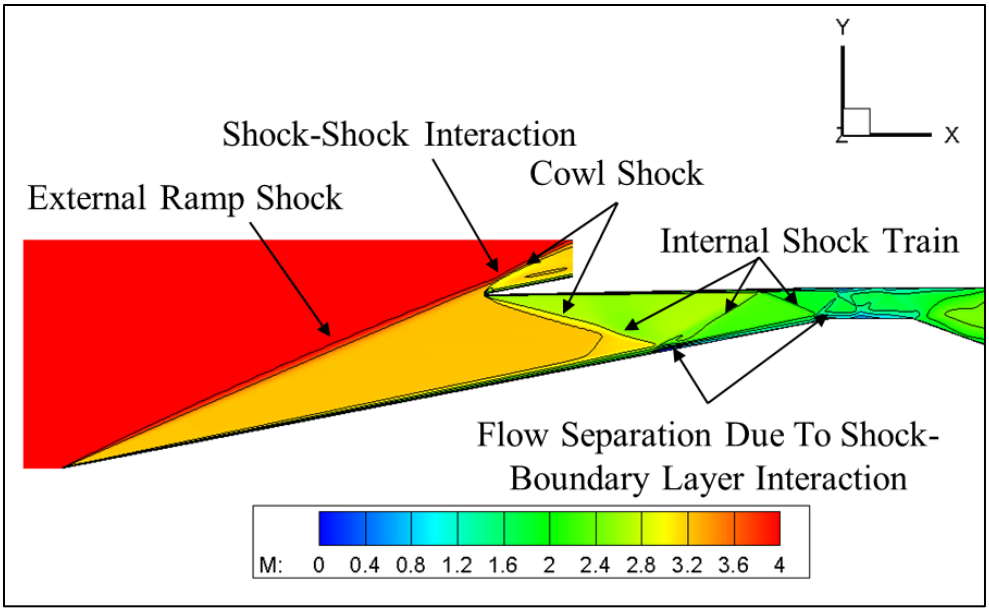

Figure 32: Centerline Mach Number Contours for the Fixed-Cowl Model at $\theta_c = 1.2$ deg

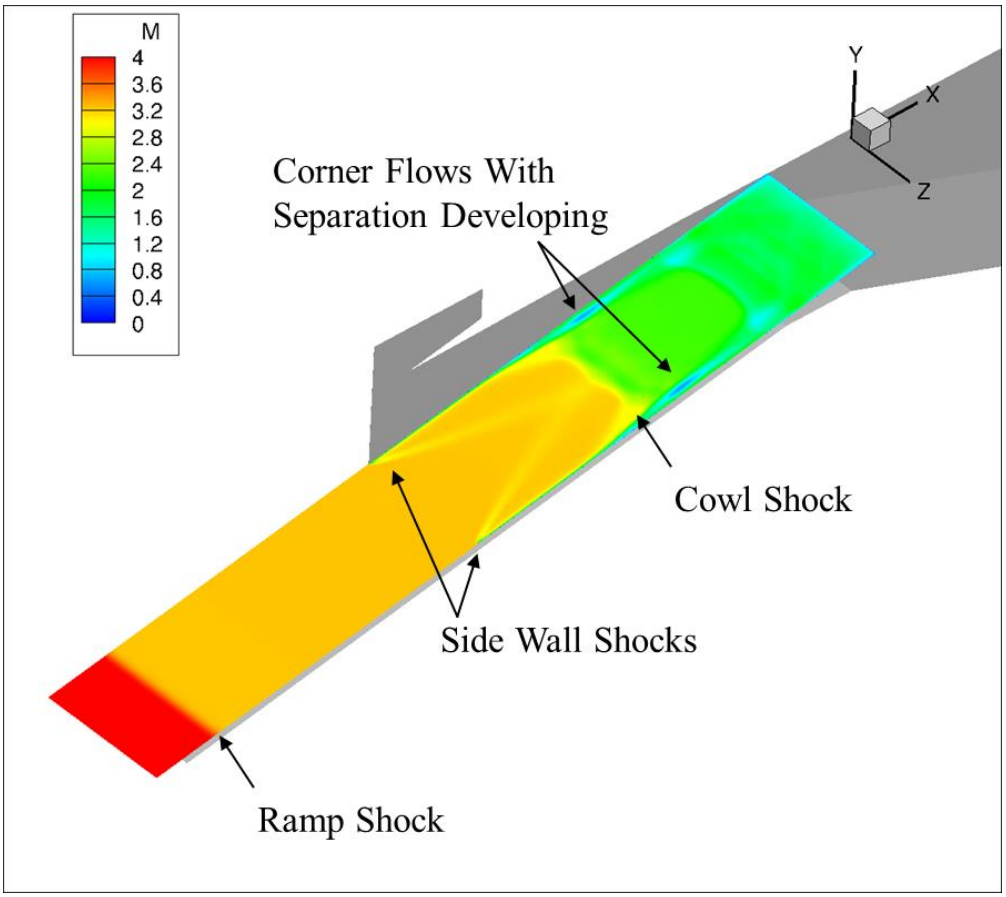

Figure 33: Mach Number Contours for the Fixed-Cowl Model at $\theta_c = 1.2$ deg along Plane 0.1 inches above the Inlet Ramp

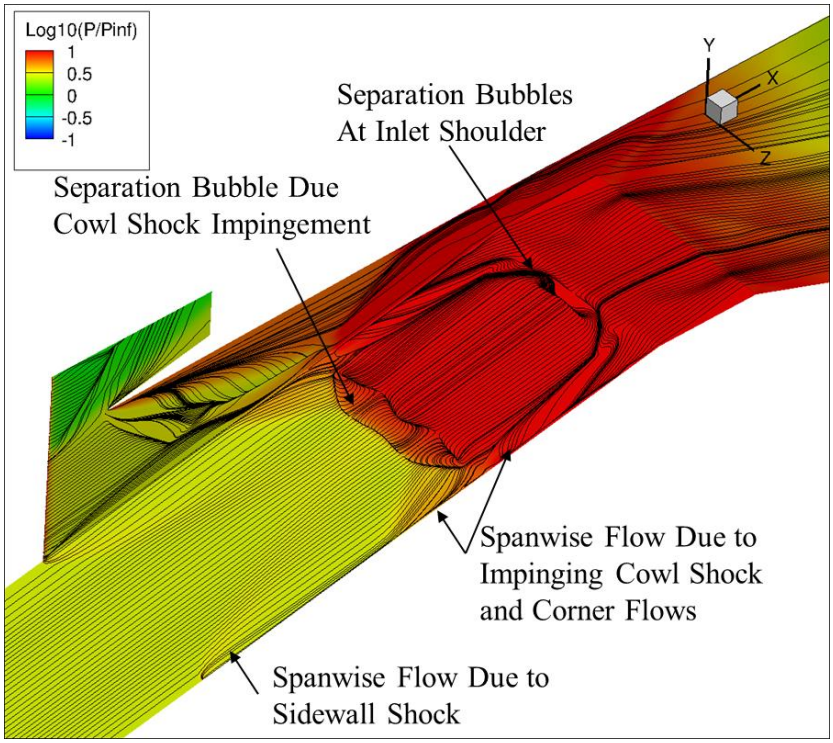

Figure 34: Simulated Oil Flow Lines and Log of the Pressure Ratio Contours along the Inlet Ramp and Sidewall for Cowl at $\theta_c = 1.2$ deg

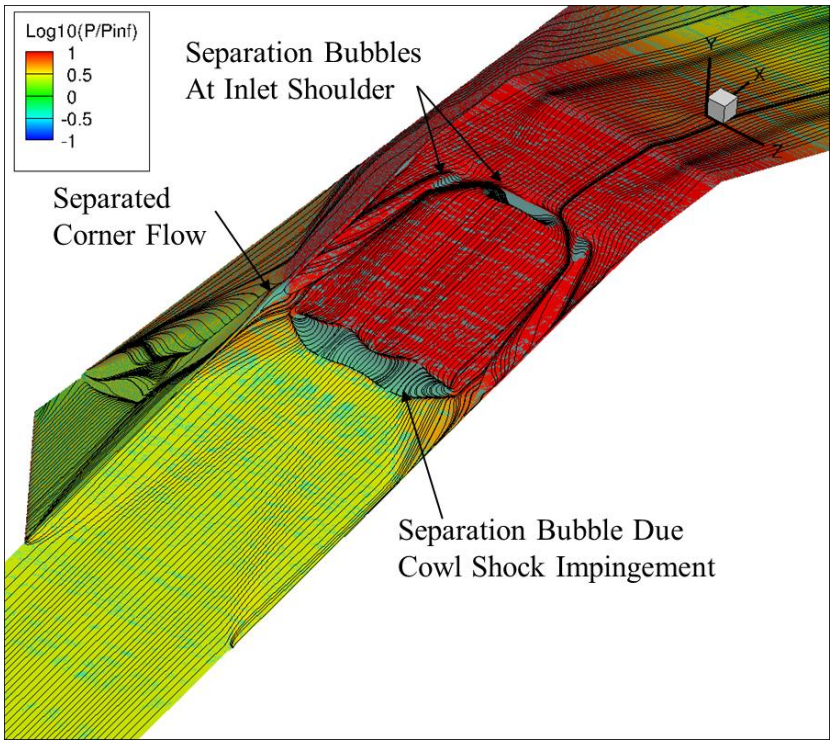

Figure 35: Simulated Oil Flow Lines and Log of the Pressure Ratio Contours along the Inlet Ramp and Sidewall for Cowl at $\theta_c = 1.2$ deg with Isosurface of U=0 showing Separated Flow Regions

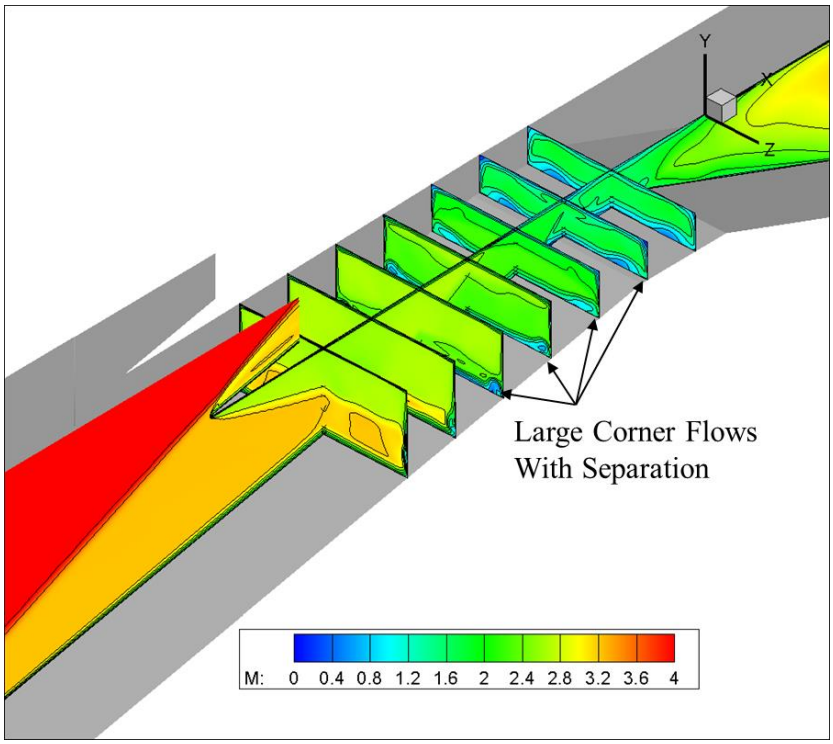

Figure 36: Spanwise and Centerline Mach Number Contours through the Inlet at $\theta_c = 1.2$ deg

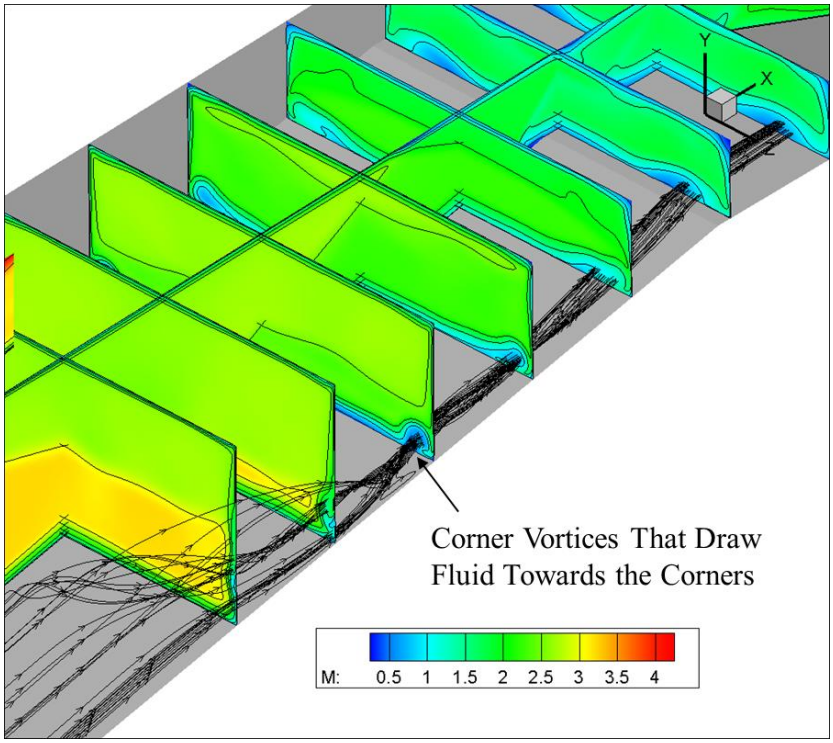

Figure 37: Streamlines Illustrating Corner Vortices that Develop in the Inlet at $\theta_c = 1.2$ deg

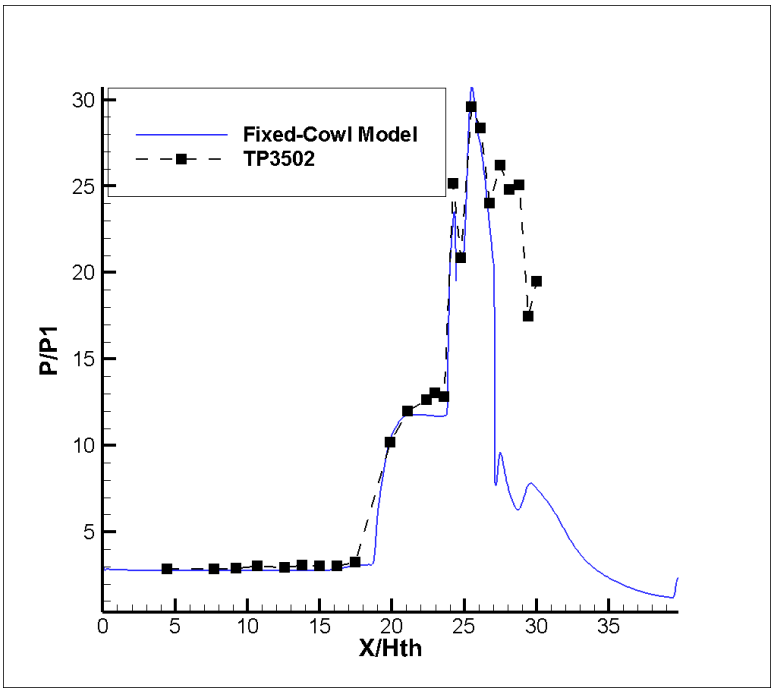

Figure 38: Comparison of the Normalized Centerline Wall Pressures from the Fixed-Cowl Model at $\theta_c =$ 1.2 deg and the Experimental Results of Ref. [3]

When the cowl is in the horizontal position (θ_c = 0 deg) the inlet is unstarted in the predictions shown in Figure 39. This is in agreement with the experimental data which also show the inlet to be unstarted with the cowl in the horizontal position. The flow field changes drastically at this point from that obtained at the previous cowl angle analyzed. The oblique shock wave at the leading edge of the ramp exists, but the shock train due to the cowl has been ejected from the inlet leading to a large separation region along the inlet ramp. This separation region causes two additional shock waves that eventually bring the flow in the separated region to a subsonic velocity. A region of supersonic flow exists along the lower surface of the cowl where the flow can expand through to the isolator. This is similar to the unstarted flow described in Ref. [26]. When the inlet is unstarted, the flow field is unsteady. The comparison of the centerline wall pressures made in Figure 41 are at a single instance in time from the steady-state model. The qualitative shape of the pressure distribution is obtained, but quantitatively, there is a substantial difference. This again is due to computing a steady-state solution to an inherently unsteady flow problem. There were significant unsteady fluctuations even in the steady-state solution. The pressures plotted in Figure 41 were obtained at a single iteration but the fluctuations may bring the computed pressures into better agreement at a later

iteration. Because the flow was known to be unsteady, a transient computation was conducted at this fixed cowl angle. Images of the oscillatory flowfield are shown in Figure 40.

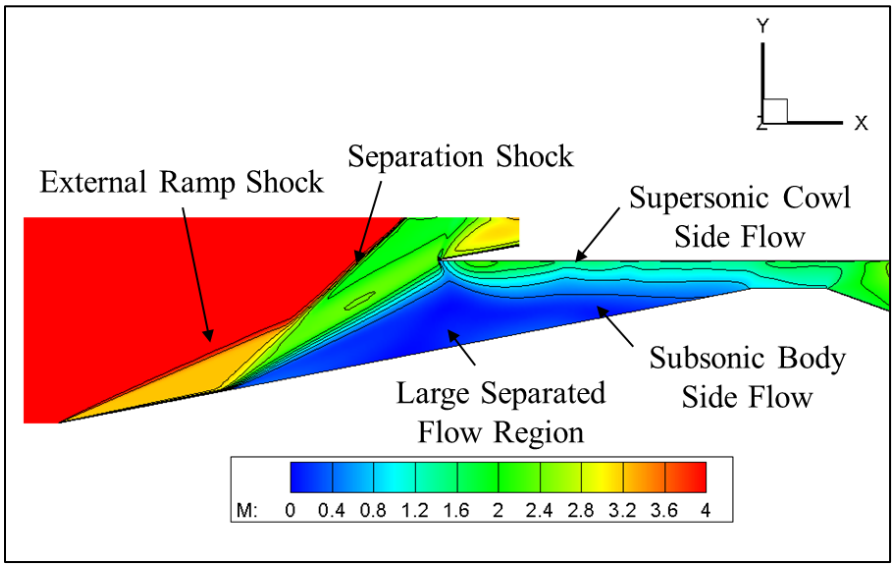

Figure 39: Centerline Mach Number Contours for the Fixed-Cowl Model at $\theta_c = 0$ deg

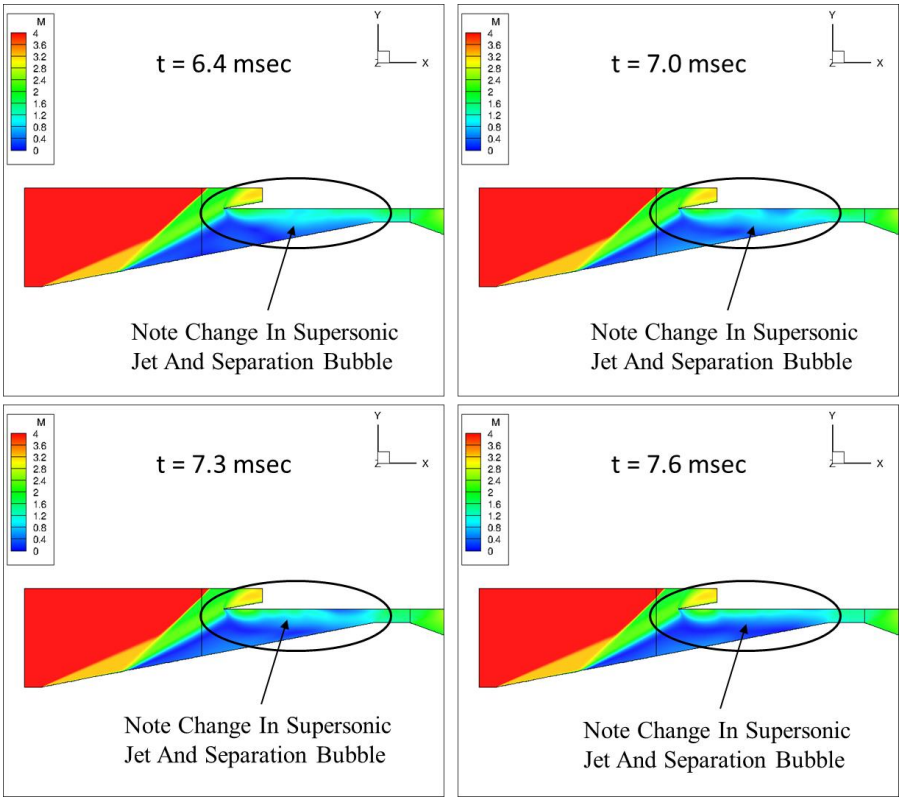

Figure 40: Time History of Centerline Mach Number Contours for the Fixed-Cowl Model at $\theta_c = 0$ deg for a Time-Accurate Simulation

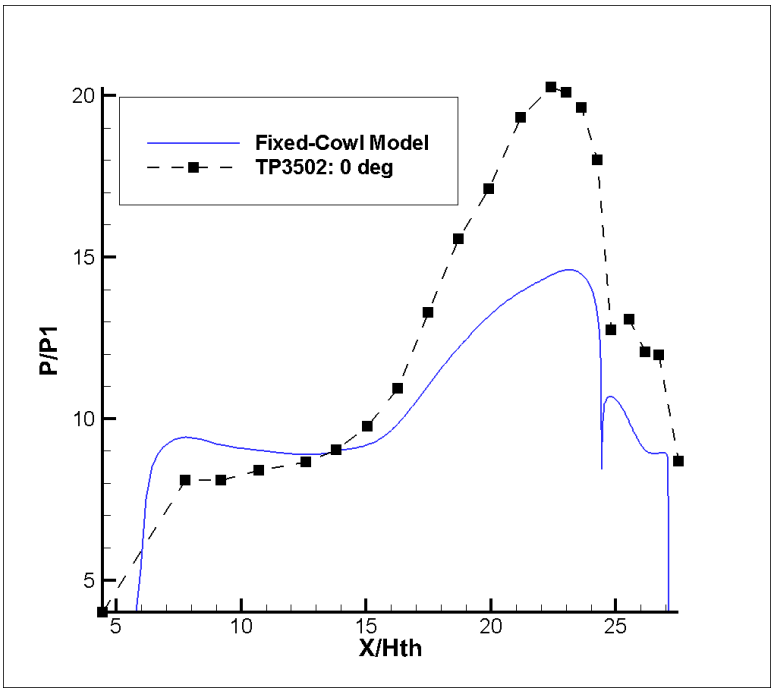

Figure 41: Comparison of the Normalize Centerline Wall Pressures from the Fixed-Cowl Model at $\theta_c = 0$ deg and the Experimental Results of Ref. [3]

The computed mass flow rates through the inlet at the three cowl angles are shown below in Figure 42. Also shown is the theoretically calculated values from Ref. [3]. Note, that the results in the figure are plotted as a function of the cowl convergence angle, $\beta = 11° - \theta_c$ for comparison with the results presented in Ref. [3].

The theoretical values from Ref. [3] are computed based on the geometric capture area of the inlet, H_{cap} given below in Equation 7.1. The capture area was adjusted to include the effects of the viscous boundary layer by subtracting a scalar multiple of the displacement thickness as shown in Equation 7.2. The inlet mass capture ratio, shown in Equation 7.3, was defined as the ratio of the actual mass flow rate through the inlet compared to the mass flow rate through the projected frontal area of the inlet model computed using the model height, $H_m = 2.3$ inches [3]. The mass flow rate through the projected frontal area of the inlet model was then computed using the isentropic flow relation in Equation 7.4 from the reservoir conditions.

$$H_{cap} = L_r \tan\alpha - L_c \sin\theta_c + H_{th} + \frac{\tan\alpha \tan\theta_w}{\tan\alpha \tan\theta_w} * \left[L_r\left(1 - \frac{\tan\alpha}{\tan\theta_w}\right) + L_c\left(\frac{\sin\theta_c}{\sin\theta_w} - \cos\theta_c\right) - H_{th}\left(\frac{1}{\tan\theta_w}\right)\right]$$

Equation 7.1

$$H_{cap,act} = H_{cap} - 1.876\,\delta^* \qquad \text{Equation 7.2}$$

$$CAP = \frac{H_{cap,act}}{H_m} \qquad \text{Equation 7.3}$$

$$\frac{\dot{m}}{A} = \frac{P_t\sqrt{\gamma}}{\sqrt{RT_t}} M \left(\frac{1}{1+\frac{\gamma-1}{2}M^2} \right)^{\frac{\gamma+1}{2(\gamma-1)}} \qquad \text{Equation 7.4}$$

The computed values from the Fixed-Cowl Model are slightly larger than that from the theoretical calculations at the cowl angles of $\theta_c = 8$ deg and 1.2 ($\beta = 3$ deg and 9.8 deg). This is most likely due to slight differences in the computed boundary layer thickness and displacement thickness that may be producing less blockage than considered in the theoretical calculations. When the cowl is in the horizontal position, the inlet is unstarted, which the theoretical approach cannot treat. When unstarted, an oscillatory flow develops as mentioned previously. This can be seen in Figure 43 which shows a time-history of the mass flow rate through the inlet obtained from the time-accurate solution discussed above. The mass flow rates are also summarized in Table 9. The average value is reported for the unstarted inlet. Note that the mass flow rate is reduced dramatically as the inlet is unstarted due to increased spillage as the shock train is ejected from the inlet and the formation of a large separation bubble and shock is created.

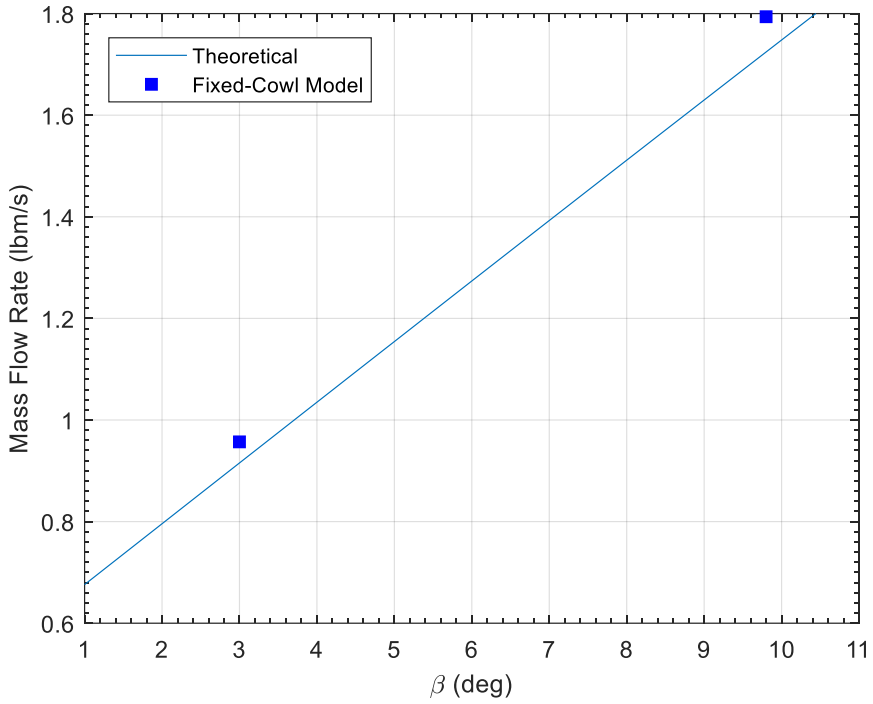

Figure 42: Comparison of Mass Flow Rates from the Fixed-Cowl Models with the Theoretical Values from Ref. [3] as a Function of the Cowl Convergence Angle

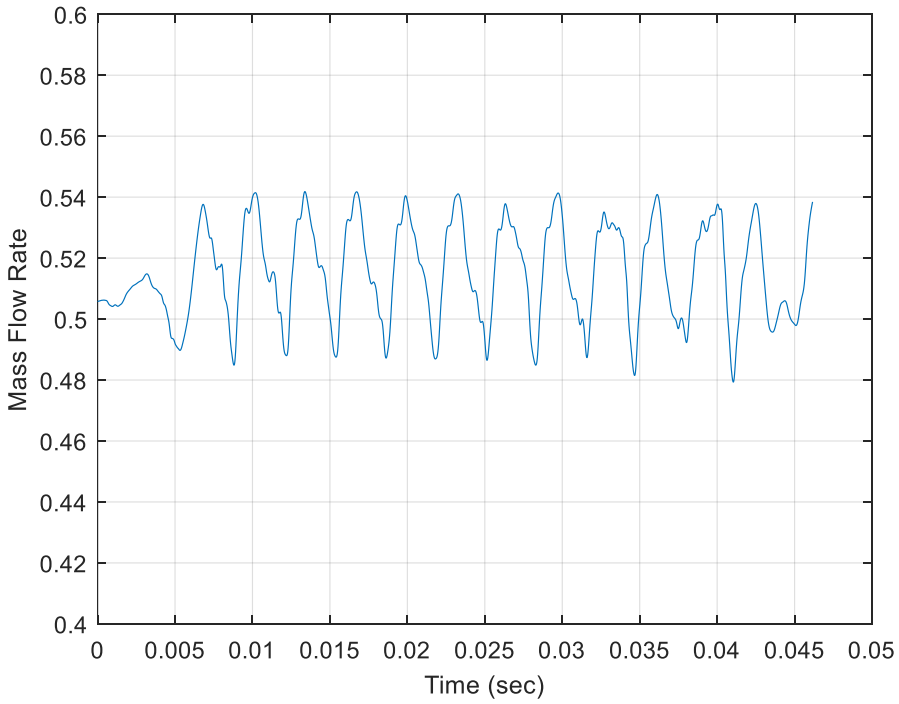

Figure 43: Time-History of the Mass Flow Rate through the Inlet when Unstarted at the Cowl Angle of $\theta_c = 0$ deg

Table 9: Mass Flow Rates from the Fixed-Cowl Model and the Theoretical Values from Ref. [3]

Cowl Angle (deg)	Mass Flow Rate (lbm/s)	Theoretical (Ref. [(2)])
8.0	0.956956	0.915439
1.2	1.793745	1.724371
0.0	0.514982*	1.865740**

* Averaged value reported due to flow oscillations
** Theoretical model does not account for unstart

7.1.2 Two-Dimensional Results

Although it was known that the flow field in the inlet is highly three-dimensional, several two-dimensional computations were conducted to highlight the importance of these effects. Results from the two-dimensional Fixed-Cowl Model are shown below. The centerline wall pressures are compared to the three-dimensional Fixed-Cowl Model and the experimental data in Figure 44, Figure 45, and Figure 46 for the cowl angles of 8 deg, 1.2 deg, and 0 deg, respectively. At the cowl angles of 8 deg and 1.2 deg, the two-dimensional results qualitatively compare well with the three-dimensional results and with the experimental data. However, quantitively there are significant differences. The pressures are consistently lower than the experimental data primarily due to not capturing the compression caused by the sidewall shocks. In addition, the lack of sidewalls means that the model does not include the effects of the corner flows that force the flow inward leading to additional compression waves.

When the cowl is in the horizontal position ($\theta_c = 0$ deg), the two-dimensional model predicts the inlet to be started which is contrary to the three-dimensional model and to the experimental data. Again, this is due to the fact that the two-dimensional results cannot capture the physics related to the corner flows which obviously play a driving factor in the inlet unstart process. This will be investigated further with the Variable-Cowl Model.

Figure 47 shows the computed mass flow rates through the inlet from the two-dimension model compared to that presented previously for the three-dimensional model and the theoretically calculated values from Ref. [3]. It is interesting to note that although the predicted pressures showed large differences between the

two-dimensional and three-dimensional model, the mass flow rates computed using the two-dimensional model seem to compare much better at the cowl angles of 8 and 1.2 deg. At 0 deg, the mass flow rate from the two-dimensional model is significantly different because the inlet is incorrectly predicted to be started. The mass flow rates from the two-dimensional model are slightly lower than the three-dimensional model when the inlet is started. This is because the flow rates computed using the two-dimensional model did not take into account the added capture area ahead of the sidewalls that was included in the three-dimensional model by accurately capturing the leading-edge radii of the sidewalls. The mass flow rates are tabulated in Table 10.

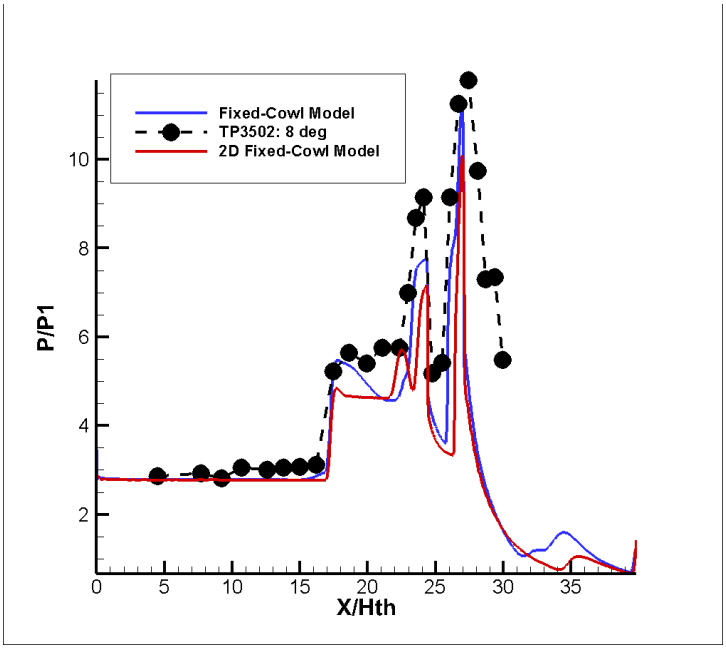

Figure 44: Comparison of the Normalized Centerline Wall Pressures from the 2D Fixed-Cowl Model at $\theta_c = 8$ deg with the Fully 3D Fixed-Cowl Model and with the Experimental Results of Ref. [3]

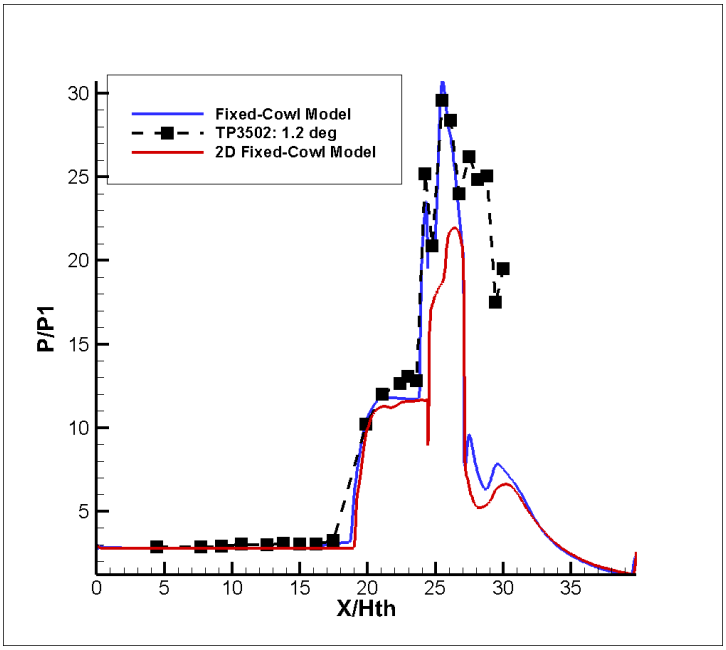

Figure 45: Comparison of the Normalized Centerline Wall Pressures from the 2D Fixed-Cowl Model at $\theta_c = 1.2$ deg with the Fully 3D Fixed-Cowl Model and with the Experimental Results of Ref. [3]

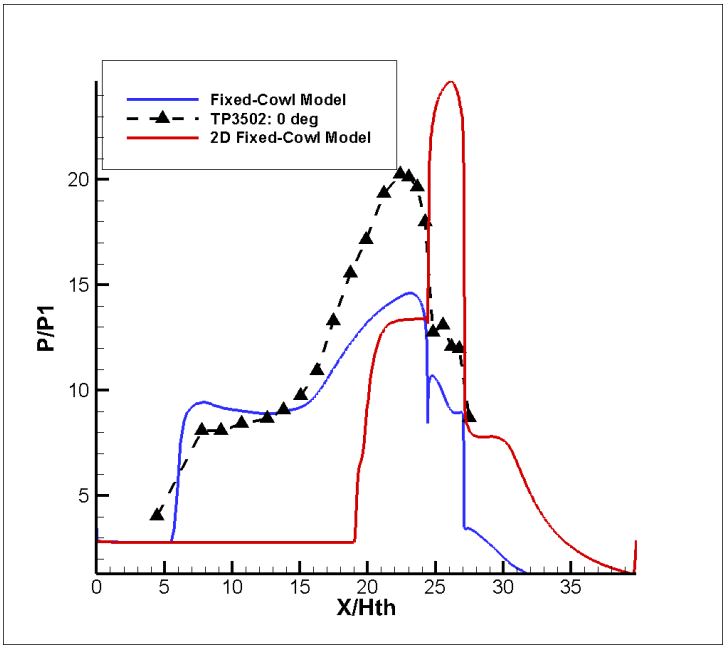

Figure 46: Comparison of the Normalized Centerline Wall Pressures from the 2D Fixed-Cowl Model at $\theta_c = 0$ deg with the Fully 3D Fixed-Cowl Model and with the Experimental Results of Ref. [3]

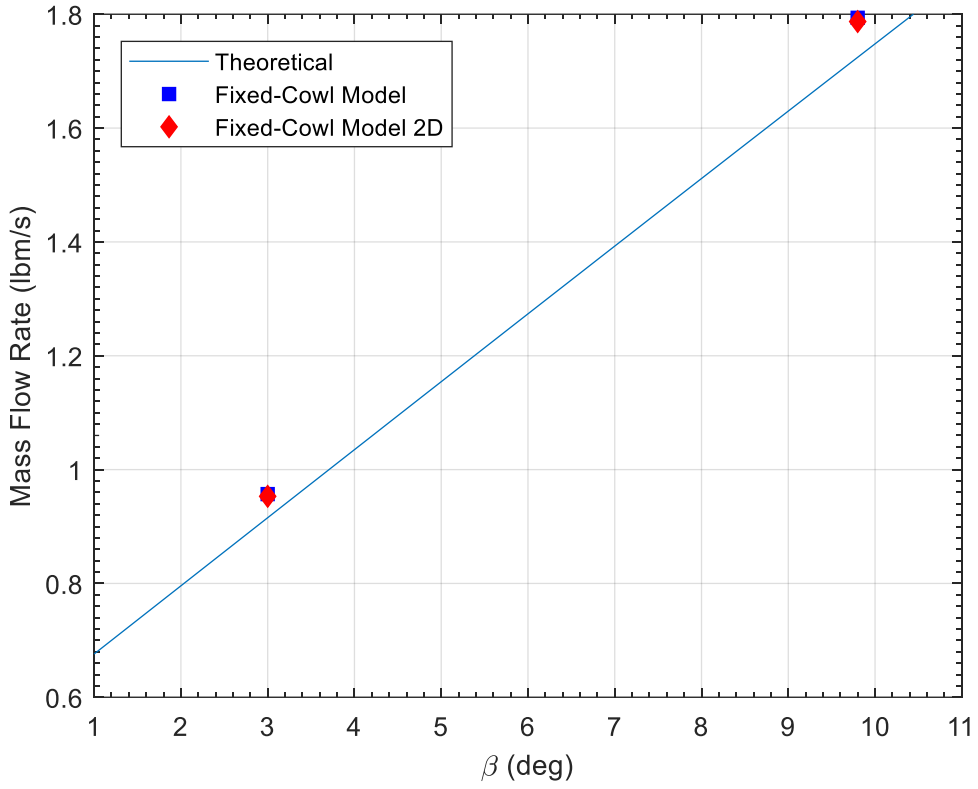

Figure 47: Comparison of Mass Flow Rates from the 2D and 3D Fixed-Cowl Models with the Theoretical Values from Ref. [3] as a Function of the Cowl Convergence Angle

Table 10: Mass Flow Rates Computed using the 2D Fixed-Cowl Model

Cowl Angle (deg)	Mass Flow Rate (lbm/s)	Theoretical (Ref. [3])
8.0	0.953028	0.915439
1.2	1.787136	1.724371
0.0	1.931168	1.865740

7.1.3 Turbulence Model Assessments

As mentioned in Section 4.2, the Reynolds-averaging process results in additional terms in the Navier-Stokes Equations that must be closed using a turbulence model. It is known that the turbulence model can have a significant impact on the computed flow solution in high-speed applications where there are significant effects due to shock-boundary layer interactions and flow separations [68, 69]. Therefore, it was necessary to compare the performance of different turbulence models for the current problem of study so as to understand the strengths and weaknesses of each model in computing the flow through a high-speed inlet

and to determine which model is best suited for the transient solutions obtained using the Variable-Cowl Model.

The experimental work presented in Ref. [3] included measurements of the local boundary layer profiles on the inlet ramp in the absence of the cowl to understand the characteristics of the boundary layer entering the inlet. The measurements were obtained at 6.81 inches aft of the leading edge of the inlet ramp with the cowl absent using a Pitot pressure probe that obtained vertical profile data starting at 0.016 inches off the ramp surface. These Pitot data were then converted to velocity and Mach number profiles. It was noted that the boundary layer thickness at this point on the inlet ramp was about 25% of the inlet throat height for the thin boundary layer case (no foreplate). These data were used for comparison with the computational results. To do this, the inlet body-side geometry was modeled without the cowl, in the same way the experimental data were, and boundary layer profiles were extracted at the same position as in the experiment, at x = 6.81 inches. The computational domain used is visible in Figure 48 and Figure 49.

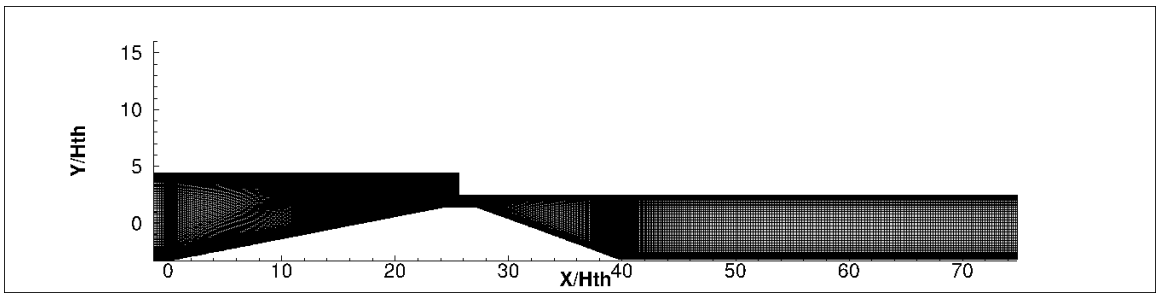

Figure 48: Inlet Body-Side Only Grid Used to Calculate Boundary Layer Profiles on the Ramp

.

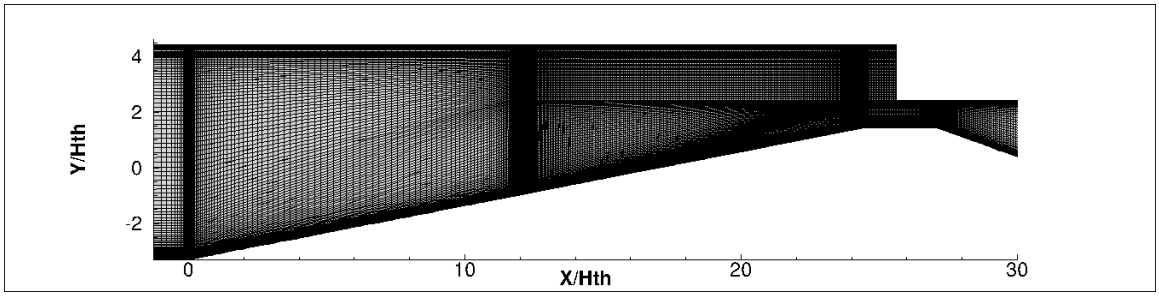

Figure 49: Inlet Body-Side Only Grid Used to Calculate Boundary Layer Profiles on the Ramp Enlarged to Show Inlet Ramp Details

The five different turbulence models described in Section 4.2 were used in the computation: the Cubic k- ε model (CKE), the Realizable k- ε model (RKE), the Reynolds-Stress Transport Model (RSTM), the Spalart-Allmaras model (SA), and the Menter SST model (SST). The profiles extracted from these results are shown and compared with the measured experimental profiles in Figure 50. In general, reasonable agreement is seen between the computed profiles and the measured profiles. It can be seen from the figure that the Cubic k-ε and Menter SST models result in the fullest profiles, whereas the Reynolds-Stress Transport Model (RSTM) results in the least full profile.

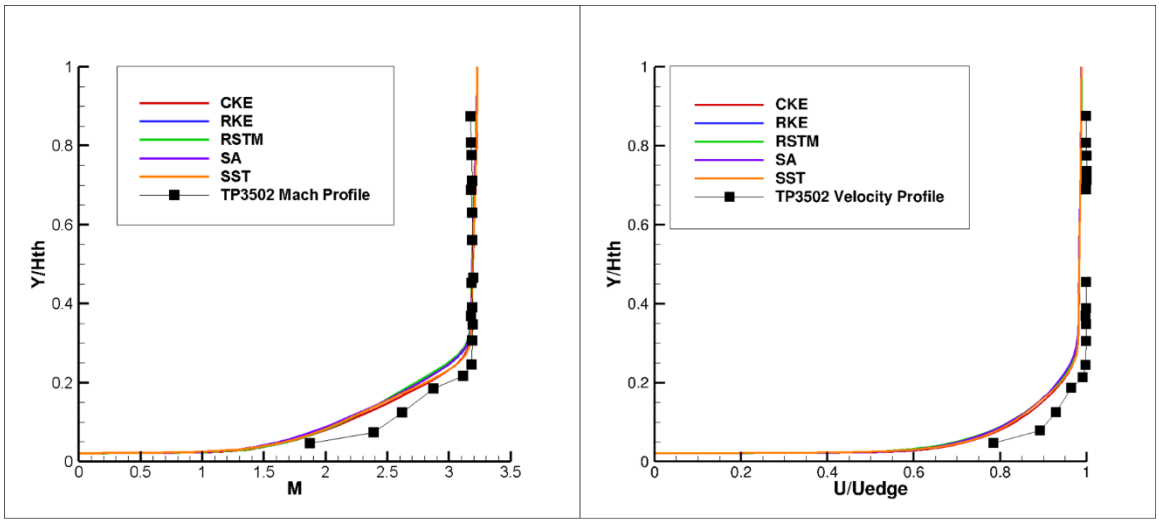

a) b)

Figure 50: a) Mach Number and b) Velocity Boundary Layer Profiles at x=6.81 inches Computed with a Range of Turbulence Models and Compared with Experimental Data from Ref. [3]

The profiles were also plotted in the Law-of-the-Wall format, shown in Figure 51. The boundary layer profiles are shown in non-dimensional form of $u^+ \equiv u/u_*$ as a function of the non-dimensional height, y^+. The profiles from the computations were obtained for compressible flow. Therefore, the Van-Driest transformation, shown below in Equations 7.5-7.7, was used to create an effective velocity, U_{eff}, so that they could be plotted in the Law-of-the-Wall form and compared against the incompressible Log Law [16].

$$U_{eff} = \frac{U_e}{B_1}\left\{\sin^{-1}\left[\frac{2B_1^2(U/U_e)-B_2}{\sqrt{B_2^2+4B_1^2}}\right] + \sin^{-1}\left[\frac{B_2}{\sqrt{B_2^2+4B_1^2}}\right]\right\} \qquad \text{Equation 7.5}$$

$$B_1 = \sqrt{\frac{\gamma-1}{2} M_e^2 \left(\frac{T_e}{T_w}\right)} \qquad \text{Equation 7.6}$$

$$B_2 = 1 + \frac{\frac{\gamma-1}{2} M_e^2}{T_w/T_e} \qquad \text{Equation 7.7}$$

Included in the plot are the empirical relations for the velocity profiles in the laminar sublayer, $u^+ = y^+$, and the incompressible Log-Law, $u^+ = 2.5\ln(y^+) + 5.5$. It can be seen that all turbulence models accurately predict the velocity profile in the laminar sublayer; however, the exact extent of the sublayer is slightly different between models. Similarly, all models show a log-region outside of the sublayer. Overall, the Cubic k-ε is seen to most closely replicate the Law-of-the-Wall.

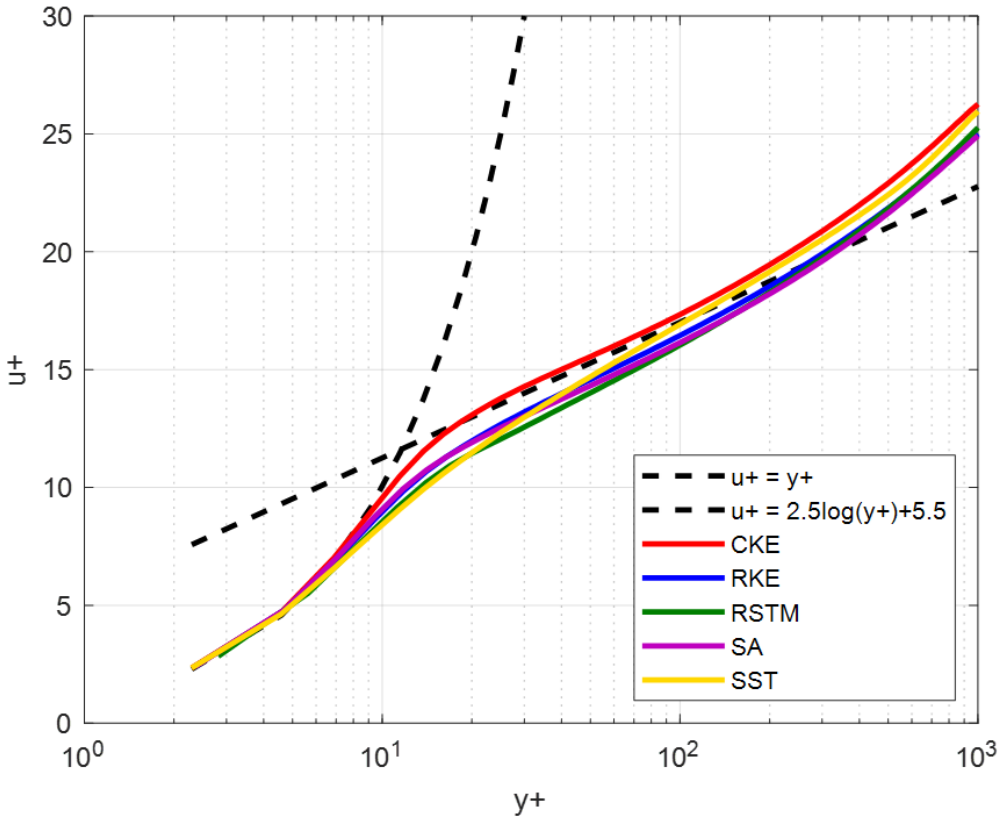

Figure 51: Law of the Wall Plot of Computed Boundary Layer Profiles Using Different Turbulence Models

Computed boundary layer characteristics are also compared with the measured values in Table 11. The boundary layer thickness was taken to be the point at which the velocity reached 99% of the value behind

the ramp shock. The 99% metric was chosen to match what was done in the experimental analysis of Ref. [3]. The displacement thickness and momentum thickness were computed by numerically integrating the boundary layer profiles in accord with Equations 7.8 and 7.9, respectively. In these equations, δ is the boundary layer thickness, ρ is the density, u is the velocity and y is the coordinate normal to the surface. In addition, the skin friction coefficient reported for the experiment was not obtained directly from measurements due to the inability to obtain an adequate number of data points in the near-wall region [3]. Therefore, an empirical correlation was used [3]. The skin friction from the computations is lower than that from the experiment. This could be due to assuming the walls were adiabatic in the computation. If the walls were at a temperature lower than the recovery temperature, this would lead to a higher skin friction coefficient.

$$\delta^* = \int_0^\delta \left(1 - \frac{\rho(y)u(y)}{\rho_e u_e}\right) dy \qquad \text{Equation 7.8}$$

$$\theta = \int_0^\delta \frac{\rho(y)u(y)}{\rho_e u_e}\left(1 - \frac{u(y)}{u_e}\right) dy \qquad \text{Equation 7.9}$$

As can be seen in Table 11, the boundary layer thickness and the displacement thickness agree well with the data reported in Ref. [3]. However, the momentum thicknesses from the computations show much larger discrepancies. The shape factor, defined as $H = \delta^*/\theta$, for the experimental data is 1.94, whereas the shape factor from the computations range between 5.46 and 5.69. It is interesting to note, however, that the correlation given in Equation 7.10, from Ref. [70], yields a shape factor of 5.57 for a Mach number of 3.23 which is the freestream Mach number behind the ramp shock. In the computations, the inlet walls were modeled as adiabatic so that the $T_r = T_w$ in Equation 7.10.

$$H = 1.4 + 0.4M^2 - 1.222T_r\left(1 - \frac{T_w}{T_r}\right) \qquad \text{Equation 7.10}$$

In addition, the value of $\rho_e u_e$ was cited as 127.18 lbm/ft^2-sec in Ref. [3] and was calculated to be 115.80 lbm/ft^2-sec using the Cubic k-ε model. Therefore, despite the disagreement in momentum thickness with the experimental data, the boundary layer profiles computed were considered to be validated.

Table 11: Boundary Layer Parameters for Flow Over the Inlet Ramp (No Cowl Present and no Foreplate)

Data Source	Boundary Layer Thickness, δ (inches)	Displacement Thickness, δ^* (inches)	Momentum Thickness, θ (inches)	Skin Friction Coefficient, c_f (---)
Experiment (Ref. [3])	0.1	0.036	0.0185	0.00207
Cubic k-ε Model	0.1055	0.03219	0.0058	0.00124
Realizable k-ε Model	0.1124	0.03466	0.0062	0.00131
Reynolds-Stress Transport Model	0.1085	0.03443	0.0064	0.00137
Spalart-Allmaras Model	0.1133	0.03507	0.0063	0.00132
Menter SST Model	0.1041	0.03332	0.0059	0.00126

To assess the impact of turbulence model on the calculation of the performance of the inlet, two cowl angles were modeled, $\theta_c = 8$ deg, and 1.2 deg ($\beta = 3$ deg, and 9.8 deg). Comparisons of the centerline pressures were made with the experimentally measured data from Ref. [3]. The comparisons were again made with the same turbulence models as mentioned above, except for the Reynolds-Stress Transport Model which failed to yield a converged solution. This was most likely due to the addition of the seven equations making the numerical problem stiffer and less stable. Figure 52 and Figure 53 show this comparison for cowl angles at $\theta_c = 8$ deg and 1.2 deg, respectively. Along the inlet ramp, on the external surface of the inlet ahead of the cowl, all of the models show essentially the same pressures values. However, as the flow enters the inlet and encounters the first shock-boundary layer interaction caused by the cowl shock impinging on the inlet ramp, the models begin to show differences. All models show an underprediction in the pressure on the aft side of the interaction region. Similarly, at the second interaction due to impingement of the reflected shock of the underside of the cowl, all of the models show an underprediction in the pressure rise at the interaction. The Realizable k-ε Model, the Spalart-Allmaras model, and the Menter SST model all predict a pressure rise closest to that measured in the experimental data, while the Cubic k-ε model is the farthest off. Finally, at the third shock interaction, again, the

Realizable k-ε model and the Menter SST model agree well in magnitude with the experimental data. However, now, the Cubic k-ε model is closer to the experimental data than the Menter SST model. Based on the results presented in Figure 52, one might suggest that the Spalart-Allmaras model should be used, because it seems to more closely match the pressure rises at the shock-boundary layer interactions.

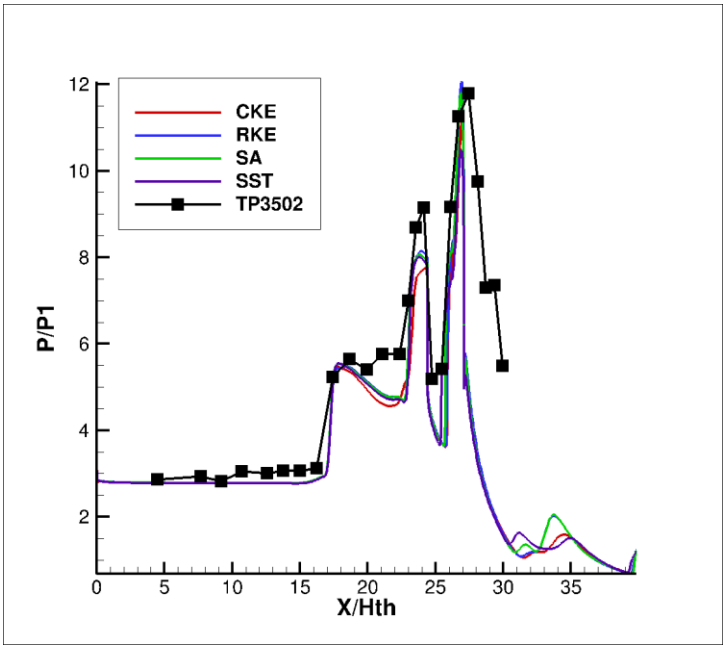

Figure 52: Comparison of Normalized Centerline Wall Pressures between Various Turbulence Models and Experimental Data from Ref. [3] at Cowl Angle $\theta_c = 8$ deg

However, at the second cowl angle, $\theta_c = 1.2$ deg, where the cowl is nearly horizontal which leads to a stronger cowl shock and thus stronger shock-boundary layer interactions, the Spalart-Allmaras model actually predicts that the inlet should be unstarted. The Menter SST model also predicts the inlet to be unstarted whereas the two k-ε models predict the inlet to be started, as was observed experimentally. Based on all of this, the Cubic k-ε was chosen to be used for the current work as capturing the unstart point properly was desired.

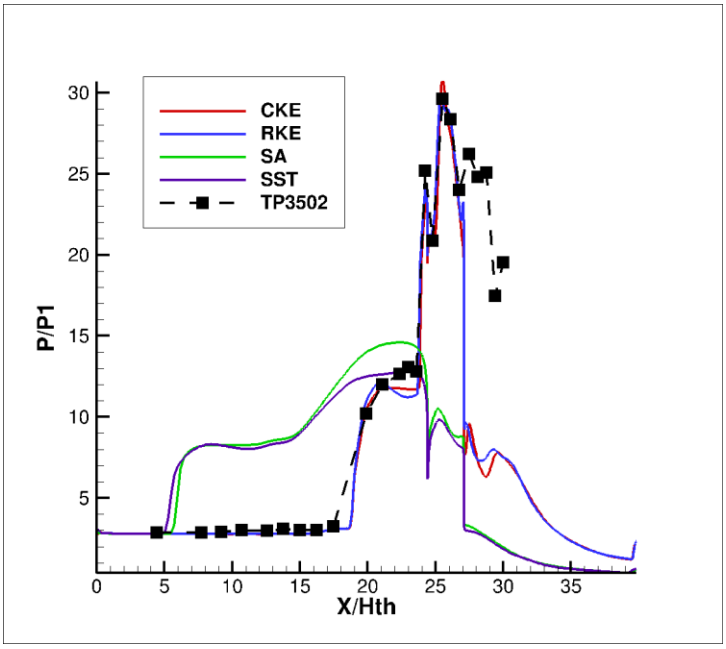

Figure 53: Comparison of Normalized Centerline Wall Pressures between Various Turbulence Models and Experimental Data from Ref. [3] at Cowl Angle $\theta_c = 8$ deg

7.2 Unsteady Variable-Cowl Model Results

This section presents the main focus of the current work; the three-dimensional, unsteady flow results obtained using the Variable-Cowl Model. First, comparisons are made with the Fixed-Cowl Model using a series of quasi-steady solutions at the same discrete cowl angles. From there, the full, three-dimensional, transient, relative motion analyses are presented. A summary of the results obtained from the Variable-Cowl Model is presented in Table 12. The steady-state cases were used to compare the Variable-Cowl Model to the Fixed-Cowl Model as described in Section 7.2.1, while the transient cases were used to obtain time-accurate solutions as the inlet progressed from the started to unstarted states, and back, as presented in Section 7.2.2. In Section 7.2.3, the role of the corner flows is addressed in detail. Following this, the effect of cowl rotation rate is investigated in Section 7.2.4. The two-dimensional cases, used to highlight the three-dimensionality of the flow field, are discussed in Section 7.2.5. Finally, Section 7.2.6 investigates the effect of a second turbulence model on the results.

Table 12: Summary of the Variable-Cowl Model Cases

Name	Turbulence Model	Time Step	Cowl Rotation Rate
Steady-State Cases			
Steady-State 8 deg Cowl	Cubic k-ε	**N/A**	**N/A**
Steady-State 1.2 deg Cowl	Cubic k-ε	**N/A**	**N/A**
Steady-State 0 deg Cowl	Cubic k-ε	**N/A**	**N/A**
Three-Dimensional, Unsteady Cases			
Baseline	Cubic k-ε	10 μs	10 rad/s
Medium Rotation Rate	Cubic k-ε	10 μs	5 rad/s
Slow Rotation Rate	Cubic k-ε	10 μs	1 rad/s
Coarse Time Step	Cubic k-ε	100 μs	10 rad/s
Fine Time Step	Cubic k-ε	1 μs	10 rad/s
SST Baseline	Menter SST	10 μs	10 rad/s
SST Coarse Time Step	Menter SST	100 μs	10 rad/s
SST Fine Time Step	Menter SST	1 μs	10 rad/s
Two-Dimensional, Unsteady Cases			
Baseline	Cubic k-ε	10 μs	10 rad/s
Medium Rotation Rate	Cubic k-ε	10 μs	5 rad/s
Slow Rotation Rate	Cubic k-ε	10 μs	1 rad/s

7.2.1 Comparison of the Variable-Cowl Model with the Fixed-Cowl Model

Prior to conducting the fully transient computations, several steady-state cases were conducted using the Variable-Cowl Model with the overset grid at the same cowl angles that were modeled using the Fixed-Cowl Model. This was done to verify that the Variable-Cowl Model was consistent with the Fixed-Cowl Model, and with the experimental data. Figure 54 compares computed schlieren images along the duct centerline for both the Fixed-Cowl Model and the Variable-Cowl Model at $\theta_c = 8$ deg. The main features of the cowl shock and the ensuing shock train compare well with the Fixed-Cowl Model. There seem to be small differences visible behind the first reflection off the cowl and the second reflection off the ramp, where a second reattachment shock is not as pronounced in the Variable-Cowl Model as in the Fixed Cowl-Model. However, as seen in Figure 55, the normalized wall pressures along the duct centerline are reproduced well with the Variable-Cowl Model and match the experimental data. There is an underprediction of the peak pressure at the transition to the isolator by the Variable-Cowl Model. This is possibly due to the tiny gap between the cowl and the sidewall that allows for high pressure fluid to escape.

Similar comparisons at $\theta_c = 1.2$ deg are presented in Figure 56 and Figure 57. Again, small differences in the interaction region can be seen, but the centerline wall pressures compare well to each other and to the experimental data. Figure 58 and Figure 59 show results obtained with the cowl set to $\theta_c = 0$ deg. Both the Fixed-Cowl Model and the Variable-Cowl model show the inlet to be unstarted, which is in agreement with the experimental data. The pressures obtained from the computations do not agree well with the experimental data, which is not unexpected as previously mentioned. This is because when the inlet is unstarted, there is massively separated flow, and the flow field is largely unsteady. Therefore, there is no true steady-state solution. The main takeaway at this cowl angle is that both models correctly predict the inlet to be unstarted.

Finally, mass flow rates obtained at these cowl angles are compared to those obtained with the Fixed-Cowl Model and the theoretically calculated values from Ref. [3] in Figure 60 and Table 13. Again, good agreement is noted with a maximum percent difference between the two models of 6.8%. This maximum difference is for the unstarted case at θ_c = 0 deg, which again is inherently unsteady. Therefore, the difference may be purely due to the oscillations. If only the first two angles when the inlet is started are considered, the maximum percent difference is only about 1.2%.

Overall, the agreement between the Variable-Cowl Model and the Fixed-Cowl Model is good. This proves that the Variable-Cowl Model is consistent with the Fixed-Cowl Model for steady-state cases. Next, the Variable-Cowl Model will be used to compute transient flow response to the cowl rotational motion.

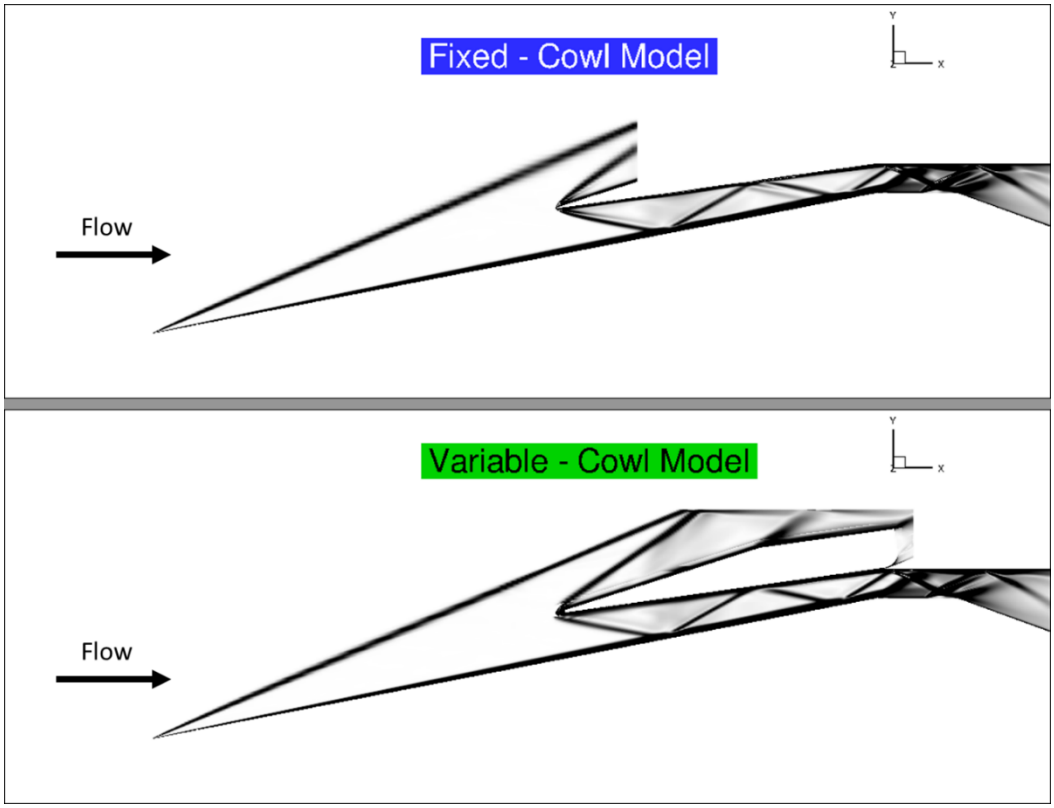

Figure 54: Comparison of Shock Structure in Simulated Schlieren Images from the Variable-Cowl Model and the Fixed-Cowl Model at the Static Cowl Angle of $\theta_c = 8$ deg

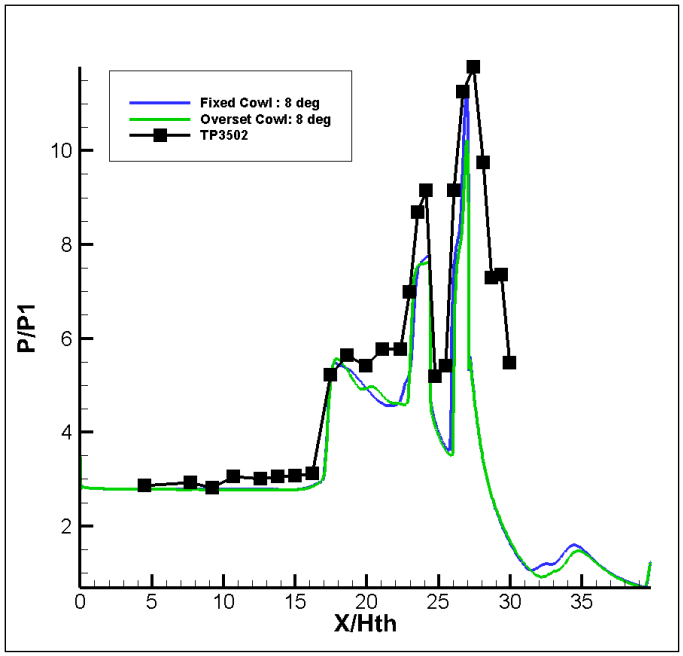

Figure 55: Comparison Normalized Centerline Wall Pressures from the Variable-Cowl Model and the Fixed-Cowl Model at the Static Cowl Angle of $\theta_c = 8$ deg

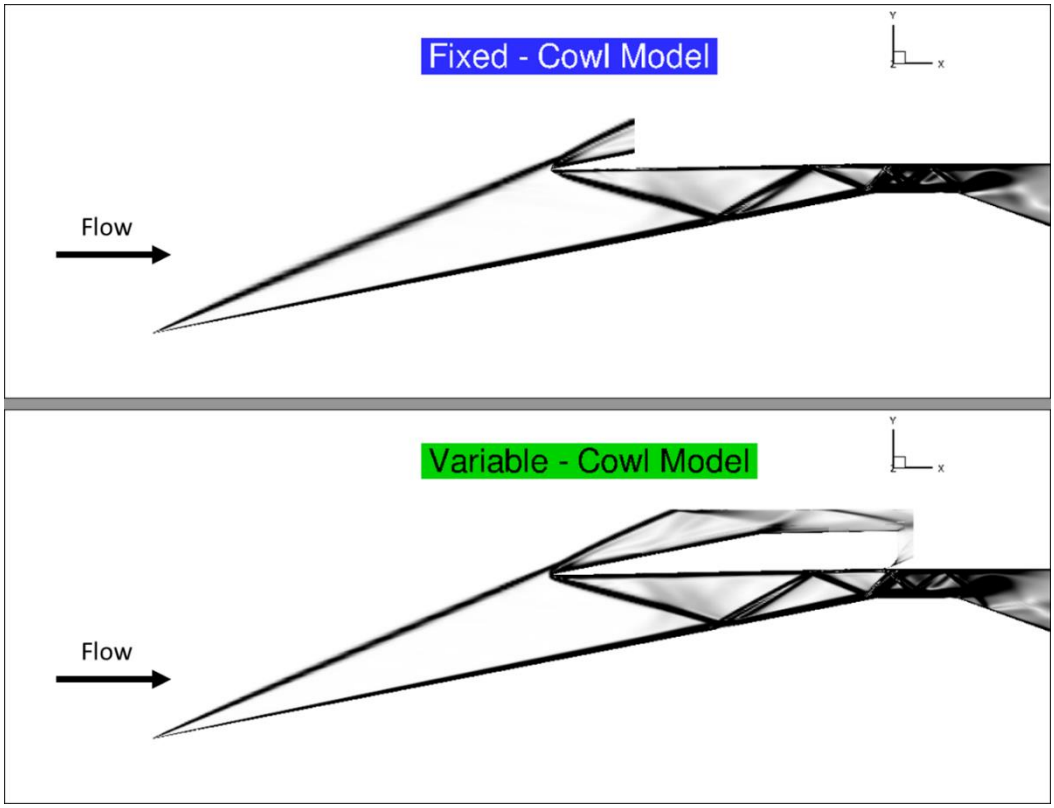

Figure 56: Comparison of Shock Structure in Simulated Schlieren Images from the Variable-Cowl Model and the Fixed-Cowl Model at the Static Cowl Angle of $\theta_c = 1.2$ deg

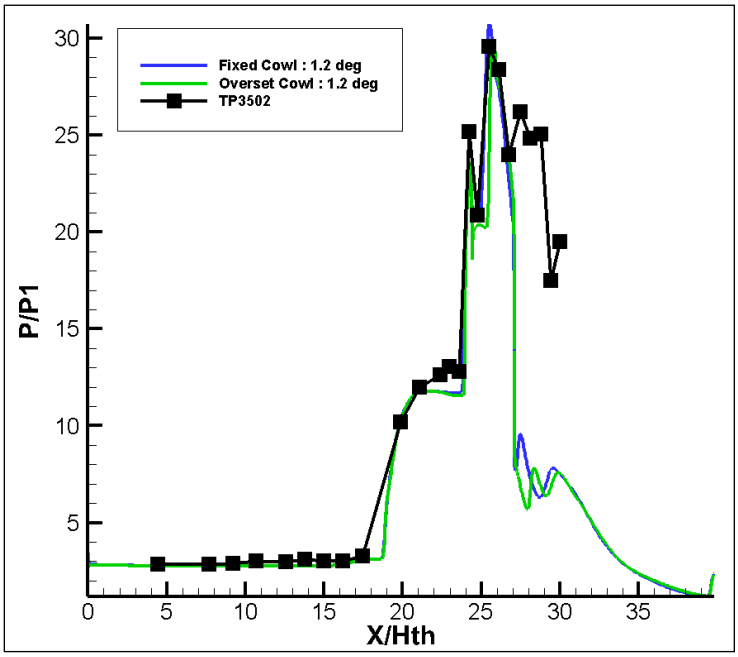

Figure 57: Comparison Normalized Centerline Wall Pressures from the Variable-Cowl Model and the Fixed-Cowl Model at the Static Cowl Angle of $\theta_c = 1.2$ deg

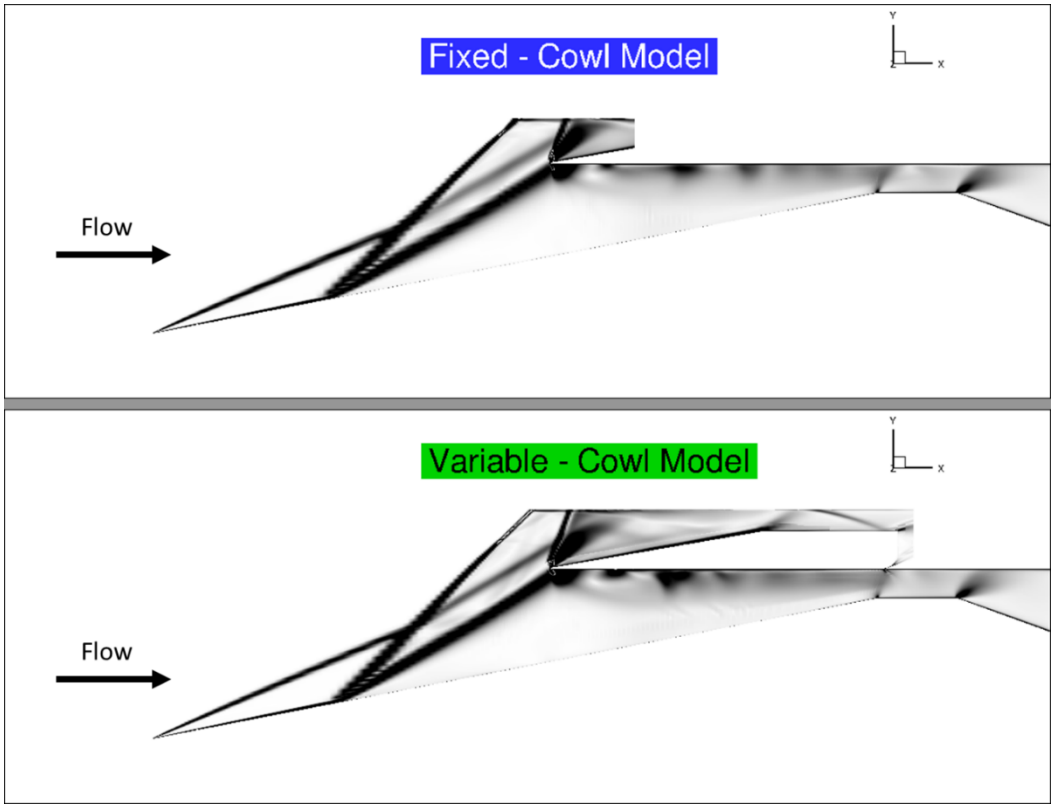

Figure 58: Comparison of Shock Structure in Simulated Schlieren Images from the Variable-Cowl Model and the Fixed-Cowl Model at the Static Cowl Angle of $\theta_c = 0$ deg

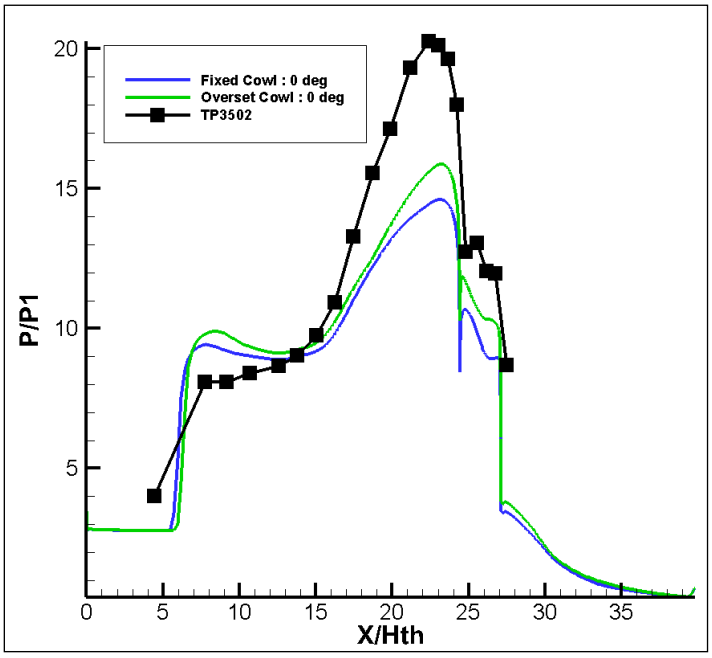

Figure 59: Comparison Normalized Centerline Wall Pressures from the Variable-Cowl Model and the Fixed-Cowl Model at the Static Cowl Angle of $\theta_c = 0$ deg

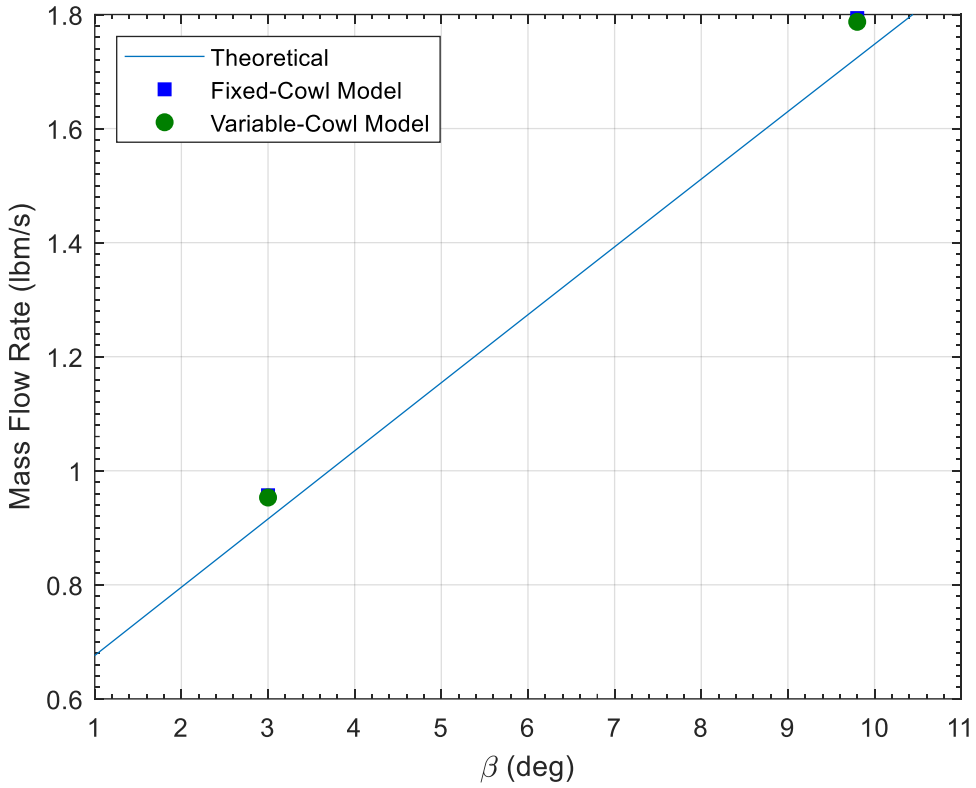

Figure 60: Comparison of Mass Flow Rates from Fixed-Cowl Model and Variable-Cowl Model with the Theoretical Values from Ref. [3] as a Function of the Cowl Convergence Angle

Table 13: Mass Flow Rates Through the Inlet for the Fixed-Cowl Model and the Variable-Cowl Model

Cowl Angle, θ_c (deg)	**Fixed-Cowl Model (lbm/s)**	**Variable-Cowl Model (lbm/s)**	**Percent Difference (%)**
8.0	0.956956	0.945965	1.2
1.2	1.793745	1.79771	0.2
0.0	0.506756	0.542294	6.8

7.2.2 Cowl Rotation Cases

After verifying that the Variable-Cowl Model was consistent with the Fixed-Cowl Model with respect to computing the steady-state flow through the inlet, the Variable-Cowl Model was used to investigate the transient response of the inlet to the rotational motion of the cowl. In these computations, the freestream conditions were the same as used previously and cited in Table 1. In all cases, the cowl was initially set to $\theta_c = 8$ deg, and a converged steady-state solution was obtained. This steady-state solution was used as the

initial conditions for the transient computations. In the transient computations, the inlet cowl was rotated from 8 deg below the horizontal ($\theta_c = 8$ deg) to the horizontal position ($\theta_c = 0$ deg). When the inlet reached close to horizontal, the inlet would unstart and the internal shock train would be ejected from the inlet, and an unsteady, oscillatory flow would set up outside the inlet as described previously. The cowl was held in the horizontal position for 30 ms for the unsteady flow to reach a stable oscillatory pattern, then the inlet cowl was rotated back to the 8 deg position allowing the inlet to restart on the way. The rotational motion of the cowl is depicted in Figure 61 at the baseline rotation rate of 10 rad/s.

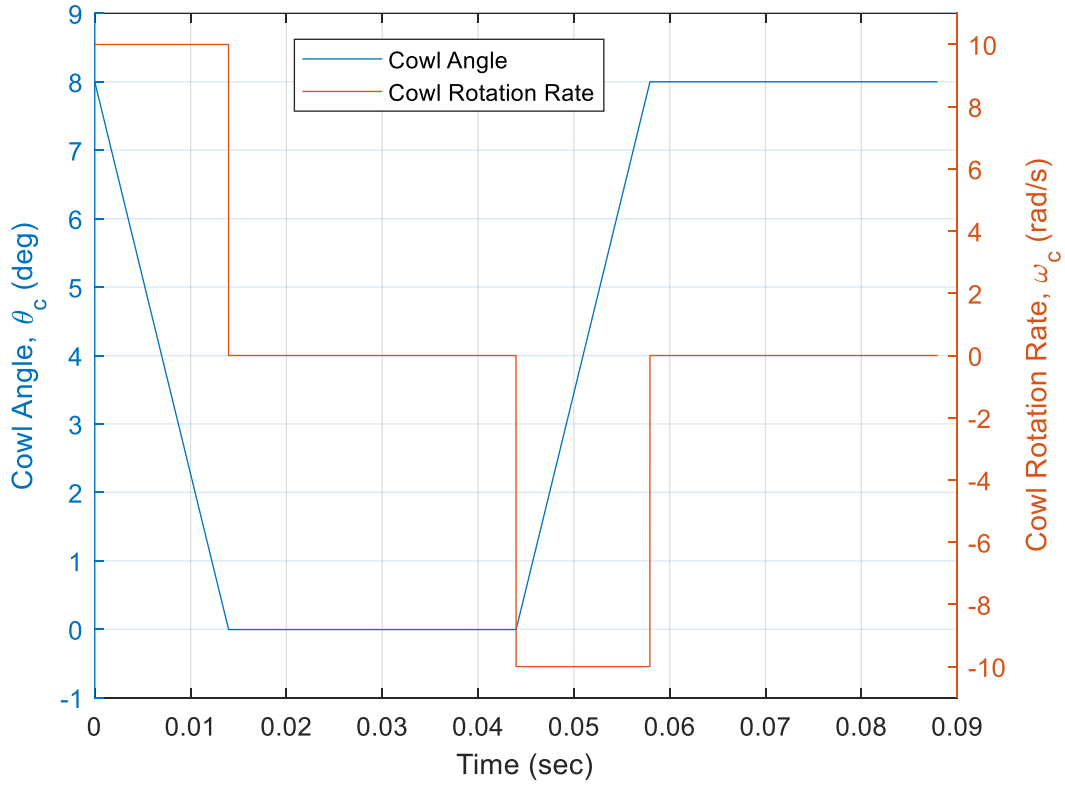

Figure 61: Cowl Angle, θ_c, and Rotation Rate, ω_c, as a Function of Time for the Baseline Transient Computation for the 10 rad/s Cases

Results from the Variable-Cowl Model for the baseline case are shown in Figure 62. This figure shows centerline Mach number contours during the opening of the cowl, the holding of the cowl at the horizontal position, and then the closing of the cowl at 10 ms increments. The result was obtained using the baseline turbulence model, the Cubic k-ε model, the baseline time step, 10 μs, and the baseline rotation rate, 10 rad/s. The figure shows the change in position of the shock train as the cowl is rotated. The progression of

the inlet from the started state to the unstarted state and back is clearly visible. The time history of the mass flow rate through the inlet during the process of rotating the cowl is shown below in Figure 63. The point of inlet unstart is clearly visible in the figure as the significant reduction in mass flow rate caused by spillage as a separation bubble blocks the inlet. The restart point is also visible where the inlet reaches the steady-state mass flow rate again. The cowl angles of unstart and restart are θ_c = 0 deg and 8 deg (β = 11 deg and 3 deg), respectively. This compares well to the data reported in Figure 16a of Ref. [3] which shows the inlet unstart and restart angles of about θ_c = 0.8-1.0 deg and 7.9-8.4 deg (β = 10-10.2 deg and 2.6-3.1 deg), respectively. It should be noted that in the current work, the point of unstart was chosen to be the point of peak mass flow rate immediately before the steep drop in mass flow rate and the point of restart was the point at which the mass flow rate recovers to the steady-state started value.

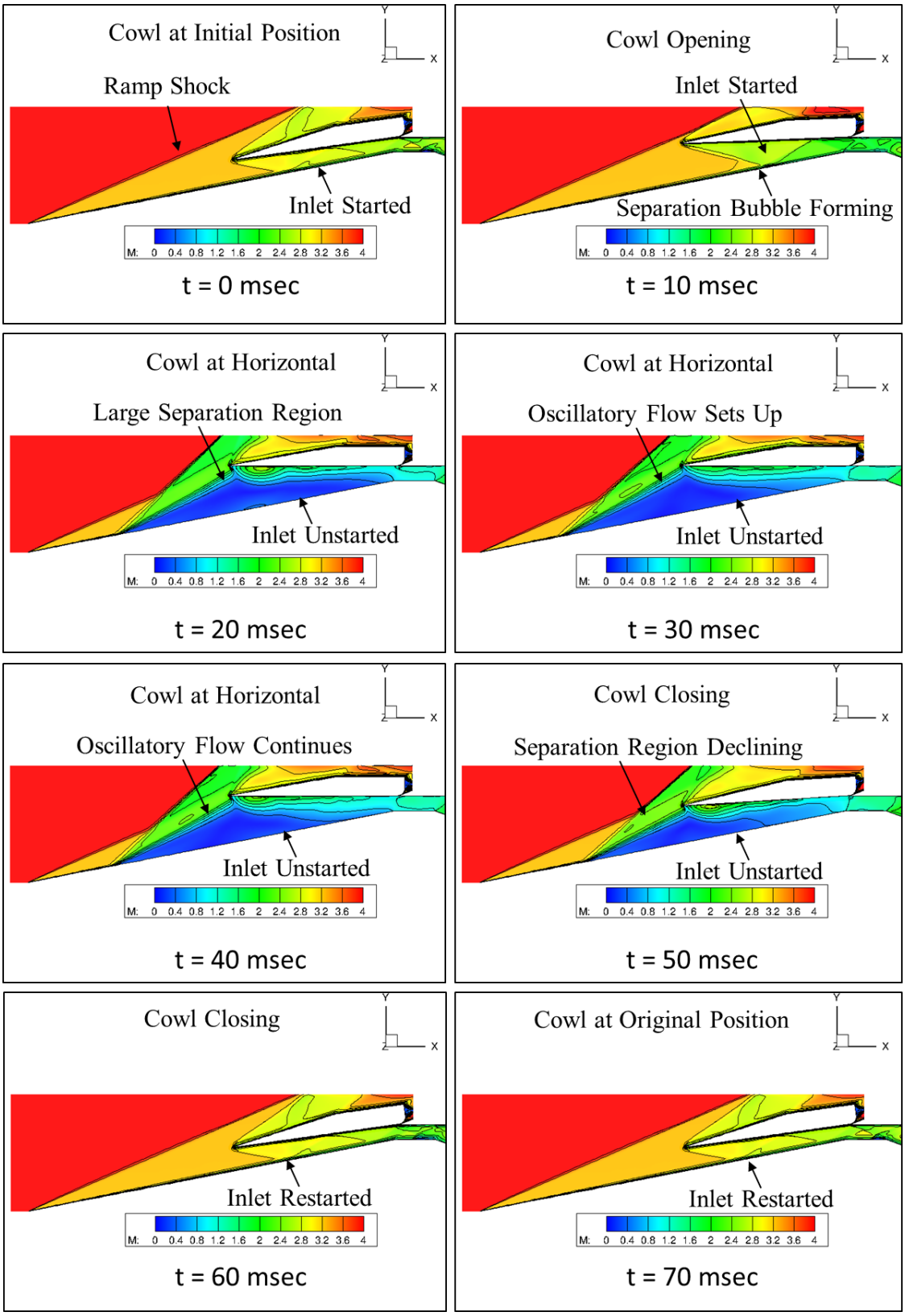

Figure 62: Centerline Mach Number Contours During Inlet Opening, Holding at the Horizontal Position, and Closing Obtained from a Three-Dimensional, Transient Computation Using the Variable-Cowl Model

In addition, it is known that the unstart process leads to large increases in the wall static pressures in the inlet. Time histories of the pressure on the inlet ramp surface during the cowl rotations are shown in Figure 64. The tap locations correspond to those used in the experimental study along the inlet centerline and are shown in Figure 65. As the cowl rotates open, the pressures gradually increase as the shock train moves forward and strengthens. As the inlet unstart occurs, a significant and rapid increase in pressure is seen at all of the pressure tap locations on the inlet ramp. The peak pressures are nearly 50 times the freestream pressure at the peak. Once the shock train is pushed out of the inlet, the pressures drop and oscillate as the separation bubble and the supersonic jet oscillate. When the inlet is unstarted, the pressures are still higher than that when the inlet is started. As the inlet restarts, the pressures drop back to the initial values. In the following sections, the progression of the inlet from the started state to the unstarted state and from the unstarted state to the restarted state will be discussed in more detail, followed by a discussion of the hysteresis.

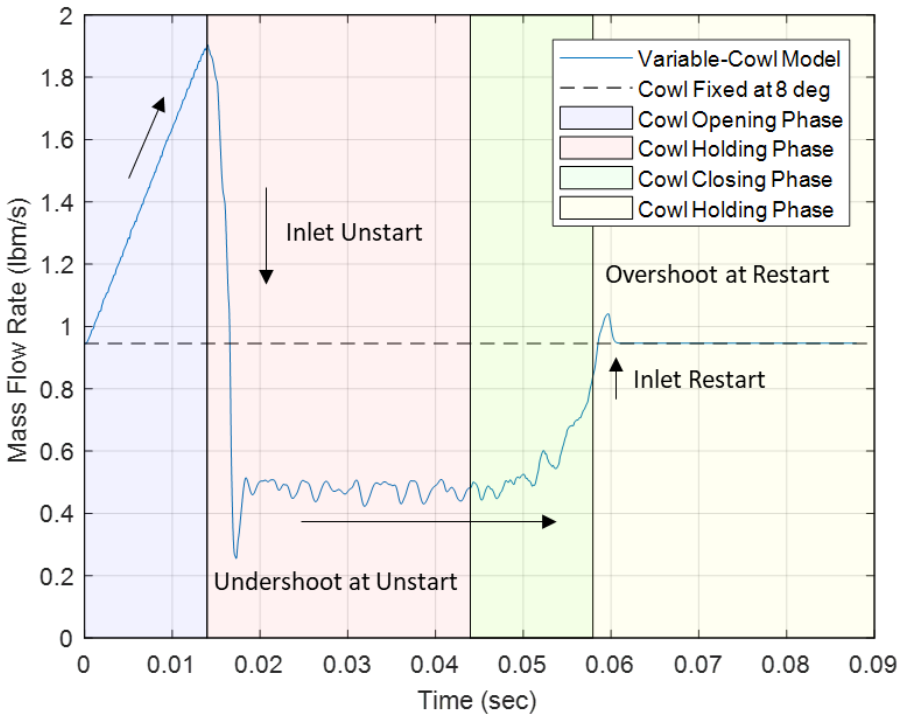

Figure 63: Time History of Mass Flow Rate Through the Inlet During the Rotation of the Cowl for the Baseline Computation

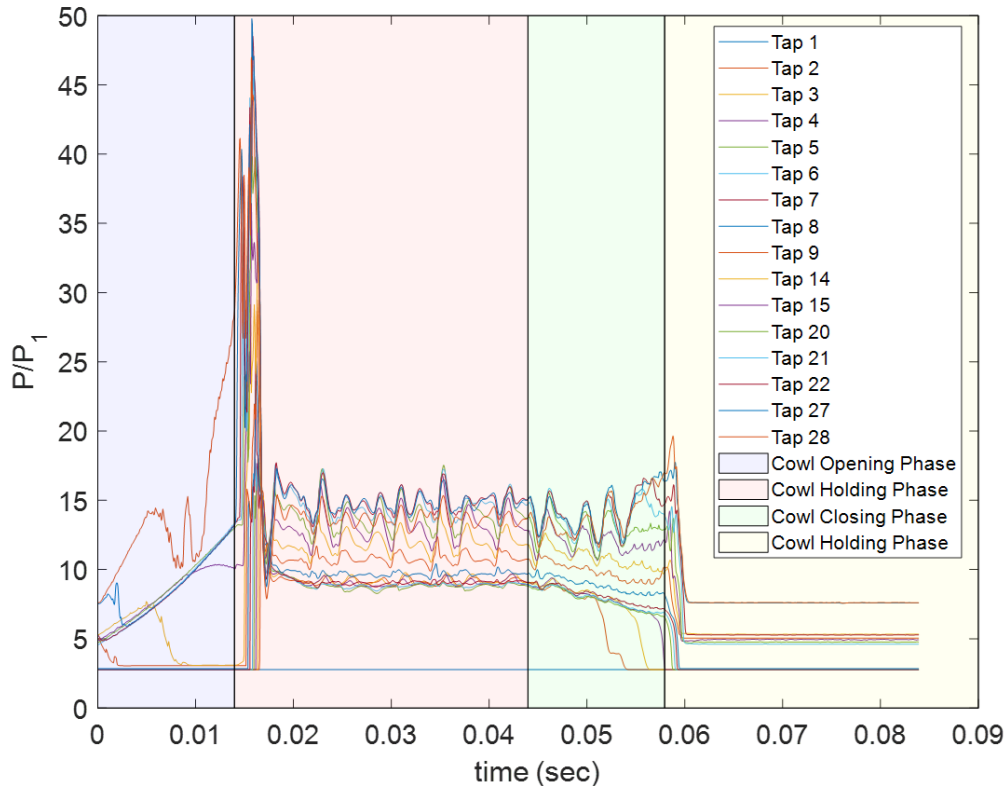

Figure 64: Pressure Time Histories during the Cowl Rotation in the Baseline Computation

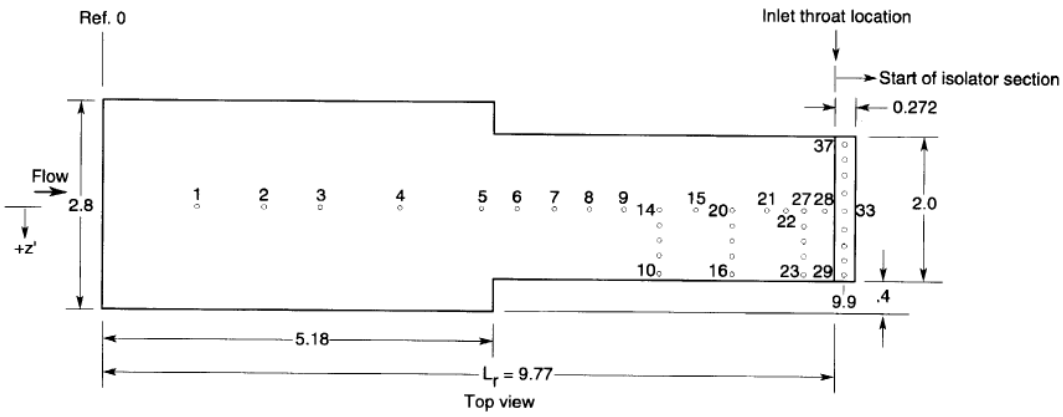

Figure 65: Pressure Tap Locations Shown in Figure 64 Corresponding to Experimental Tap Locations from Ref. [3]

Inlet Unstart

The cowl begins to rotate open at time t = 0 s. As can be seen in Figure 63, the mass flow rate initially increases as the inlet cowl is rotated open which increases the capture area of the inlet. However, at t = 0.01397 s, the inlet cowl reaches the horizontal position. The mass flow rate continues to increase slightly

even though the cowl has stopped opening, then at t = 0.01405 s, the mass flow rate peaks and drops off suddenly. This is the point of inlet unstart where the separated flow regions along the side walls have reduced the flow through area of the inlet, thus choking it. A time series of images showing the unstart process is also visible in Figure 66. The figure shows the same Mach number contours along the centerline plane as shown in Figure 62, but with a finer increment of 0.5 ms. At the 14 ms frame, the cowl is already in the horizontal position and is just before the peak mass flow rate is obtained. At 14.5 ms, a large separation bubble at the inlet shoulder is visible which is most likely the cause of the inlet unstart. As time continues, this separation bubble is seen moving upstream and growing in size. As the bubble passes through the inlet and grows, it creates a larger and larger flow constriction which increases the strength of the shock waves ahead of it and disrupts the shock train. In the 16.0 ms frame, it can be seen that the separation bubble has caused a “lambda shock” pattern spanning the height of the inlet. This is created by the separation bubble which has forced both the cowl shock and the separation shock to interact, leading to a nearly normal shock off the cowl leading edge. From 16.5 ms and on, all the shock waves have been pushed out of the inlet and a large separation shock sits ahead of the separation bubble, which blocks the flow from entering the inlet. The shock train is quickly and violently ejected from the inlet, and a large separation region forms at the entrance of the inlet, causing a severe blockage to the inlet capture area and thus leading to a significant reduction in the mass flow rate. This is also accompanied by the rapid increase in pressure in the inlet shown in Figure 67.

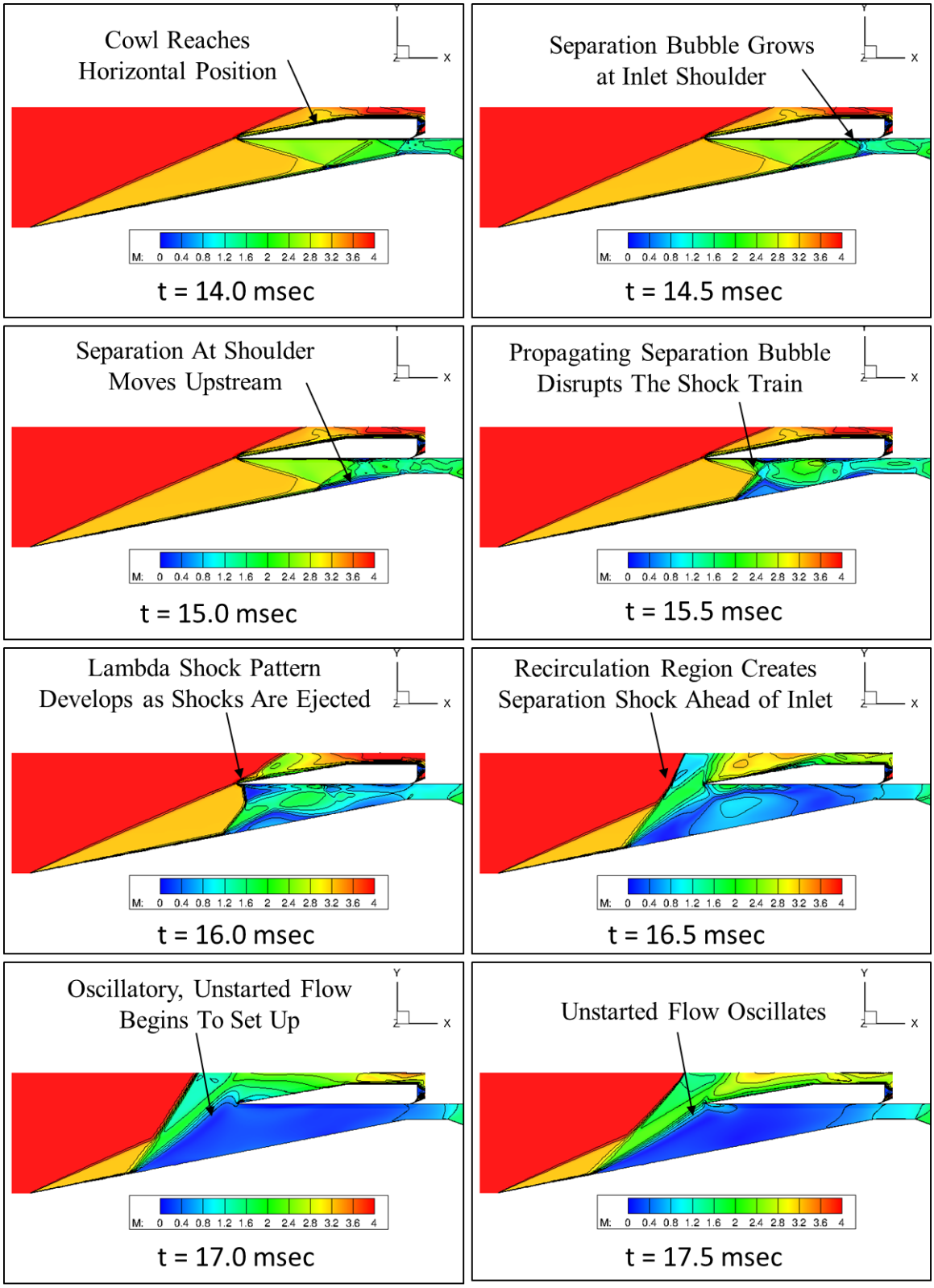

Figure 66: Centerline Mach Number Contours During Inlet Unstart

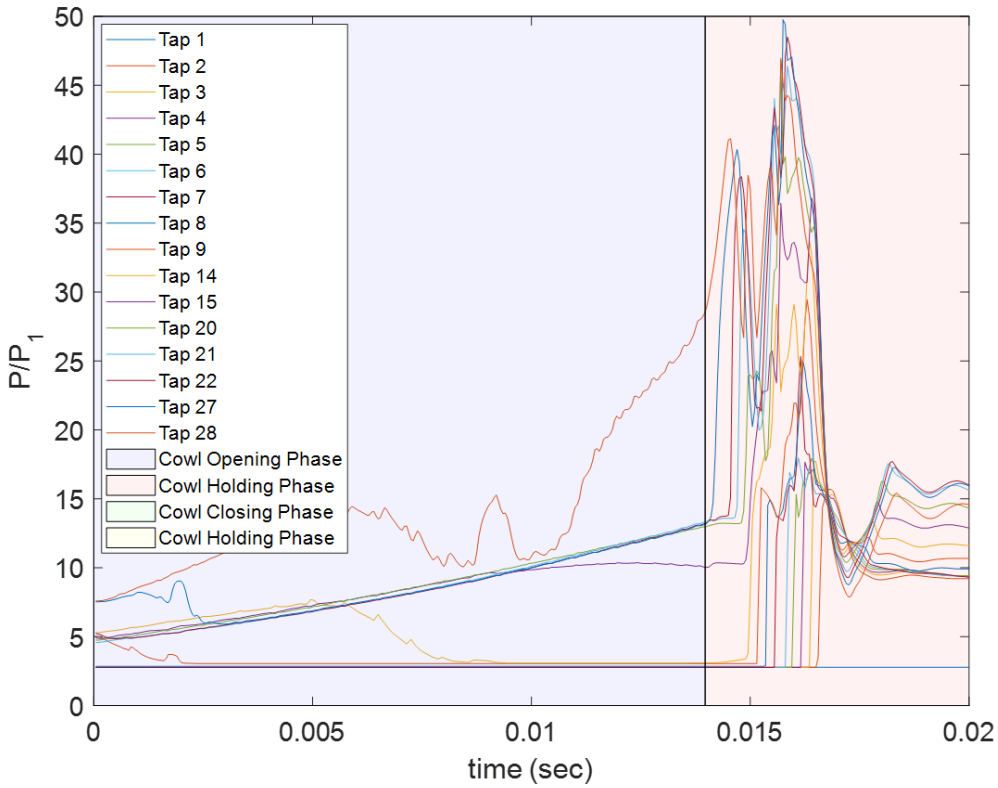

Figure 67: Normalized Wall Pressure Time Histories During Inlet Unstart

Inlet Restart

After the inlet unstarts, the cowl is held at the horizontal position for 30 ms during which the unstarted flow oscillates unsteadily. At time t = 0.04397 s, the cowl begins to close. As the cowl closes, the separation bubble is reduced in size because of the development of a favorable pressure gradient (evident in Figure 64 at around 50 ms), and the mass flow rate begins to increase as well. The restart process is shown visually in Figure 68. The size of the separation bubble can be seen decreasing in the frames at t = 53.0 ms to t = 58.0 ms. Also, as the cowl closes, the Mach number in the small supersonic jet that passes above the separation bubble on the cowl side increases. At 57.94 ms, the cowl has reached the 8 deg position and stops rotating. In the 58.0 ms frame, the separation shock ahead of the separation bubble can be seen to have reached the shock on lip position with the cowl. At this point, there is no spillage around the inlet and the separation bubble is sucked back into the inlet, as seen in the 59.0 ms frame. After 60.0 ms, the inlet has reached the started state again, and the mass flow rate returns to the steady state value.

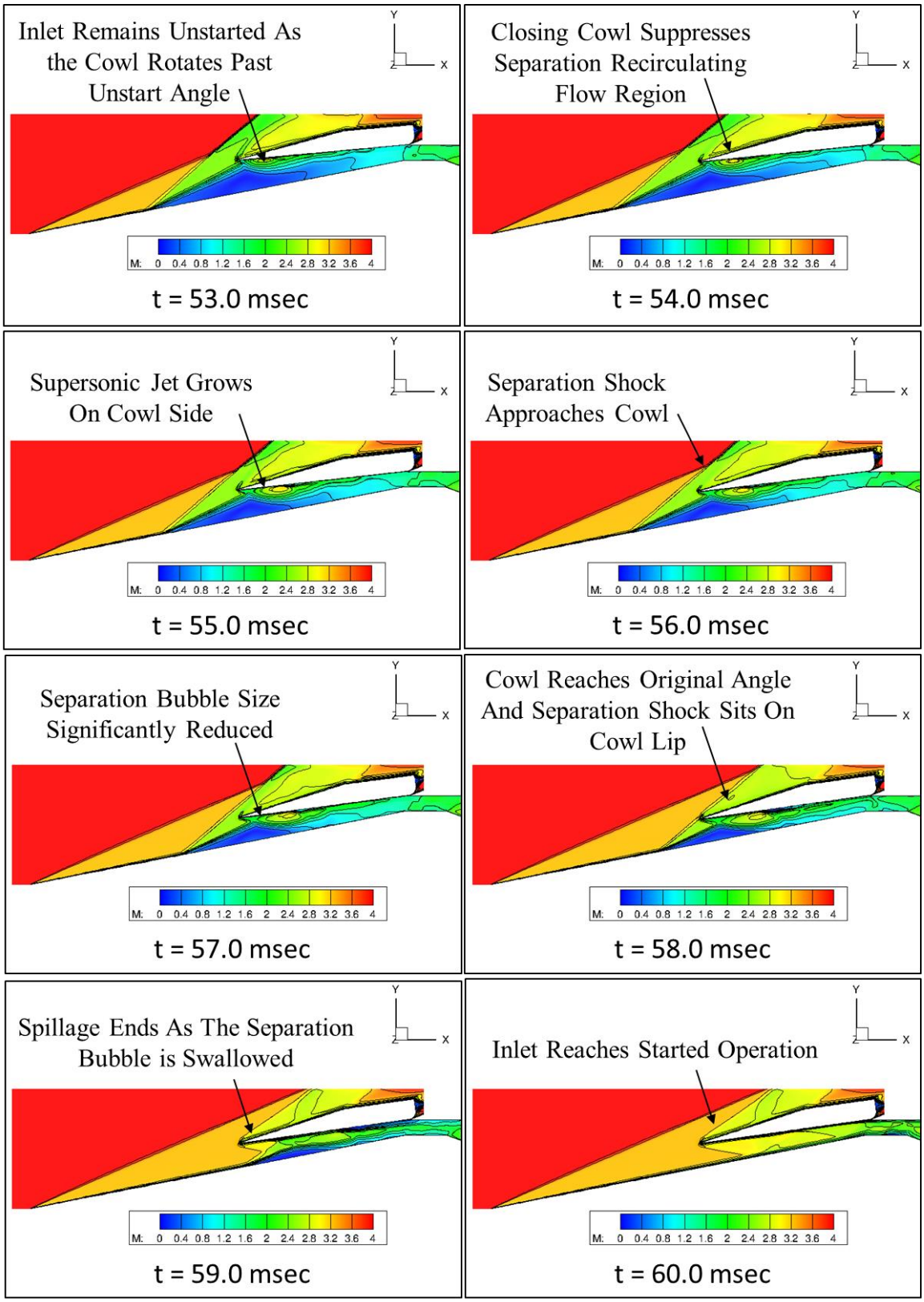

Figure 68: Centerline Mach Number Contours During Inlet Restart

Hysteresis

Hysteresis exists in this cowl rotation loop such that the inlet does not restart at the same point it unstarted. The inlet unstarted when the cowl was in the horizontal position, θ_c = 0 deg, but the inlet must be closed to back to θ_c = 8 deg before the favorable pressure gradient is large enough to reduce the separated flow regions and ingest the shock train. This hysteresis is illustrated in Figure 69 which shows the mass flow rate as a function of the cowl angle during the rotation loop. As the cowl angle is reduced (cowl opens), the mass flow rate increases until it unstarts when the cowl is in the horizontal position. As the cowl closes, the mass flow rate is not seen to begin to increase until the cowl has reached an angle of about 4 deg below the horizontal. The cowl stops rotating after it reaches the 8 deg position where the rotation started. There is a slight delay after the cowl reaches this position until the inlet restarts and the mass flow rate returns to the steady-state started value. It is interesting to note that in both Figure 63 and Figure 69, there is an undershoot and overshoot visible in the mass flow rate as the inlet unstarts and then restarts. This phenomenon is likely associated with the viscous separated flows and a required time delay until the separation bubbles are fully formed and positioned.

Figure 69 also includes individual data points obtained from the steady Fixed-Cowl Model at the three cowl angles discussed previously. The agreement between the two models is good. It is important to note, however, that the Fixed-Cowl Model, using uniform initial conditions, is incapable of predicting the lower branch of the mass flow rate curve caused by the hysteresis during the restart process. This inherently requires a transient computation marching forward in time from the unstarted solution to properly account for the hysteresis that exists. This is a significant finding and clearly illustrates the need for including the time-dependent analysis in inlet performances analyses during the unstart and restart phases of an inlet.

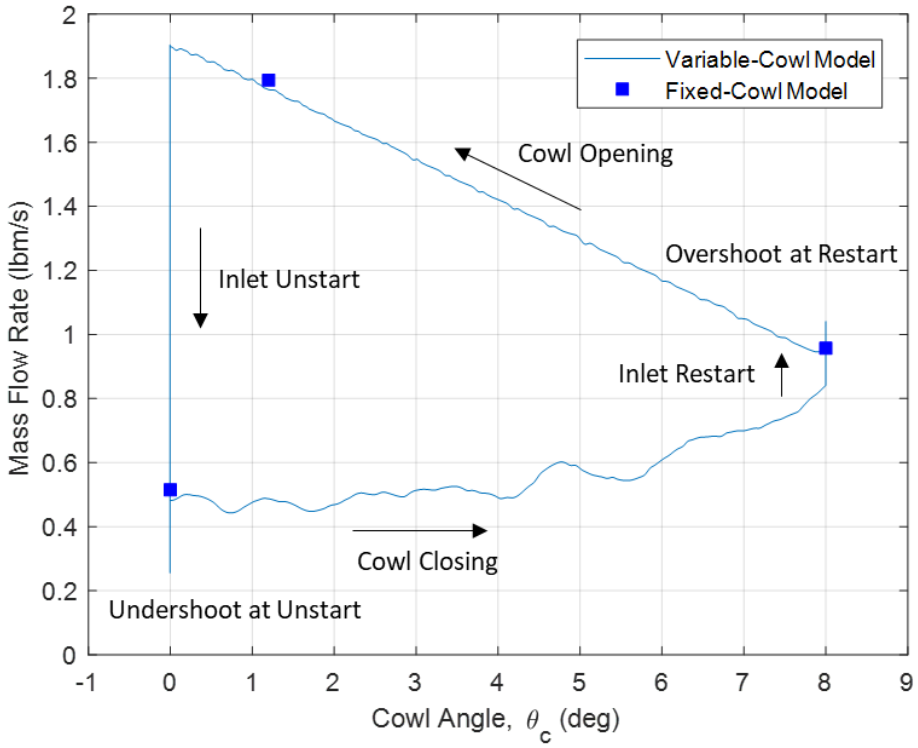

Figure 69: Mass Flow Rate Through the Inlet During the Rotation of the Cowl Plotted as a Function of Cowl Angle for the Baseline Computation

7.2.3 The Impact of Corner Flows and Separation on the Unstart Process

As mentioned in Section 2.2.2, the three-dimensionality of the flow field plays a large role on the dynamics of the inlet unstart mechanism. In particular, the presence of corner flows and their role in creating spanwise flows has already been noted in Section 7.1.1 using the Fixed-Cowl Model. This section, however, will highlight the evolution of the corner flows and separation bubbles and will show the role they play in the inlet unstart dynamics. To begin with, Figure 70 shows an x-t diagram of the logarithm of the wall pressure ratio, indicating the motion of the shock waves and other high-pressure bands along the centerline of the inlet. As the cowl rotates open with time, it is seen that the shock waves along the centerline move aft based purely on the geometry of the wave angles. At about t = 0.015 s, the waves change direction and move forward at a high velocity, indicated by the steep slope in the diagram. This is showing the shock train moving forward and eventually out of the inlet where the separation shock sets up in the unstarted flow. The restart process again is hindered by hysteresis. The waves move back into the

inlet and are eventually swallowed, but the restart process requires much more time than the unstart process.

The first indication of the influence of corner flows on the unstart process is shown in Figure 71, which plots the same x-t diagram along a line at the spanwise coordinate of z/H_{th} = 2.25. This spanwise location is 0.1 inches off the sidewall. This line is, therefore, nearly in the sidewall boundary layer. By comparing Figure 70 and Figure 71, important differences can be seen. As the cowl rotates open initially, it is seen that the high-pressure lines between x/H_{th} = 18 and x/H_{th} = 27 move forward almost immediately along the sidewall, as opposed to those along the centerline which moved aft. This is the development of the corner flow shocks and separation region that was shown to influence the centerline shock-boundary layer interaction and to create the spanwise flow inward toward the centerline. This result hints at the fact that the inlet unstart may be initiated by the growth of the corner flow separation regions.

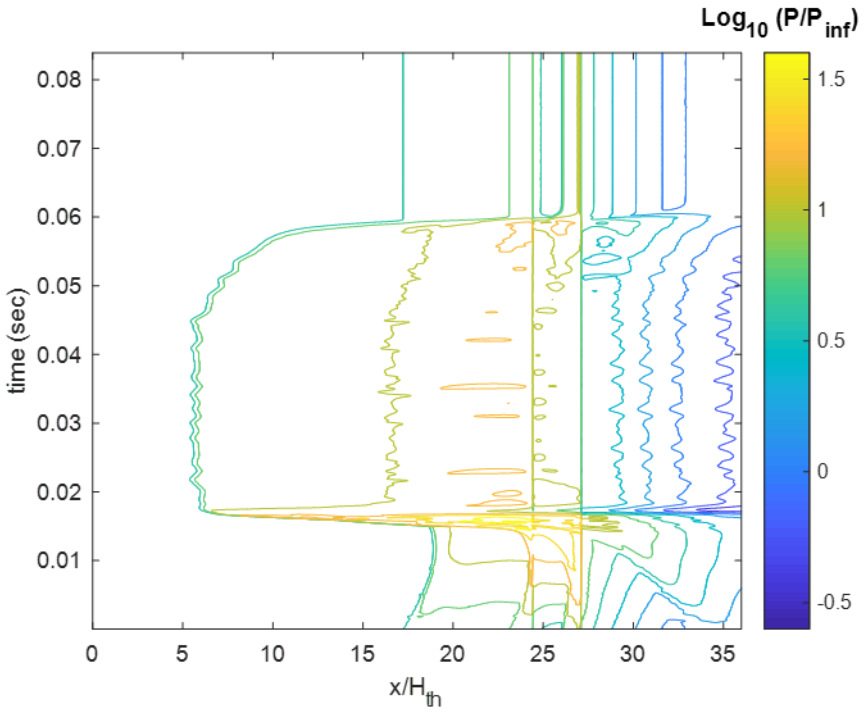

Figure 70: x-t Wall Pressure Diagram Along the Centerline of the Inlet

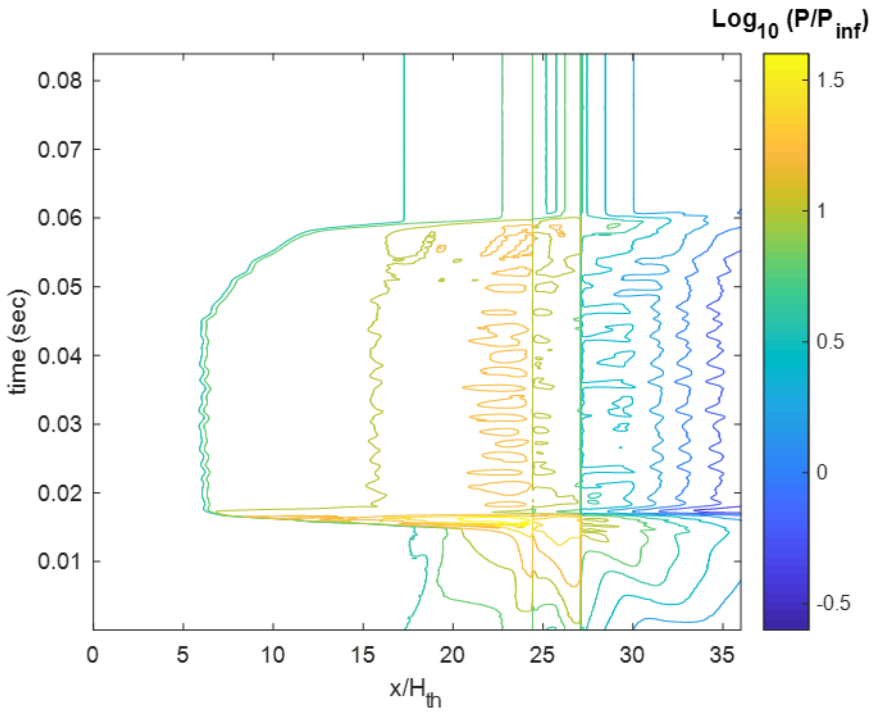

Figure 71: x-t Wall Pressure Diagram Along a Line at Z = 0.9 inches (0.1 inch off the Side Wall)

Additionally, the impact of the corner flows can be seen in Figure 72 which shows Mach number contours on surfaces that are 0.1 inches above the inlet ramp, isolator and diffuser sections. Again, these surfaces are close to the edge of the boundary layer. In the first frame, at t = 13.0 ms, the cowl is at 0.55 deg below the horizontal, which is just prior to the inlet unstarting (which occurs at the horizontal position). The strong shock-boundary layer interaction due to the cowl shock impinging on the inlet ramp is visible. Also, a short distance behind this interaction a small region of low speed flow is visible along the sidewalls. This is the corner flow separation bubble. There also exists a similar separation bubble father aft at the shoulder of the inlet ramp and transition to the isolator section. This second separation bubble grows in the next two frames. At 14.0 ms, the inlet state is just prior to the point of maximum mass flow rate which occurs at 14.05 ms. In the following frames, these separation bubbles begin to move forward as the inlet begins to unstart. As they progress down the inlet, they grow in size and they create an even larger region of separated flow that now extends into the centerline of the inlet. At 16.0 ms, a pair of counter-rotating vortices is evident in the flow. At 16.5 ms, the inlet is completely unstarted.

To further show the impact of the corner flows on the centerline flow, the same time intervals are shown in Figure 73, but now, axial cuts through the duct with a single centerline cut are shown with Mach number contours. The evolution of the separation bubbles is visible. They begin along the sidewalls but grow into the center of the inlet as seen in the frame at 14.5 ms. At 15.0 ms, there are similar separation bubbles growing on the underside of the cowl. The forward motion of the separation bubbles during the unstart is again evident.

To highlight the vortical features, Figure 74 shows the same cut planes as in Figure 76 with contours of magnitude of vorticity. Vorticity is defined as twice the angular velocity of a fluid element. Mathematically this is $\boldsymbol{\Omega} = \boldsymbol{\nabla} \times \mathbf{V}$ [58]. Other than in the boundary layer, regions of high vorticity can be seen in the corner regions where the inlet ramp and sidewalls meet. These corner vortices grow in size as the inlet cowl is opened and the separation regions grow. At 15 ms, the vortical features extend nearly the full height of the isolator and then begin to propagate upstream as the inlet unstarts. As they move forward, they grow in size and extend across the full span of the duct. Once the inlet is unstarted, a large vortical flow field is set up ahead of the inlet.

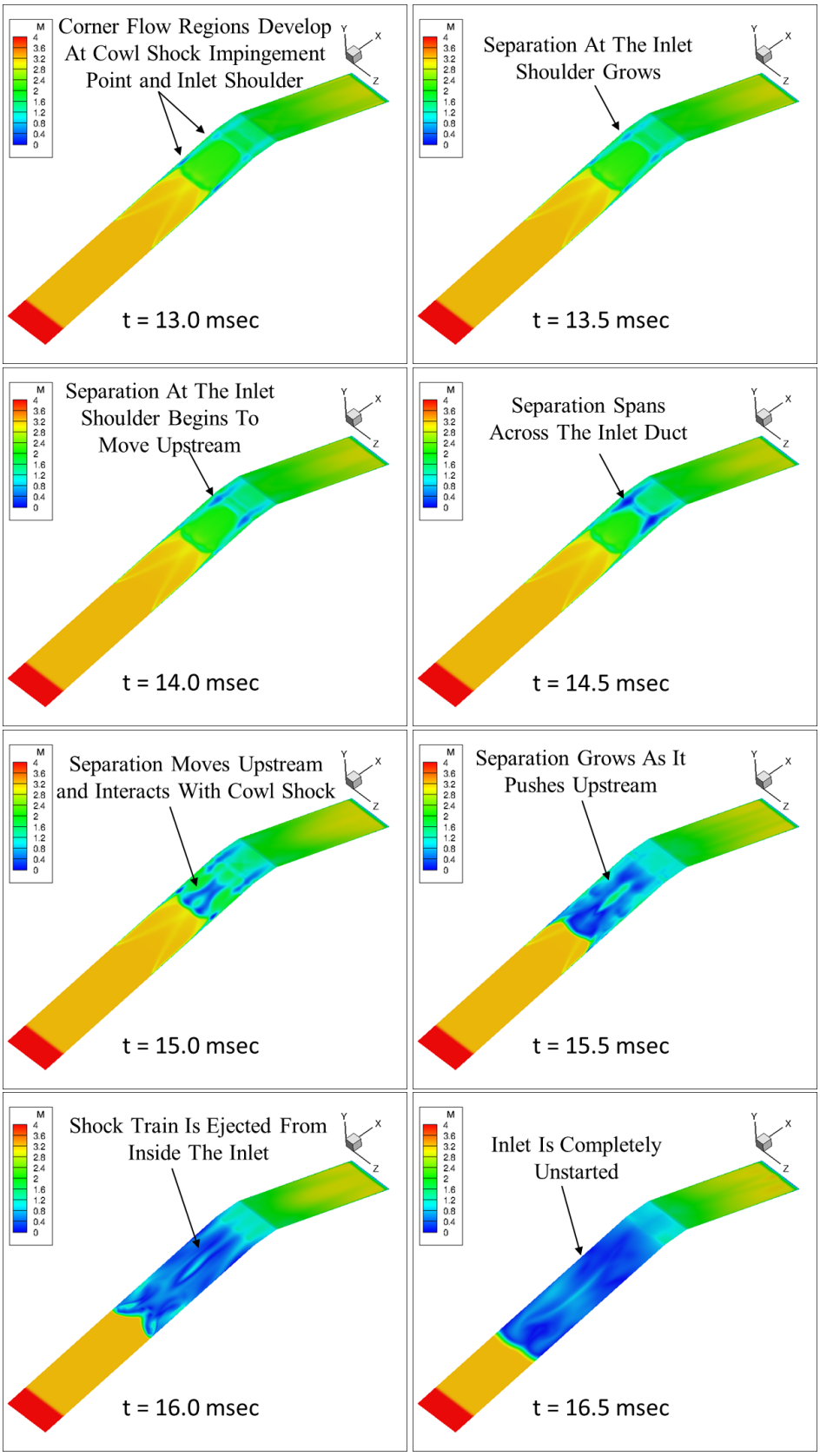

Figure 72: Time Histories of Mach Number Contours along a Plane 0.1 inches Above Body Side Ramps

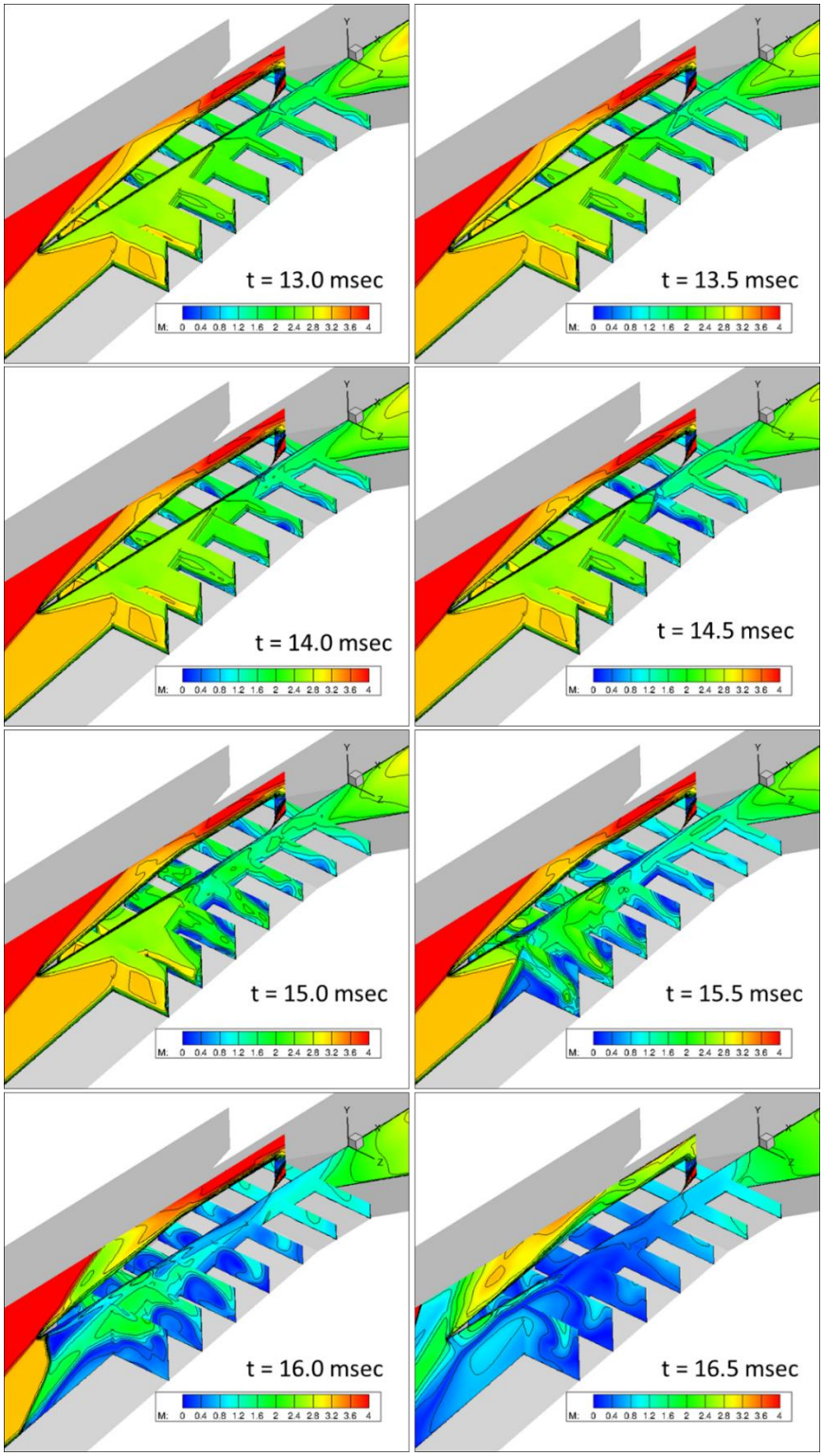

Figure 73: Time Histories of Mach Number Contours along Axial and Centerline Cuts
(See Figure 72 For Annotations)

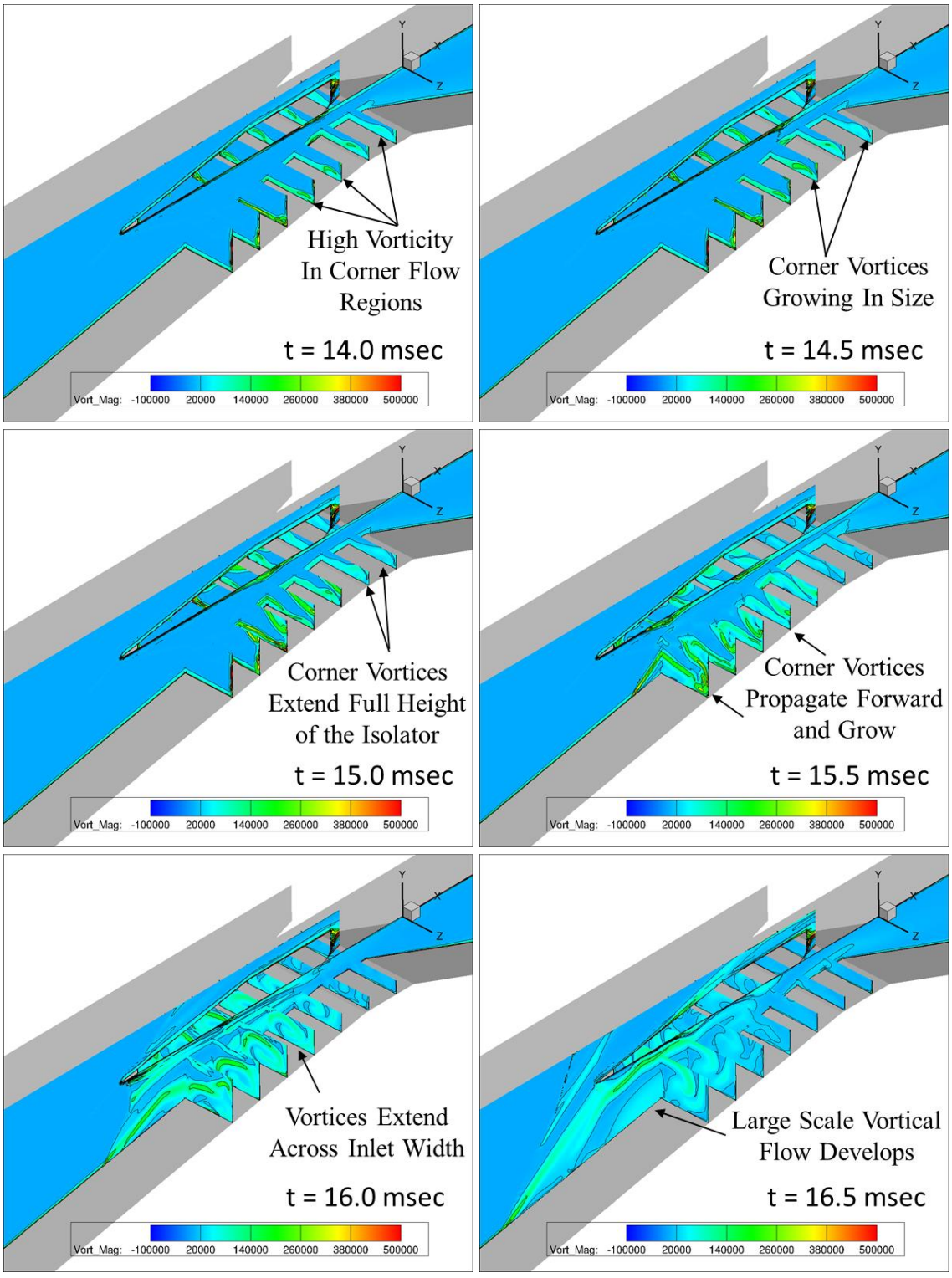

Figure 74: Time Histories of Vorticity Contours along Axial and Centerline Cuts

Finally, Figure 75 and Figure 76 show simulated oil flow lines along the inlet ramp and sidewall during the cowl rotation phase up the point just prior to unstart and then through the unstart, respectively. First, Figure 75 shows a series of frames not at regular intervals but at significant points in the development of the separation bubbles to highlight the development of the bubbles. When the cowl is at a large angle below the horizontal as in the first frame, no separation bubble or spanwise flow is seen along the inlet ramp. The only separation exists in the isolator section. As the cowl opens and the shock-boundary layer interaction due to the cowl shock gets stronger, spanwise flows from the corners of the sidewalls and inlet ramp develop as seen in the second frame at 5 ms. Due to motion of the shock train, the separation bubble in the isolator eventually breaks up, and significant streamline curvature at the inlet shoulder develops as the reflected shock becomes positioned at the shoulder. This is seen in the frame at 6.5 ms. Next, separation bubbles begin at the cowl shock impingement point and at the shoulder as a pair on either side of the centerline and eventually merge as seen at 8.5 and 9.2 ms. Then, prior to unstart, the separation bubble at the cowl shock impingement point grows and additional vortices develop at the should as more spanwise flow is pulled into the separation bubble and accompanying vortices.

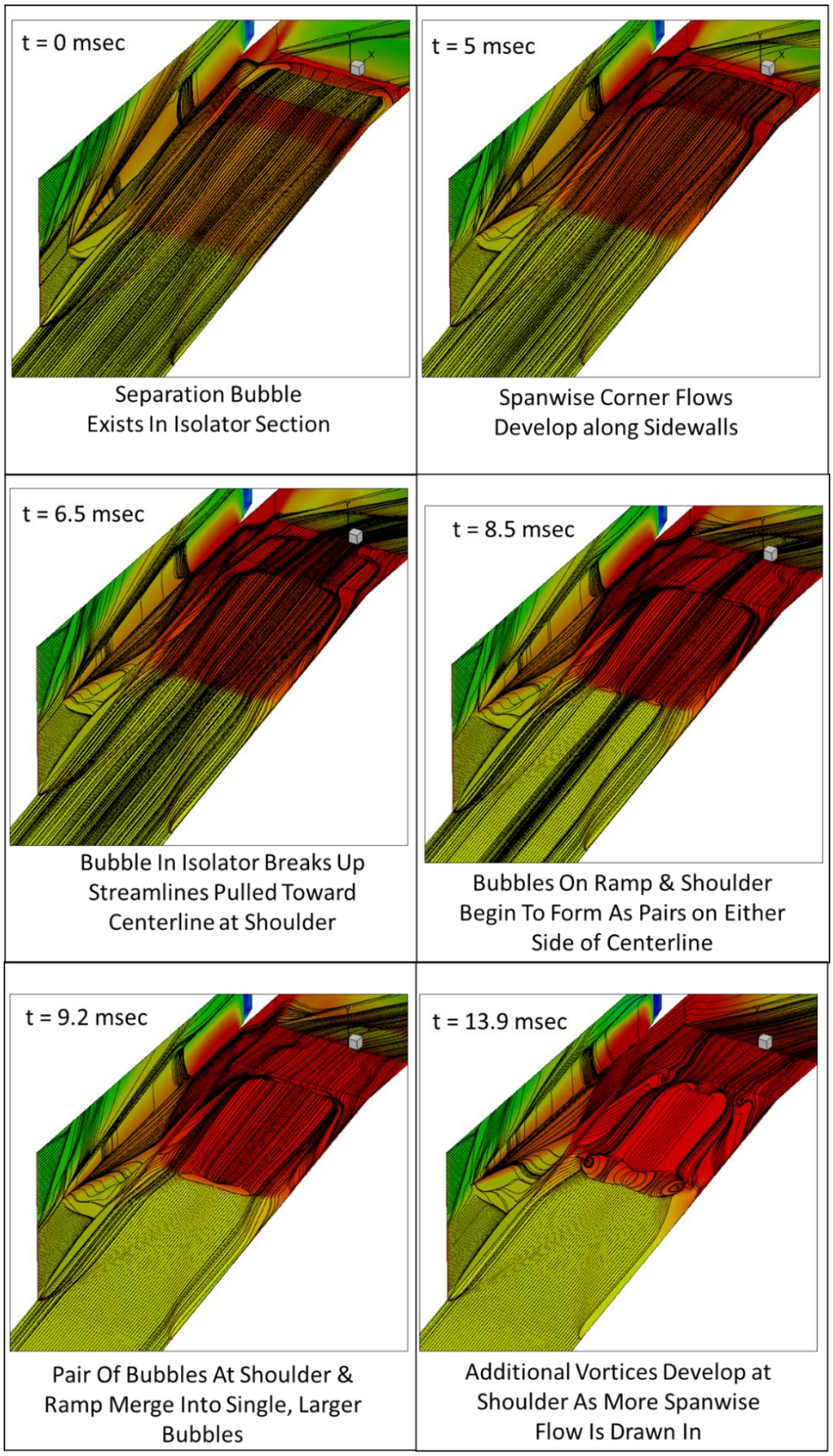

Figure 75: Oil Flow Lines on the Inlet Ramp and Sidewalls During the Cowl Rotation Highlighting the Development of the Separation Bubbles

Second, Figure 76, shows oil flows at 5 ms intervals during the unstart process to highlight the motion of the bubbles and vortices. This time series begins at 12.0 ms when the inlet cowl is positioned at 1.12 deg below the horizontal. Note the spanwise flows that exist prior to the main shock-boundary layer interaction at the cowl shock impingement point. This spanwise flow is drawn into two foci at the center of counter-rotating vortices inside the separation bubble. Behind this, a second separation bubble sits at the inlet shoulder as discussed previously and shown in Figure 72. It is important to note that the spanwise flow from the sidewalls is also drawn into this second separation bubble from the sidewalls. As time proceeds and the cowl opens, the separation bubbles grow. In the frames from 12.0 ms to 13.0 ms, there does not appear to be a pair of counter-rotating vortices in the separation at the shoulder as in the first separation bubble at the cowl shock impingement point. The flow instead enters the shoulder separation bubble and reaches a focus at the inlet centerline. However, in the 13.5 and 14.0 ms frames, the separation bubble grows as the shock interaction gets stronger and a vortex develops on either side of the focus. At 14.0 ms, again just prior to the inlet unstarting, the vortices have grown significantly and are now drawing the flow in from both the centerline and the sidewalls into the vortices. This is a change from the frames up to about 13.0 ms which only showed spanwise flow into the centerline separation bubble. Again, as the inlet unstarts, the vortices are drawing fluid away from the centerline and sidewalls. At this point, the counter-rotating vortices move upstream and progress out of the inlet. The two vortices that began at the shoulder merge with the vortices in the first separation bubble and expand significantly. At 16.0 ms, the separation shock has pushed ahead of the inlet sidewalls and has exited the inlet.

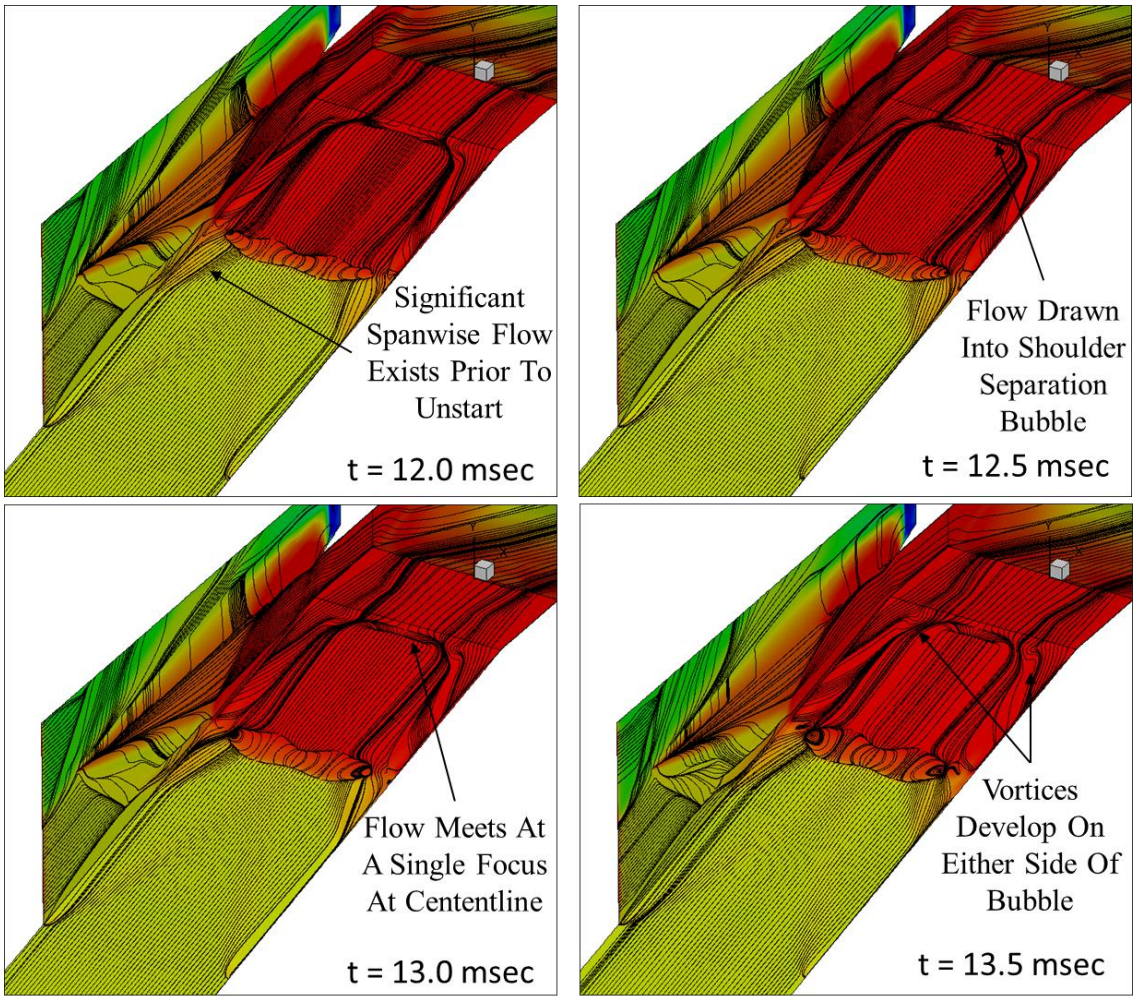

Figure 76: Simulated Oil Flow Lines on the Inlet Ramp and Sidewalls During the Unstart Process Highlighting the Motion of the Separation Bubbles

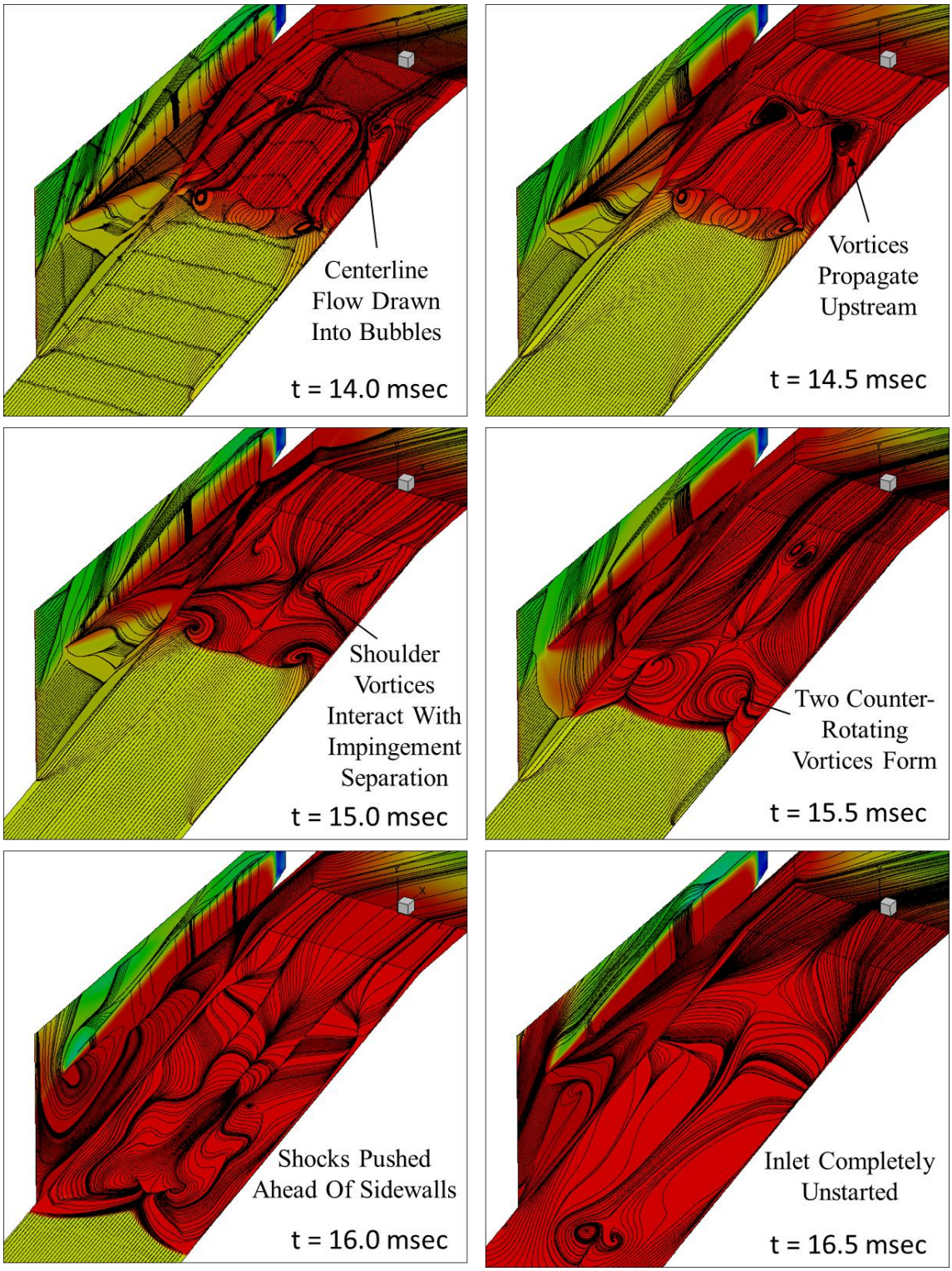

Figure 76 (Continued): Simulated Oil Flow Lines on the Inlet Ramp and Sidewalls During the Unstart Process Highlighting the Motion of the Separation Bubbles

7.2.4 The Effect of Cowl Rotation Rate

The effect of how fast the cowl is rotated on the physics just described was assessed by computing the same cowl motions (rotate open, hold, and rotate close) using two additional rotation rates, 5 rad/s and 1 rad/s. It should be noted that the cowl was held in the horizontal position after the unstart for the same duration in all cases, that is 30 ms. Time histories of the mass flow rates through the inlet for the three different rotation rates can be seen in Figure 77. The trends are all similar; the mass flow rates increase linearly with time as the cowl angle is opened and then drop off steeply after reaching a peak as the inlet unstarts. A period of unsteady fluctuation follows and then the mass flow rate slowly increases as the inlet begins to restart. It is interesting to note that the peak mass flow rates are slightly different for the different cowl rotation rates. The peak mass flow rate increases as the cowl rotation rate increases as shown in Table 14. Also, the cowl angle at which the peak mass flow rate was reached decreased as the rotation rate increased. At the 1 rad/s rate, the peak mass flow rate was reached when the cowl was about half a degree below the horizontal whereas the 10 rad/s reached this peak after the cowl had reached the horizontal position. This can be seen visually in Figure 78 and is tabulated in Table 15. The restart dynamics are also slightly different. In particular, the slowest rotation rate, 1 rad/s, shows much larger fluctuations and seems to almost restart at about t = 0.29 s. These large fluctuations in mass flow rate are due to significant motion of the supersonic jet that forms on the underside of the cowl. This is shown in Figure 78 which depicts the centerline Mach number contours at θ_c = 6.9 deg from the computations with the baseline cowl rotation rate and the slow cowl rotation rate. The 6.9 deg position corresponds approximately to the spike in mass flow rate at 0.29 seconds for the slow rotation rate shown in Figure 77. After the restart, all rotation rates tend to the same steady-state value of the mass flow rate. In addition, each case shows similar undershoots and overshoots in mass flow rate as the inlet is unstarted and restarted.

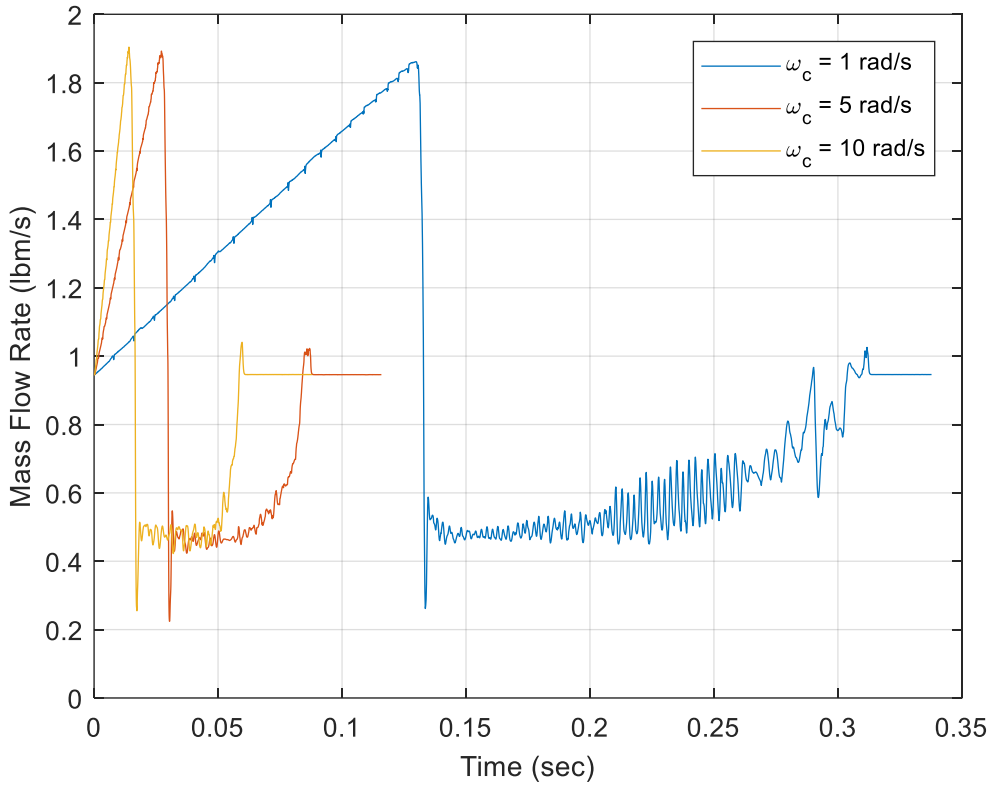

Figure 77: Time Histories of Mass Flow Rate Through the Inlet for Different Cowl Rotation Rates

Table 14: Peak Mass Flow Rates Prior to Inlet Unstart for Different Cowl Rotation Rates

Rotation Rate (rad/s)	**Peak Mass Flow Rate (lbm/s)**
1 rad/s	1.8614
5 rad/s	1.8923
10 rad/s	1.9039

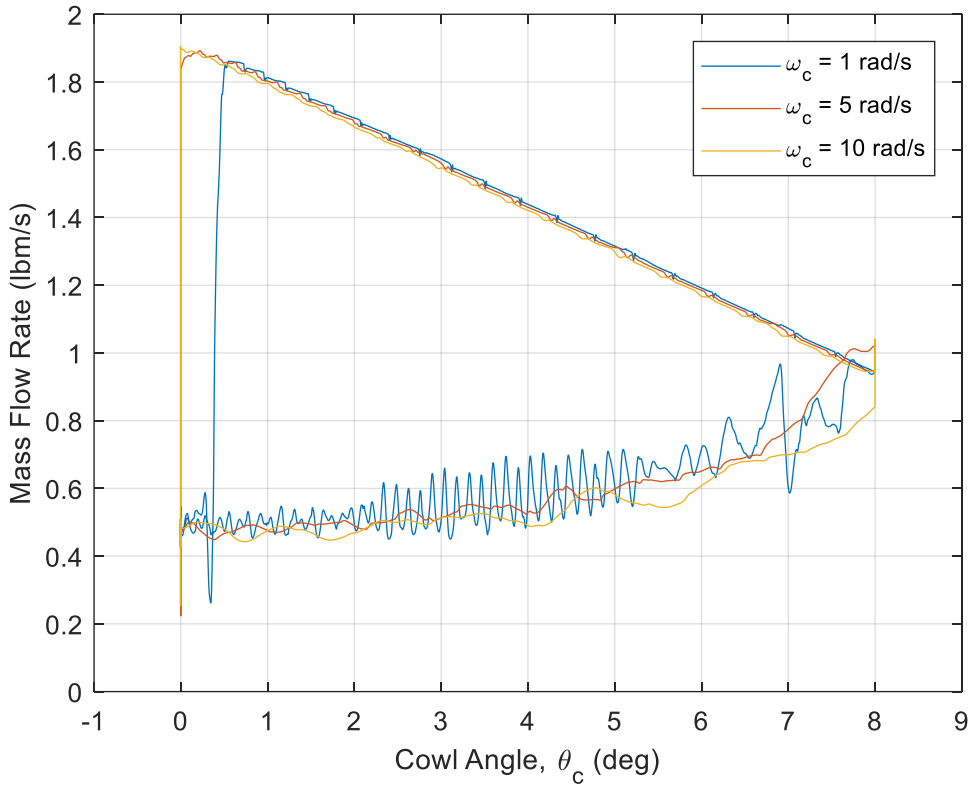

Figure 78: Mass Flow Rate Through the Inlet During the Rotation of the Cowl Plotted as a Function of Cowl Angle for Different Cowl Rotation Rates

Table 15: Cowl Angle Corresponding to Peak Mass Flow Rate Prior to Inlet Unstart for Different Cowl Rotation Rates

Rotation Rate (rad/s)	**Cowl Angle from Horiz., θ_c (deg)**
1 rad/s	0.56
5 rad/s	0.22
10 rad/s	0.00

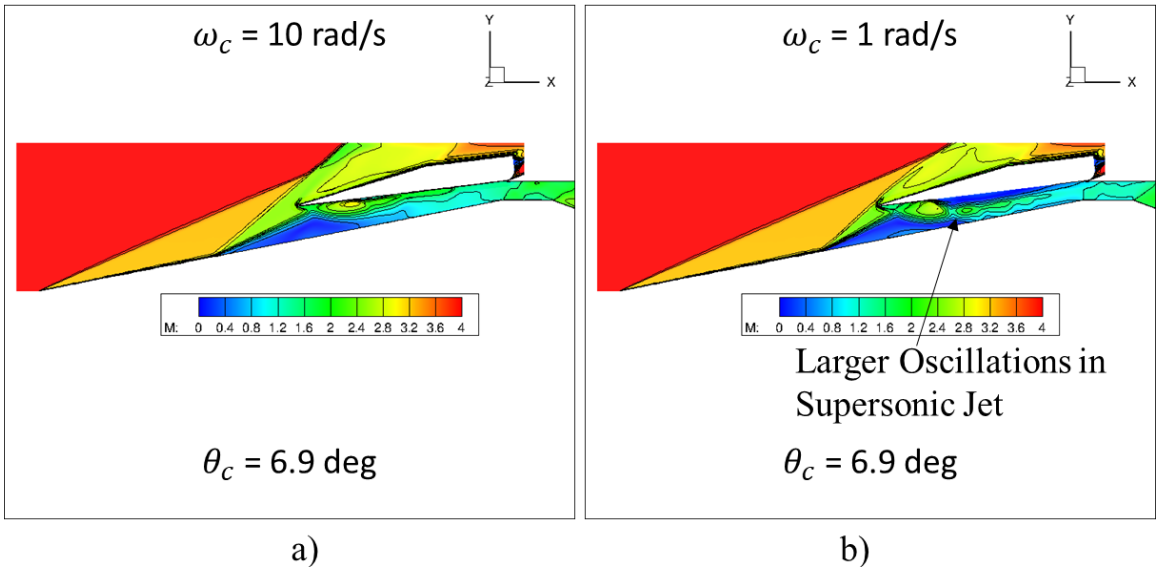

Figure 79: Centerline Mach Number Contours at θ_c = 6.9 deg Computed with a) the Baseline Rotation Rate of 10 rad/s and b) the Slow Rotation Rate of 1 rad/s

7.2.5 Unsteady Two-Dimensional Results

As was done with the Fixed-Cowl Model, a set of two-dimensional cases was conducted for the Variable-Cowl Model as well. The reason for conducting these two-dimensional cases was to highlight the effect of three-dimensional flows on the inlet. The motion of the cowls were the same and the same three rotation rates discussed in the previous section were analyzed. Significant differences were found between the two-dimensional and three-dimensional models. Most importantly, the two-dimensional results do not show the inlet unstarting when the cowl is at the horizontal position. This is in contrast to the three-dimensional model as well as the experimental data. The reason for this is that by applying the two-dimensional model inherently assumes an infinitely wide duct and therefore neglects the effects of the corner flows discussed in Section. 7.2.3. As the cowl rotates open, a separation bubble at the point of the cowl shock impingement point grows as seen in the below Figure 81 which shows the evolution of the centerline flow for both the two- and three-dimensional models. This is similar to what is seen at the centerline of the three-dimensional results. However, the size of this bubble does not reach that obtained in the three-dimensional results because it cannot feed off the spanwise flow initiated at the ramp and sidewall corners. The same can be said about the separation bubble at the shoulder of the inlet. Because the computation does not account for spanwise flows, the growth of the additional two vortices on either side of the centerline prior to unstart

noted in Figure 75 and Figure 76 are not accounted for. This is illustrated in more detail in Figure 82 which shows the same contours as in Figure 81 but at the 14 ms time step, which is just prior to the point of maximum mass flow rate prior to unstart in the three-dimensional model. Again, this highlights the high three-dimensionality of the inlet unstart process.

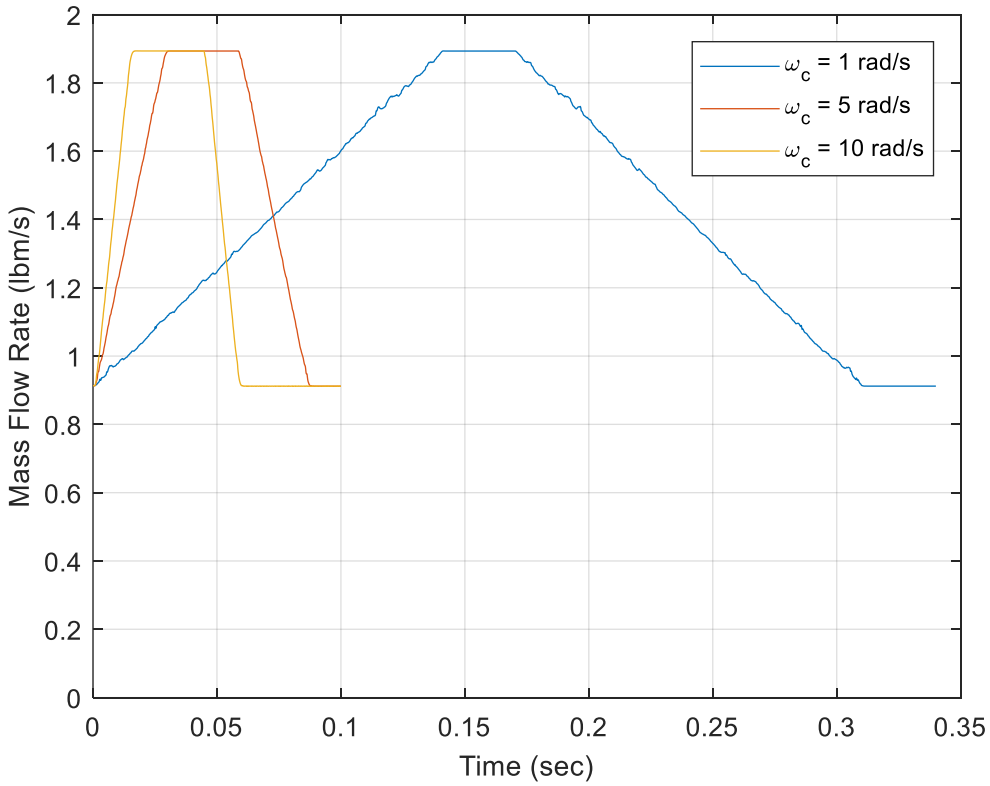

Figure 80: Time Histories of Mass Flow Rate Through the Inlet for Different Cowl Rotation Rates Obtained Using the Two-Dimensional Model

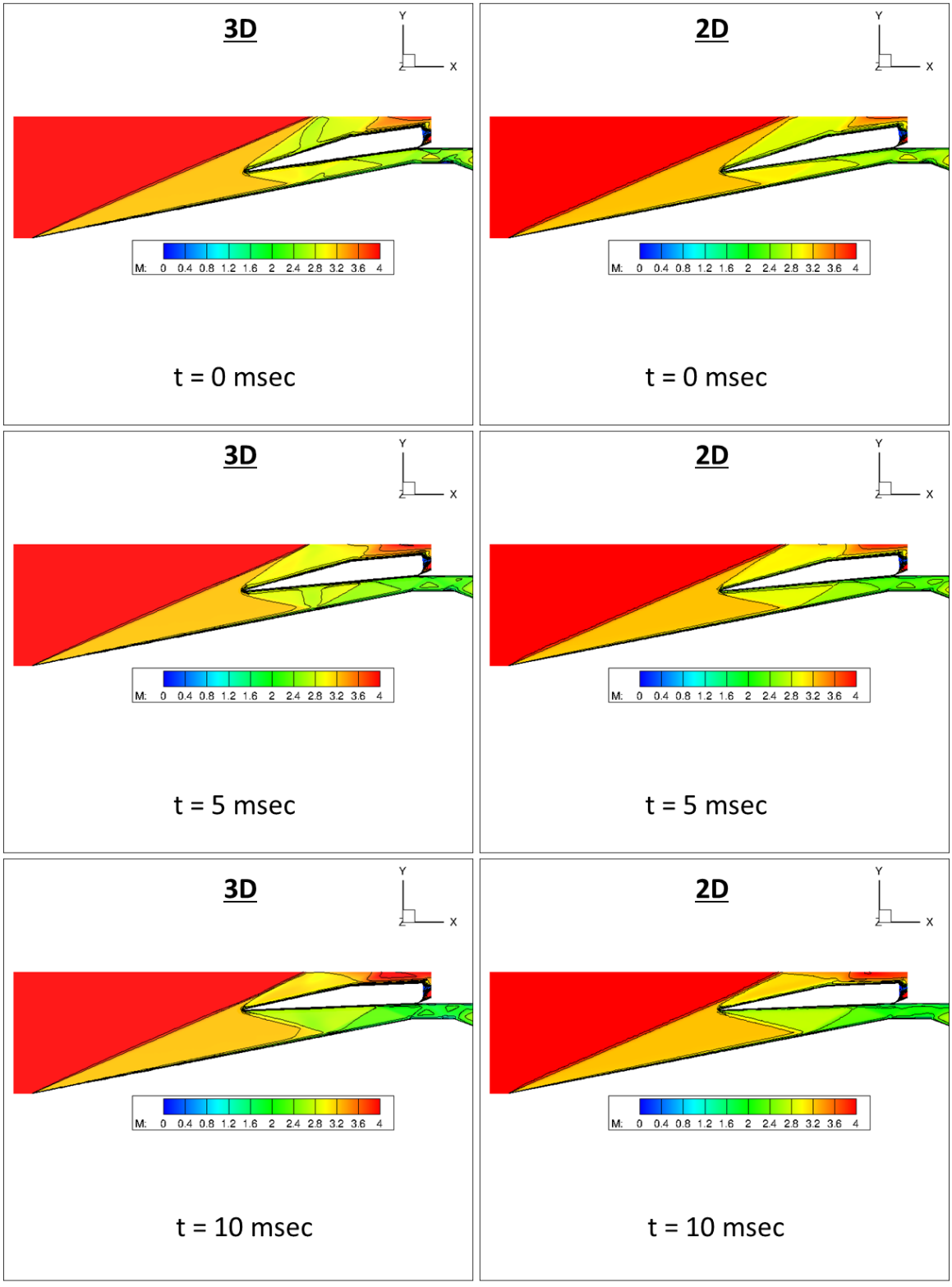

Figure 81: Centerline Mach Number Contours During Cowl Opening for the a) 3D and b) 2D Models

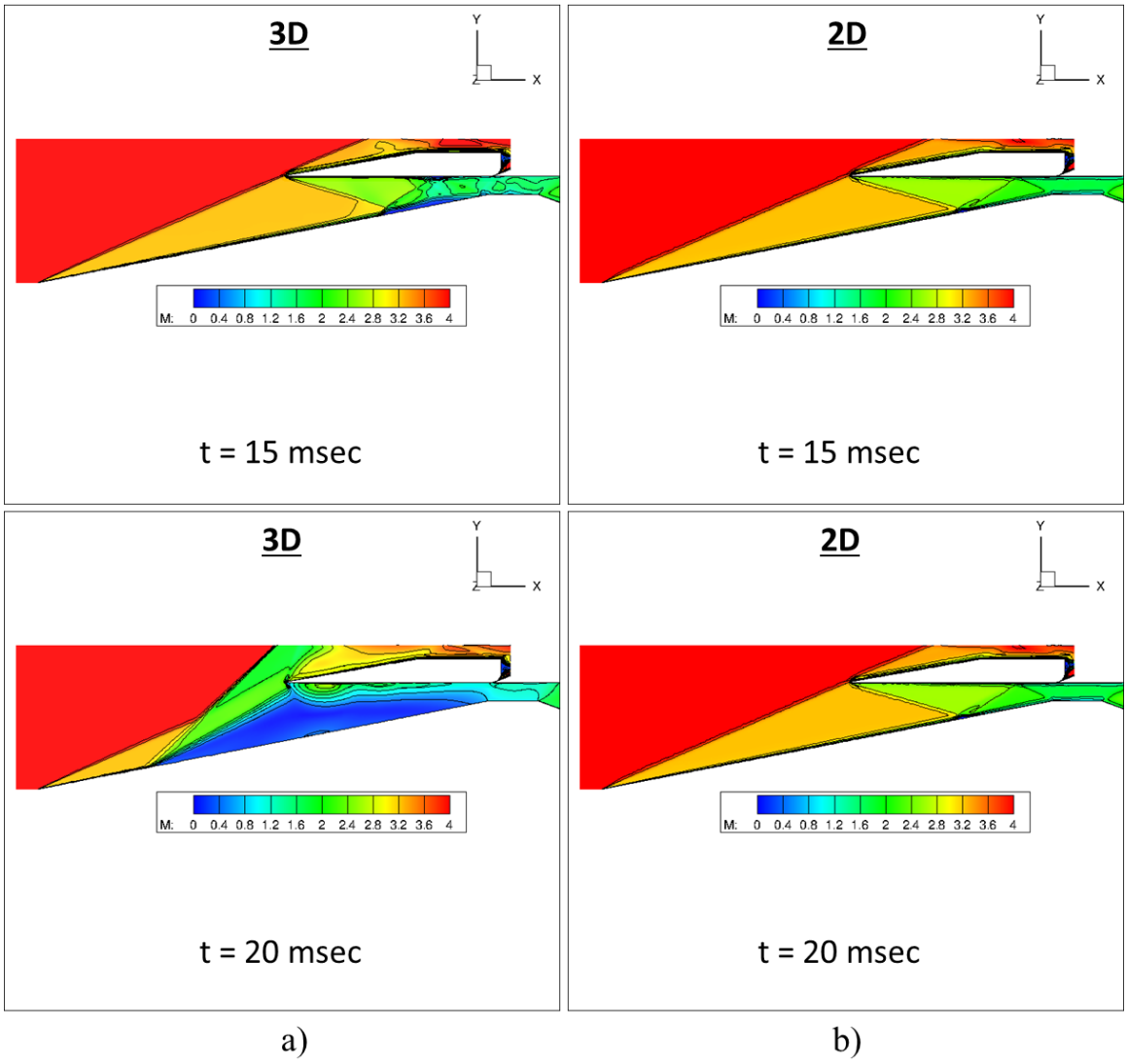

Figure 81 (Continued): Centerline Mach Number Contours During Cowl Opening for the a) 3D and b) 2D Models

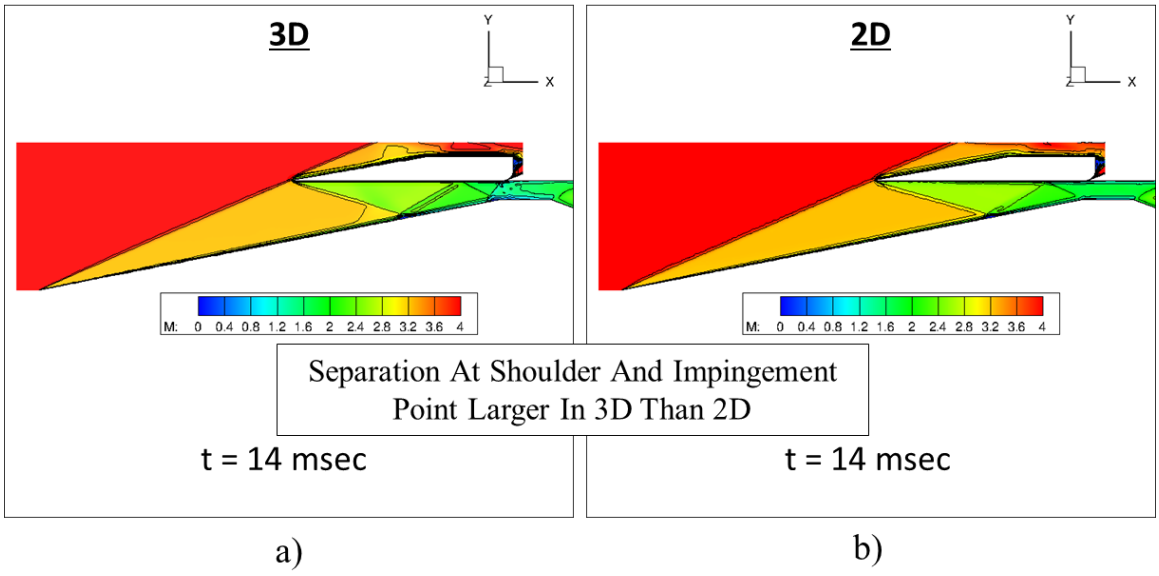

Figure 82: Centerline Mach Number Contours for the a) 3D and b) 2D Models at 14 msec

Interestingly, there is a different type of hysteresis present in the 2D results even though the inlet does not unstart. This can be seen in Figure 83 which shows the mass flow rate through the inlet as a function of the cowl angle below the horizontal, θ_c. The motion begins at the 8 deg position and progresses on the lower curve as the inlet opens. After the cowl reaches the horizontal position, the mass flow rate continues to increase slightly before leveling off. Then, as the cowl closes, the mass flow rate decreases along the upper curve due to the hysteresis until the cowl reaches the 8 deg position again. The hysteresis is most likely due to a change in the computed boundary layer thickness and displacement thickness as the cowl is closed and the separation bubble is reduced and then eliminated.

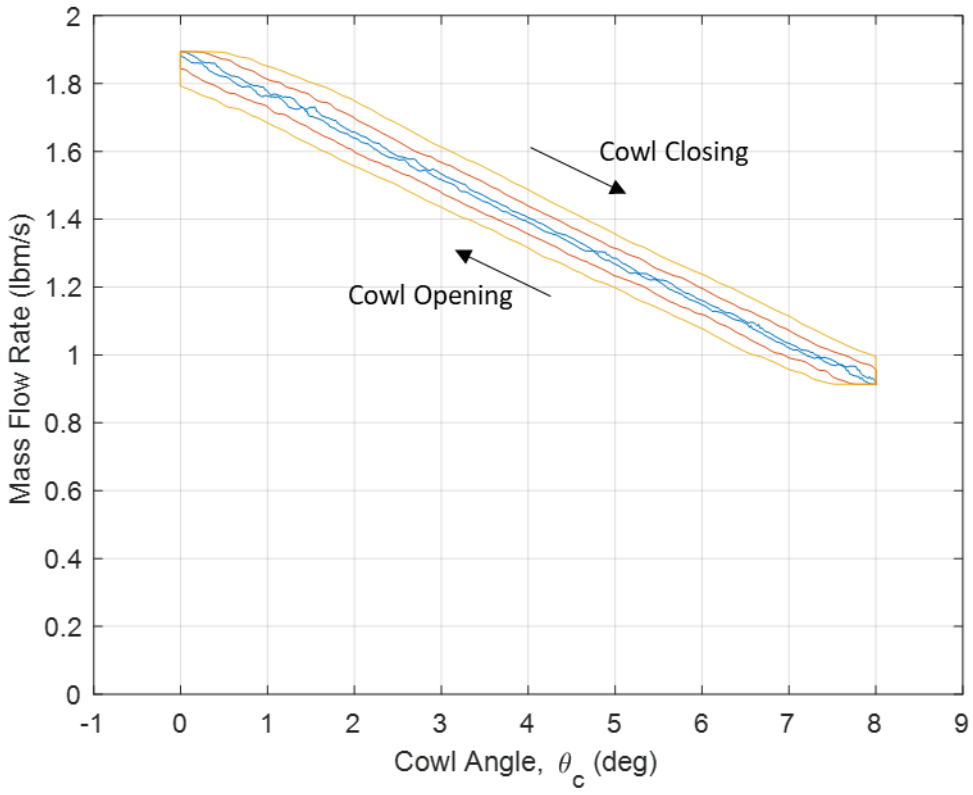

Figure 83: Mass Flow Rate Through the Inlet During the Rotation of the Cowl Plotted as a Function of Cowl Angle for Different Cowl Rotation Rates Obtained Using the Two-Dimensional Model

7.2.6 Turbulence Model Assessments

Similar to what was done with the Fixed-Cowl Model, an assessment of the effect of the turbulence model on the computed results was conducted for the three-dimensional, unsteady Variable-Cowl Model. Only the Cubic k-ε model (the baseline for all computations) and the Menter SST models were considered because of the increased computational time required for the transient computations. A comparison of the results obtained with these two models is shown below in Figure 84. The results shown were both obtained with the baseline time step of 10 μs. In general, the results show the same trends. However, the SST model predicts unstart to occur at an earlier angle, as was discovered using the Fixed-Cowl Model. The point of restart, however, agrees well. The SST model also tends to produce a more stable flow field with less unsteady oscillations during the unstarted phase when the cowl is held in the horizontal position. Overall, besides the fact the inlet unstarted earlier, the results between the two turbulence models were quite similar.

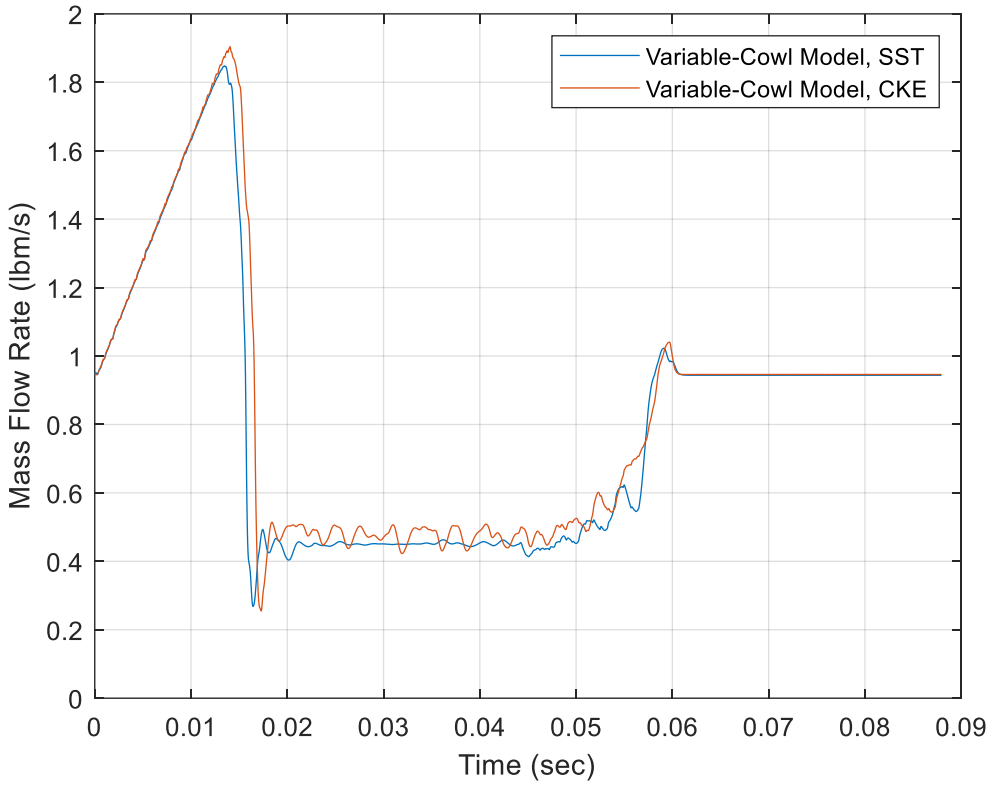

Figure 84: Comparison of Time Histories of Mass Flow Rate Through the Inlet Using the Cubic k-ε and Menter SST Turbulence Models

Table 16: Cowl Angle at Peak Mass Flow Rate and Peak Mass Flow Rate Obtained Using Different Turbulence Models

Turbulence Model	**Cowl Angle, θ_c, at Peak Mass Flow Rate (deg)**	**Time at Peak Mass Flow Rate (sec)**	**Peak Mass Flow Rate (lbm/s)**
Cubic k-ε Model	-0.0042	0.01405	1.9040
Menter SST Model	0.2880	0.01346	1.8478

A comparison of the centerline Mach number contours obtained from the Variable-Cowl Model with the Cubic k-ε Model and the Menter SST model is shown below. Figure 85 is taken at 13.45 ms which is essentially the point of peak mass flow rate for the computation with Menter SST model and Figure 86 is taken at 14.05 ms which corresponds to the peak mass flow rate for the computation with the Cubic k-ε Model. As can be seen in Figure 85, at the point of unstart for the Menter SST model, the size of the separation bubble at the shoulder of the inlet is larger than that at the same time for the Cubic k-ε Model. Alternatively, at the point of peak mass flow rate for the Cubic k-ε Model, the Menter SST model is already

showing the inlet unstarting with the separation bubbles moving upstream. This is again due to the slight differences in computation of the boundary layer thickness between the two models.

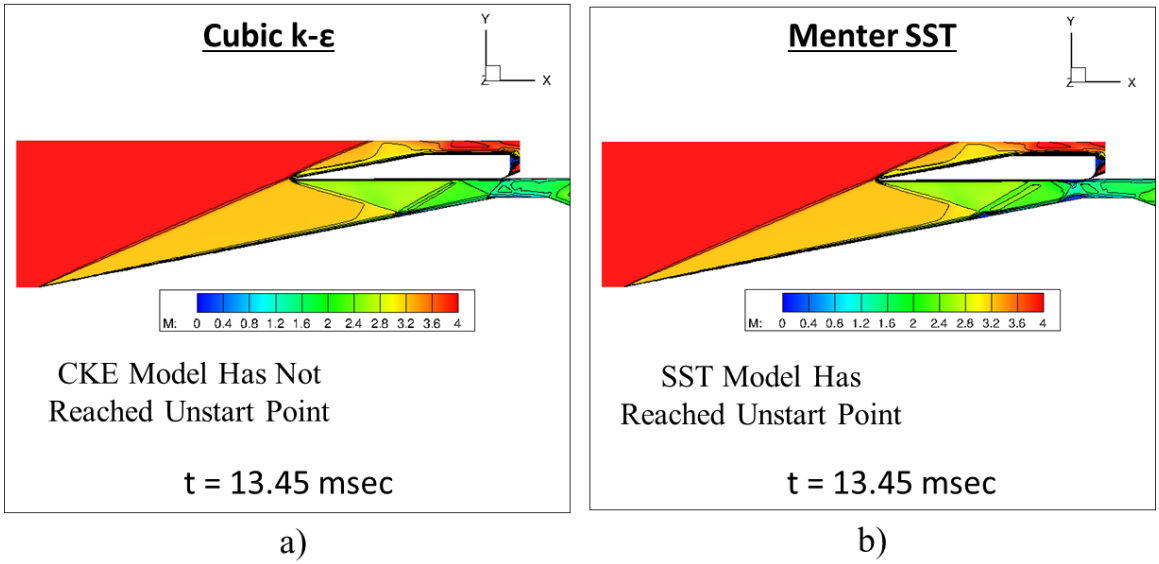

Figure 85: Centerline Mach Number Contours at 13.45 msec for the a) Cubic k-ε and b) SST Models

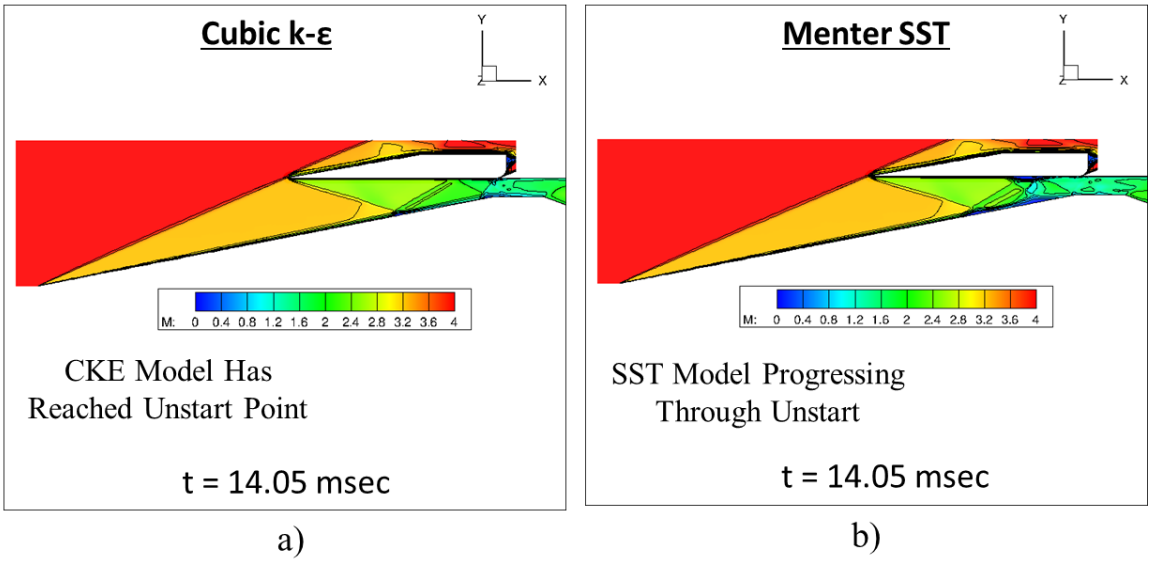

Figure 86: Centerline Mach Number Contours at 14.05 msec for the a) Cubic k-ε and b) SST Models

7.3 Summary and Discussion

The results presented in the Sections 6 and 7 have accomplished the main goals of this work outlined in Section 1.3. These were to develop a variable-geometry model to analyze the transient features of an inlet with a rotating cowl computationally and to compare those results to a traditional quasi-steady analysis approach; to use the variable-geometry model to obtain insights into the physics of the transients that inlet experiences including unstart, restart, and hysteresis induced by cowl motion; and to validate and verify the "new model" and to quantify uncertainties in the approach. This first goal was achieved by developing the Variable-Cowl Model. This new model used time-accurate CFD computations of the URANS equations coupled with an overset mesh motion methodology to analyze the inlet with a variable-geometry, rotating cowl. Good agreement in the quasi-steady limit with a traditional analysis approach was obtained. However, the new model allowed for more detailed information regarding the fully transient features of the unstart, restart, and hysteresis to be obtained.

Investigating these transient processes was the focus of the second goal of the work. Several key insights were obtained that highlighted important points about the unstart/restart characteristics and the analysis of variable-geometry inlets consisting of rotating cowls. First, the development of separated flow regions at the shock impingement points, as well as in the corner regions, played a principle role in the unstart process of the inlet. Indeed, without the corner regions, the inlet remained started, as was shown using the two-dimensional computations which effectively modeled an infinitely wide duct. It was shown that the corner flow regions include separated flows and vortical structures. These features influenced the main centerline inlet flow through the creation of spanwise flows that interacted with the main separation regions along the centerline. Through these interactions, the inlet was ultimately unstarted due to the limiting of the contraction ratio by the growing separation bubbles as the cowl was rotated open. Second, the hysteresis that existed when the inlet progressed from the unstarted to restarted condition was captured by the time-accurate computations. The hysteresis manifested itself as a requirement of a much smaller cowl angle to restart the inlet than was required to unstart the inlet. The results indicated that in all cases, the inlet unstarted when the cowl was at the horizonal position, but the inlet could not be restarted again until the cowl was positioned back to 8 deg below the horizontal. This process was shown to be driven primarily by

the viscous, separated flow that sets up ahead of the inlet when it unstarts. Third, the effect of cowl rotation rate was generally small; however, definite trends were observed. For example, as the cowl rotation rate decreased, the peak mass flow rate before unstart also decreased while the angle of this peak mass flow rate increased slightly.

The third goad of the work was to validate the new computational approach. A rigorous assessment of the errors and uncertainties of the Variable-Cowl Model indicated that Computation Fluid Dynamics is a valid tool for analyzing the transient response of a high-speed inlet in the presence of unstart/restart and hysteresis phenomena. The effect of turbulence model in the RANS computations was assessed and can lead to significant differences in the point of the unstart due to differences in the computed boundary layer thicknesses. In addition, the timestep is an important parameter and must be chosen wisely to balance computational time and accuracy. It was found that if the full details of the oscillatory, unstarted flow field are not required, the timestep can be chosen to be an order of magnitude larger than the characteristic wave speeds. This is an important note because in inlet analysis, it is generally desired to avoid unstarted operation because of the negative impacts on performance. Therefore, in an engineering analysis, the main goal is often just to identify the point at which the inlet unstarts, which can be done with a larger timestep, leading to much quicker analysis times.

Finally, CFD is an important tool for inlet analysis because of the detailed information that can be extracted that may not be easily obtained from experiment. Therefore, overall, the validation of CFD to accurately capture the inlet unstart/restart physics and the insights obtained in this work are significant findings that will form the basis for future investigations to build upon.

8 Conclusion

The focus of this work was to investigate the transient physics associated with a high-speed inlet and to expand the current database for inlet unstart/restart for variable-geometry inlets. This was accomplished using high-fidelity computational fluid dynamics techniques. The main goals of this work were to develop a variable-geometry model to analyze the transient features of an inlet with a rotating cowl computationally and to compare those results to traditional quasi-steady state analysis approaches, to use the variable-geometry model to obtain insight into the physics of the transients that inlet experiences including unstart/restart and hysteresis induced by cowl motion, and to validate and verify the "new model" and to quantify uncertainties in the approach.

First, a traditional analysis methodology was used which consisted of a series of steady-state computations conducted a three discrete cowl angles. These results were termed the "Fixed-Cowl Model" as individual computational grids were required with the cowl fixed in the discrete positions considered. The results of this model showed good comparison with the experimental results obtained in Ref. [3] when the inlet was started. A range of popular turbulence models showed the importance of accurately predicting the boundary layer thicknesses. It was found that the Cubic k-ε model provided the best results as it properly predicted the cowl angle at which the inlet unstarted. Other popular models such as the Menter SST model and the Spalart-Allmaras models yielded slightly larger displacement thicknesses which resulted in the inlet unstarting at angles larger than shown by the experimental results.

A two-dimensional Fixed-Cowl Model was also created to highlight the need for three-dimensional computations. The two-dimensional model showed similar trends to the three-dimensional model when the inlet was started but significantly underpredicted the compression due to not including the effect of the sidewall shocks and corner flows that developed. In addition, because the two-dimensional model lacked the latter, it allowed the inlet to remain started for all cowl angles considered, whereas the three-dimensional model and the experimental data showed the inlet to unstart once the cowl reached the horizontal position. This highlighted the importance of the corner flows in the unstart process that was to be investigated further in the time-accurate computations.

The time-accurate computations were performed using the “Variable-Cowl Model” which was the primary advancement in variable-geometry inlet analysis presented in this work. This model made use of overset mesh techniques that allowed for relative rotational motion of the cowl during transient computations. The model was first validated against the Fixed-Cowl Model and experimental data by replicating the steady-state analyses at the same discrete cowl angles as consisted with the Fixed-Cowl Model. Good agreement between the two models and the experimental data was achieved, and that validated the Variable-Cowl Model. After validation, the Variable-Cowl Model was used to investigate the transient features of the inlet unstart and restart. Time-dependent histories of the complete flowfield, including pressures and mass flow rate through the inlet, were obtained as the cowl was rotated from 8 deg below the horizontal to the horizontal position. As the cowl progressed through this motion, the development of the corner flows observed statically with the Fixed-Cowl Model were captured. In particular, the development of separated flow regions at the cowl-shock impingement point and in the isolator were observed. These separated regions included vortices that drew fluid in from the sidewalls leading to a three-dimensional flow pattern. As the vortices and separation bubbles grew, they choked the inlet leading to a contraction ratio induced inlet unstart. Once the unstart process was initiated, a transient process in which the separation bubbles and shock train moved upstream and were eventually ejected out of the inlet after which a large separation bubble ahead of the cowl lead to significant spillage that prevented the inlet from restarting.

As the cowl began to rotate closed, this separation bubble was reduced in size allowing for the mass flow rate to increase. Once the separation shock reached the shock-on-lip condition, the spillage ended, and the inlet restarted allowing for the shock train to be reestablished inside of the inlet. Hysteresis existed such that the point at which the inlet restarted did not correspond to the point at which the inlet unstarted. A significant finding was that the quasi-steady Fixed-Cowl Models only replicated the started side of this hysteresis loop and could not capture the restart process. This was because a time-dependent analysis was necessary to march from the unstarted solution to the restarted solution to include the physics associated with the hysteresis.

The rate of cowl rotation was shown to affect the process slightly. As the cowl rotation rate increased, the peak mass flow rate through the inlet increased slightly. In addition, the cowl angle at which the inlet unstarted increased slightly with an increase in cowl rotation rate. In general, however, the trends were similar with all rotation rates considered.

A two-dimensional Variable-Cowl Model was also created to highlight the three-dimensionality of the flow field. As the inlet opened, the cowl did not unstart as found with the Fixed-Cowl Model. The growth of the separation bubbles was significantly reduced as the cowl opened compared to the three-dimensional model. This was due to the inability to capture the corner flow regions and again highlighted the need for three-dimensional computations.

Finally, the effect of turbulence model on the transient computations was also considered by comparing results obtained with the baseline Cubic k-ε model with those obtained using the Menter SST model. The results were qualitatively similar with the Menter SST model showing unstart to occur sooner. Also, once unstarted, the Menter SST model showed less unsteadiness in the form of oscillatory flow.

The last goal of this work was to provide an estimate for the uncertainties present in the new Variable-Cowl Model. This was done in the form of rigorous spatial, iterative, and temporal convergence studies. The grids were found to be in the asymptotic range and relative errors and grid convergence indices were calculated. The baseline grids were found to be acceptable. The baseline timestep was found to not capture the timescales associated with the shock motion when the inlet was unstarted but were observed to be adequate to compute the unstart and restart points. Finally, iterative convergence was also observed with the baseline number of sub-iterations.

Overall, this work has presented the development of a high-fidelity computational approach to analyze inlet unstart, restart, and the associated hysteresis in a high-speed inlet with a rotating, variable geometry cowl.

8.1 Future Works

For future studies, it is suggested that additional computations be undertaken to investigate the effect of different Reynolds numbers and freestream Mach numbers on the unstart/restart process. The effect of Reynolds number is expected to change the cowl angle at which the inlet unstarts because of the change in the boundary layer thicknesses. However, whether the Reynolds number has a significant impact on the development of the corner flows and separation regions is yet to be determined. By varying the freestream Mach number, the unstart/restart characteristics of the inlet at off-design conditions could be assessed. In addition to Mach number, the effect of angle of attack and sideslip should be investigated as this will also lead to off-design performance of the inlet. Characterizing the transient characteristics in these off-design conditions are important as a flight vehicle is rarely operating at the design point.

Finally, the current work focused on the use of unsteady, RANS computations. However, it would be informative to apply the same computation process using a hybrid model that incorporates the use of RANS turbulence models near the wall and Large-Eddy Simulation (LES) in the free-shear regions. These Hybrid RANS-LES models are particularly useful in flows with massive separation like the resulting unstarted flow field shown in this work. Using a hybrid model will allow for less modeling of the turbulence and will resolve more of the large-scale turbulent features. This would be useful to compare the RANS models against and provide validation of the RANS solutions while at the same time providing more statistics of the turbulent flow.

9 References

[1] Fry, R.S. "A Century of Ramjet Propulsion Technology Evolution," *Journal of Propulsion and Power*, Vol. 20, No. 1, 2004, pp. 27-58.

[2] Curran, E.T., "Scramjet Engines: The First Forty Years," *Journal of Propulsion and Power*, Vol. 17, No. 6, 2012, pp. 1138-1148.

[3] Emami, S. Trexler, C.A., Auslender, A.H., Weidner, J.P., "Experimental Investigation of Inlet-Combustor Isolators for a Dual-Mode Scramjet at a Mach Number of 4," NASA-TP-3502, May 1995.

[4] "NASA Armstrong Fact Sheet: Hyper-X Program," February 28, 2014 https://www.nasa.gov/centers/armstrong/news/FactSheets/FS-040-DFRC.html.

[5] Heiser, W.H., and Pratt, D.T., *Hypersonic Airbreathing Propulsion*, AIAA Education Series, AIAA, Washington D.C., 1994.

[6] Anderson, J.D., *Introduction to Flight*, 7th Ed., McGraw Hill Companies Inc., New York, 2012.

[7] McClinton, C.R., "X-43 – Scramjet Power Breaks the Hypersonic Barrier: Dryden Lectureship in Research for 2006," AIAA Paper 2006-1, January 2006.

[8] Bauer, C., Petters, D., and Whitcomb, C., "Comparison of Mach 3 to 6 Conventional and Dual-Mode Ramjet Performance", AIAA Paper 98-3426, July 1998.

[9] "Ramjet/Scramjet Thrust," https://www.grc.nasa.gov/www/k-12/airplane/ramth.html, Accessed 10/10/2019.

[10] Moran, M.J., and Shapiro, H.N., *Fundamentals of Engineering Thermodynamics*, 7th Ed., John Wiley & Sons Inc., 2011

[11] Hill, P.G., and Peterson, C.R., *Mechanics and Thermodynamics of Propulsion*, 2nd Ed., Addison-Wesley Publishing Company Inc., Reading, MA, 1992.

[12] Kopasakis, G., Connolly, J.W., and Kratz, J., "Quasi One-Dimensional Unsteady Modeling of External Compression Supersonic Inlets," AIAA Paper 2012-4147, July 2012.

[13] Holland, S.D., and Perkins, J.N., "Internal Shock Interactions in Propulsion/Airframe Integrated Three-Dimensional Sidewall Compression Scramjet Inlets," AIAA 92-3099, July 1992.

[14] Kopasakis, G. and Connolly, J.W., "Shock Positioning Controls Design for a Supersonic Inlet," NASA TM-2010-216074, February 2010.

[15] Chang, J., Wang, L., Bao, W., Yang, Q., and Qin, J., "Experimental Investigation of Hysteresis Phenomenon for Scramjet Engine", *AIAA Journal*, Vol. 52, No. 2, 2014, pp. 447-451.

[16] Schetz, J.A., *Boundary Layer Analysis*, 2nd Ed., AIAA Education Series, AIAA, Reston, VA, 2011.

[17] "Fundamentals of Boundary Layers," F.H. Abernathy, in The National Committee for Fluid Mechanics Book of Film Notes, MIT Press, Cambridge, MA, 1972.

[18] Anderson, J.D., *Hypersonic and High-Temperature Gas Dynamics*, 2nd Ed., AIAA Education Series, AIAA, Reston, VA, 2006.

[19] Dussauge, J.P., Dupont, P., and Debieve, J.F., "Unsteadiness in Shock Wave Boundary Layer Interactions with Separation", *Aerospace Science and Technology,* Vol. 10, Issue 2, 2006.
[20] Smits, A.J., and Dussauge, J.P., *Turbulent Shear Layers in Supersonic Flow*, 2nd Ed., Springer Science and Business Media Inc., New York, 2006.

[21] Xiang, X., and Babinski, H., "Corner Effects for Oblique Shock-Wave/Boundary Layer Interactions in Rectangular Channels", *Journal of Fluid Mechanics*, Vol. 862, March 2019, pp. 1060-1083.

[22] Wang, B., Sandham, N.D., Hu, Z., and Liu, W., "Numerical Study of Oblique Shock-Wave/Boundary Layer Interaction Considering Sidewall Effects", *Journal of Fluid Mechanics*, Vol. 767, March 2015, pp. 526-561.

[23] Edwards, J.R., "Numerical Simulations of Shock/Boundary Layer Interactions using Time-Dependent Modeling Techniques: A Survey of Recent Results", *Progress in Aerospace Sciences*, Vol. 44, Issue 6, 2008, pp. 447-465.

[24] Gaitonde, D.V., "Progress in Shock Wave/Boundary Layer Interactions", *Progress in Aerospace Sciences*, Vol. 72, January 2015, pp. 80-99.

[25] Pritchard, P.J., *Fox and McDonald's Introduction to Fluid Mechanics,* 8th Ed., John Wiley & Sons Inc. Hoboken, NJ, 2011.

[26] Zhang, Q.F., Tan, H.J, Chen, H., Yuan, Y.Q., Zhang, Y.C., "Unstart Process of a Rectangular Hypersonic Inlet at Different Mach Numbers", *AIAA Journal*, Vol. 54, No. 12, 2016, pp. 3681-3691.

[27] Sorenson, N.E., Latham, E.A., and Smeltzer, D.B. "Variable Geometry for Supersonic Mixed-Compression Inlets", *Journal of Aircraft*, Vol. 14, No. 4, 1976, pp. 309-312.

[28] "Supersonic Transport Development Program, Phase III Proposal," Lockheed-California Co., Burbank, Calif., Vol. II-E Propulsion Rept. Book 1 of 3, Rept. 19841, Sept. 1966.

[29] "Commercial Supersonic Transport Proposal," Propulsion A-VI, The Boeing Company, Seattle, Wash., Rept. D6-2400-12, Jan. 15, 1964.

[30] Starkey, R.P., "Off-Design Performance Characterization of a Variable Geometry Scramjet", AIAA Paper 2005-3711, July, 2005.

[31] Sanders, B.W and Weir, L.J. "Aerodynamic Design of a Dual-Flow Path Mach 7 Hypersonic Inlet System of a Turbine-Based Combined-Cycle Hypersonic Propulsion System", NASA CR-2008-215214, June 2008.

[32] Yuan, H. Wang, Y, Liu, J. and Hua, Z., "Aerodynamic Design and Performance Analysis of a Two-Dimensional Variable Geometry Inlet", AIAA Paper 2017-2275, March 2017.

[33] Hui, Y., Jun, M., Man, Y., Zhu, S., Ling, W., and Cao, X., "Numerical Simulation of Variable-Geometry Inlet for TRRE Combined Cycle Engine," AIAA Paper 2017-2437, March 2017.

[34] Weiting, A.R., "Exploratory Study of Transient Unstart Phenomena in a Three-Dimensional Fixed-Geometry Scramjet Engine," NASA TN-D-8156, Mach 1976.

[35] Shimura, T., Mitani, T., Sakuranaka, N., and Izumikawa, M., "Load Oscillations Caused by Unstart of Hypersonic Wind Tunnels and Engines," *Journal of Propulsion and Power*, Vol. 14, No. 3, 1998, pp. 348-353.

[36] Rodi, P.E., Emami, S. and Trexler, C.A., "Unsteady Pressure Behavior in a Ramjet/Scramjet Inlet", *Journal of Propulsion and Power*, Vol. 12, No. 3, 1996, pp. 486-493.

[37] Wagner, J.L., Valdivia, A., Yuceil, K.B., Clemens, N.T., Dolling, D.S., "An Experimental Investigation of Supersonic Inlet Unstart," AIAA Paper 2007-4352, June 2007.

[38] Do, H. Im, S.K, Mungal, M. and Capelli, M., "The Influence of Boundary Layer Separation on Supersonic Inlet Unstart", AIAA Paper 2011-2349, April 2011.

[39] Hawkins, W.R., Marquart, E.J., "Two-Dimensional Generic Inlet Unstart Detection at Mach 2.5-5.0," AIAA Paper 1995-6019, April 1995.

[40] Pletcher, R.H., Tannehill, J.C., and Anderson, D.A., *Computational Fluid Mechanics and Heat Transfer*, 3rd Ed. CRC Press, Boca Raton, FL, 2013.

[41] Roy, C.J., "Review of Code and Solution Verification Procedures for Computational Simulation," *Journal of Computational Physics*, Vol. 205, Issue 1, 2005, pp. 131-156.

[42] Reinartz, B.U., Herrmann, C.D., Ballmann, J. and Koschel, W.W., "Aerodynamic Performance Analysis of a Hypersonic Inlet Using Computation and Experiment," *Journal of Propulsion and Power*, Vol. 19, No. 5, 2003, pp. 868-875.

[43] Haberle, J. and Gulhan, A., "Internal Flowfield Investigation of a Hypersonic Inlet at Mach 6 with Bleed.," *Journal of Propulsion and Power*, Vol. 23, No. 5, 2007, pp. 1007-1017.

[44] Yentsch, R.J., and Gaitonde, D.V., "Numerical Investigation of the HIFiRE-2 Scramjet Flowpath," AIAA Paper 2013-0119, January 2013.

[45] Mayer, D.W., Paynter, G.C., "Prediction of Supersonic Inlet Unstart Caused by Freestream Disturbances", *AIAA Journal*, Vol. 33, No. 2, 1995, pp. 266-275.

[46] Neaves, M.D., McRae, D.S., Edwards, J.D., "High-Speed Inlet Unstart Calculations Using an Implicit Solution Adaptive Mesh Algorithm," AIAA Paper 2001-0825.

[47] Hoeger, T.C., "CFD Transient Simulation of an Isolator Shock Train in a Scramjet Engine," Ph.D. Dissertation, Air Force Institute of Technology, Wright-Patterson AFB, OH, 2012

[48] Riley, L.P., Hagenmaier M.A., Donbar, J.M., and Gaitonde, D.V., "A Computational Investigation of Unstart in a Dual-Mode Scramjet," AIAA Paper 2016-1901, January 2016.

[49] Riley, L.P., Gaitonde, D.V., Hagenmaier, M.A., and Donbar, J.M., "Isolator Dynamics During Unstart of a Dual Mode Scramjet," *Journal of Propulsion and Power*, Vol. 34, No.6, 2018, pp. 1409-1427.

[50] Yentsch, R.J., and Gaitonde, D.V., "Unsteady Three-Dimensional Mode Transition Phenomena in a Scramjet Flowpath," *Journal of Propulsion and Power*, Vol. 31, No. 1, 2015, pp. 104-122.

[51] Yentsch, R.J. and Gaitonde, D.V., "Unsteady Three-Dimensional Phenomena in Mode-Transition Simulations of the HIFiRE-2 Scramjet Flowpath," AIAA Paper 2013-3753, July 2013.

[52] Grainger, A.L., Brieschenk, S., Boyce, R.R., Malpress, R., and Buttsworth, D., "Investigation into the Flow Physics of Hypersonic Variable Geometry Inlet Starting," AIAA Paper 2014-3230, June 2014.

[53] Xianhong, X., Yuan, L., and Zhansen, Q., "Aerodynamic Design and Numerical Simulation of Over-Under Turbine-Based Combined-Cycle (TBCC) Inlet Mode Transition," *Procedia Engineering*, Vol. 99, 2015, pp. 129-136.

[54] Li, N., Chang, J., Jiang, C., Yu, D., Bao, W., Song, Y., and Jiao, X., "Unstart/Restart Hysteresis Characteristics of an Over-Under TBCC Inlet Caused by Backpressure and Splitter," *Aerospace Science and Technology*, Vol. 72, January 2019, pp. 418-425.
[55] Anderson, J.D., *Modern Compressible Flow with Historical Perspective*, 3rd Ed., McGraw Hill, New York, 2003.

[56] Liepmann, H.W., and Roshko, A., *Elements of Gas Dynamics*., Dover Publications Inc., Mineola, NY, 1985.

[57] McBride, B.J., Gordon, S., and Reno, M.A., "Coefficients for Calculating Thermodynamic and Transport Properties of Individual Species," NASA TM-4513, October 1993.

[58] Pope, S.B., *Turbulent Flows*, Cambridge University Press, 2000.

[59] Wilcox, D.C., *Turbulence Modeling for CFD*, DCW Industries Inc., La Canada, CA, 1993.

[60] METACOMP, Inc., *CFD++ User Manual, Version 18.1*.

[61] Spalart, P.R. and Allmaras, S.R. "A One-Equation Turbulence Model for Aerodynamic Flows," AIAA Paper 1992-439, January 1992.

[62] Yentsch, R.J., and Gaitonde, D.V., "Effect of Initial Conditions on Simulations of a Scramjet Flowpath", *Journal of Propulsion and Power*, Vol. 30, No. 4, 2014, pp. 1107-1112.

[63] Candler, G.V., Barnhardt, M.D., Drayna, T.W., Nompelis, I., Peterson, D.M., and Subbareddy, P., "Unstructured Grid Approaches for Accurate Aeroheating Simulations," AIAA Paper 2007-3959, June 2007.

[64] Roache, P.J., *Verification and Validation in Computational Science and Engineering*, Hermosa Publishers, Albuquerque, NM, 1998.

[65] Edney, B.E., "Anomalous Heat Transfer and Pressure Distributions on Blunt Bodies at Hypersonic Speeds in the Presence of an Impinging Shock," *Flygtekniska Forsoksanstalten*, Stockholm, Sweden: The Aeronautical Research Inst. of Sweden (FFA), 1968.

[66] Edney, B.E., "Effects of Shock Impingement on the Heat Transfer Around Blunt Bodies," *AIAA Journal*, Vol. 6, No. 1, 1968, pp. 15-21.

[67] Lind, C.A., "Effect of Geometry on the Unsteady Type IV Shock Interaction," *Journal of Aircraft*, Vol. 34, No. 1, 1997, pp. 64-71.

[68] Roy, C.J. and Blottner, F.G., "Review and Assessment of Turbulence Models for Hypersonic Flows," *Progress in Aerospace Sciences*, Vol. 42, Issues 7-8, 2006, pp. 469-530.

[69] Yentsch, R.J., Gaitonde, D.V., and Kimmel, R., "Performance of Turbulence Modeling in Simulation of the HIFiRE-1 Flight Test," *Journal of Spacecraft and Rockets*, Vol. 51, No. 1, 2014, pp. 117-127.

[70] Shahab, M.F., Lehnasch, G., Gatski, T.B., and Comte, P., "Statistical Characteristics of an Isothermal, Supersonic Developing Boundary Layer Flow from DNS Data," *Flow, Turbulence and Combustion*, Vol. 86, Issue 3-4, pp.369-397.